Theoretical Investigations of the Interactions Between Peptides and Inorganic Surfaces

Zur Erlangung des akademischen Grades eines

DOKTORS DER NATURWISSENSCHAFTEN

(Dr. rer. nat.)

von der Fakultät für Chemie und Biowissenschaften

des Karlsruher Instituts für Technologie (KIT)

genehmigte

DISSERTATION

von

Magister Monika Borkowska-Panek

aus

Zielona Góra, Polen

KIT-Dekan:	Prof. Dr. W. Klopper
Referent:	PD Dr. K. Fink
Korreferent:	Prof. Dr. W. Klopper

Tag der mündlichen Prüfung: 10. Februar 2017

Contents

1 Introduction

Investigating the interactions between peptides and inorganic surfaces is essential to understand the more complex phenomenon of interactions in biologically relevant systems of a mixed organic-inorganic nature. This knowledge is invaluable in various fields, like, biotechnology, nanotechnology, and materials science for designing new biomimetic hybrid materials[1–3]. In medicine, in turn, such materials can be used as transporters delivering drugs into the cells[4–12]. Gaining a detailed understanding of the surface-peptide interactions is essential for the selection of appropriate surfaces and peptides. This was the aim of a joint experimental and theoretical project entitled "Rational design of peptide-surface interactions", funded by the Federal Ministry of Education and Research (BMBF) in the Biotechnology 2020+ initiative. The goal was to find and to design new peptide sequences which are selective direct binders to nanoparticle surfaces of magnetic iron oxides. Iron-oxide nanoparticles are preferred in various applications due to their magnetic properties, and the low cost of production. The experimental investigations were performed at the Technical University of Munich (TUM) in the group of Prof. Sonja Berensmeier, the theoretical investigations at the Institute of Nanotechnology (INT) of Karlsruhe Institute of Technology (KIT). The experimental part was devoted to characterization of the surface properties, the structures of the interacting peptides, as well as to the verification of the interactions.

The aim of the thesis was the development of protocols for the description of the peptide-surface interactions under various experimental conditions. Next, to provide and test the methodology for the efficient theoretical assessment of the binding affinity between peptides and surfaces. The setup was parametrized with literature data and partially from the experimental results. It allows to reproduce the experimental results, as well as predict sequences of well-binding peptides. Finally, to employ quantum-chemical methods to investigate electronic properties of iron oxide and derivative mixed-center systems.

This thesis is organized as follows. In the remaining parts of the introduction, applications, experimental and theoretical methods for characterization of peptide-surface interactions are described. First, various applications of inorganic surfaces coated by organic molecules (mostly proteins) are presented in Chapter 1.1. Next, experimental and theoretical methods used to investigate peptide-surface interactions are presented in Chapters 1.2, and 1.3, respectively. In Chapter 2.1, the interactions occurring between amino acids and inorganic surfaces are introduced. In Chapter 2.2, the electronic and magnetic properties of iron oxide (magnetite) are considered, including spinel structures and its derivatives with manganese and zinc. Furthermore, the properties of magnetic nanoparticles (MNPs) are discussed in particular. In Chapter 2.3, the main experimental method, namely, peptide array screening, used by the experimental collaborators, to measure peptide-surface affinity is described. In Chapter 3, the main computational protocols used in this thesis to predict peptide-surface affinity are described. These rely on Metropolis Monte Carlo simulations supported with the metadynamics approach and the Effective Implicit Surface Model (EISM). In Chapter 4, the EISM calibrated against theoretical reference data was

used to reproduce reference peptide binding affinities to gold (111) and silver (111) surfaces. Chapter 5 is divided into two parts directly connected to the results provided by the experimental group from TU Munich. In Chapter 5.1, the affinity of magnetic nanoparticles to a set of peptides is measured under different pH and solvent conditions. In order to explain and reproduce these results, an analytical model, based on possible equilibrium reactions occurring during the experimental procedure, is introduced. In Chapter 5.2, the EISM model is calibrated against the experimentally obtained binding affinities of amino acids and used to reproduce and predict binding affinities of various peptide sequences. The EISM results are then directly compared with the experimental results. Further analysis in Chapter 5.3 shows an influence of the composition and length of the peptide chain on the changes of the Gibbs free energy of binding. Based on these results, peptide sequences, which bind selectively to the magnetic nanoparticles, can be designed. Finally, in Chapter 6 the electronic properties of magnetite and its derivatives with manganese and zinc are investigated by means of the density-functional theory (DFT) methods employing Point Charge Field Embedding model. In Chapter 7, the summary of this thesis is given.

1.1 Peptides in biotechnology – applications

Peptides find various application in biotechnology and bioengineering. A combination of the protein collagen and the mineral hydroxyapatite was found to build bones and other tissues with different flexibility[13–15] and became important in bone and dentin tissue engineering[16]. Implants covered with proteins can be protected from an immune response[17]. A deeper insight into bacterial resistance to antibiotics showed that it is due to the biofilm which is made by bacteria[18,19], interruption in the process of binding the protein to the substrate could solve this important problem. In nanotechnology the interactions of peptides and inorganic materials are essential for crystal growth regulation[20–26], surface biocompatibility and synthesis of nanoparticles[23,25,27–33]. New, functionalized nanoparticles are characterized by various and unique properties[34–37]. Mussels Adhesive Proteins (MAPs) produced by marine mussels[38] are containing a specific amino acid, 3,4-dihydroxyphenylalanine (DOPA), which generates the adhesion to plenty of inorganic surfaces such as metals, oxides and polymers. Functionalized nanoparticles could be used to produce, e.g., biodegradable glues, characterized by high mechanical strength, able to connect components of different type[39–44]. Combination of nanoparticles with peptides can also have influence on the optical properties of the system. The size and the shape of nanoparticles, as well as occurrence of molecular recognition groups (peptides, surfactants) determine the plasmon resonance frequency in such a way that it can induce adequate shifts in the UV/vis absorption spectrum[45–47].

1.2 Experimental techniques to investigate peptide-surface interactions

There are many experimental tools, which can be used to investigate the nature of interactions between peptides and inorganic surfaces. In the following section some of the most prominent experimental methods are introduced. Phage display is one of the most important techniques for verifying the presence of binding to the surface[2,22,24–26,48,49]. Here, use of bacteriophages (bacterial viruses) allows to identify peptide sequences with specific binding

affinity to the investigated surface. This technique is called *in vitro* selection, which allows to screen whole libraries of proteins. With the quartz crystal microbalance (QCM)[50–53] technique small changes in the mass of a resonating crystal, due to the absorption of matter, can be detected. This change manifests itself in a change of the resonance frequency of the crystal. It is a highly effective tool for determining the affinity of molecules (proteins, peptides) to surfaces. Gibbs free energies of binding of a set of peptides to gold(111) and silver(111) surfaces obtained using this technique, were used as reference data in Chapter 4. In the surface plasmon resonance (SPR)[54–56] technique a polarized light is reflected from the metal surface and detected as a dark line on a detector. In case of an adsorption on the investigated surface a shift of this reflected signal is observed. Both techniques, QCM and SPR, are measuring the adsorption of the peptides on inorganic surfaces as a whole, however they do not give information about the binding mechanism. More knowledge on the structural aspects of the binding can be gathered with single molecule force microscopy with atomic force microscopy (AFM)[54,57–67], which can monitor the interactions between any pair of molecules, i.e., during an absorption of molecules on a surface. In this technique, the investigated material is scanned using a cantilever with a tip on its end. The tip is in close contact with the sample surface, because of an attractive force between them, and is causing deflection of the cantilever towards or away from the surface. The whole process is measured by detection of a laser beam which is changing its direction together with the deflection of the cantilever, and as a result gives the topography of the scanned area of the surface, and at the same time information if something is bound to it. Although all presented experimental methods are able to find various peptide sequences binding to the specific surfaces, there is no straightforward answer, why the compatibility occurs. Since various sequences of peptides may bind with similar affinities, explanation of the binding mechanism may be very difficult or impossible. In such cases a support from computational methods is required.

1.3 Computational methods for the investigation of peptide-surface interactions

Computational methods provide methodologies to investigate the properties of the system itself, the nature of the interactions[68], as well as direct access to the relation between the structure and the interactions. However, due to the number of possible peptide sequences and structural complexity of the inorganic surfaces, efficient computational approaches are required.

Depending on the investigated properties, and the type and size of the considered systems, as well as the type of dominating interactions, different computational methods are available. There are two general routes, either a larger part of the free energy landscape can be described with molecular dynamics (MD)[69–71] or Monte Carlo (MC) methods based on empirical force fields at the cost of accuracy. Alternatively, selected fragments can be treated with a higher accuracy employing quantum-mechanical methods. In the main part of this work, MD and MC methods are considered, and in the following some respective methods for large-scale simulations are discussed. First of all, sampling of the free-energy landscapes is not a straightforward task. For instance, an exploration of the landscape for a system with several local minima and saddle points in between can be out of reach for the molecular dynamics time scale. Here, methods like umbrella sampling[72–82] and

thermodynamic integration[78,83–85] are useful. They require information about the reaction path between the substrate and the product. In the umbrella sampling, an external resistant is added, hence only a predefined part of the space is explored. The limitation of this method is that a realistic guess for the location of the free-energy barrier is mandatory. The definition of the thermodynamic integration is related to the umbrella sampling method, but in this case the bias is considered to be infinitely strong. By calculating differences of free energies one can simulate real chemical processes. This method is applicable for systems, where a direct simulation of the process is impossible, because the potential energies of the considered states depend on different space coordinates. In this method the thermodynamic path between states is determined, along which the integration over averaged enthalpy changes is carried out. Steered molecular dynamics (SMD) was developed to reduce simulation times of classical MD methods, and became the most popular non-equilibrium simulation technique for biomolecular systems[86–99]. In this method, external forces are applied to manipulate the structure by pulling it along defined degrees of freedom. There are two ways of proceeding, one is with constant pulling velocity and second with constant pulling force. This method can be used for mechanical unfolding or stretching of the proteins, binding or dissociation of a ligand. Nevertheless, molecular-dynamics-based methods still require relatively long runs for well equilibrated simulations fulfilling ergodicity conditions. To explore larger areas of the phase space, and avoid being trapped in local minima metadynamics approach can be applied[100–105]. Here, a positive Gaussian potential is added to the energy landscape, in order to prevent the system from coming back to an already visited point. This approach was applied to boost the efficiency of the Monte Carlo simulations performed in this thesis, see Chapter 3.3 for more details.

In this thesis the interaction of peptide sequences with on average around twelve amino acids with inorganic surfaces was considered. The conformer flexibility of peptides has a direct influence on their ability to bind with their binding side chains to the surface. To ensure that all important conformations are sampled during the simulation MC simulations instead of molecular dynamics were used. To neglect numerous degrees of freedom of water molecules, an implicit solvent model was applied. As it turned out, proper modeling of the surface structure is not a trivial task for the considered systems. Iron oxides are open shell systems, and in the form of the nanoparticles have inhomogeneous surfaces with several defects. Additionally, in the solution they are coated by solvent ions, see Chapter 2.2 for details. Therefore, a proper description of the surface, including all the mentioned effects, is required. However, an explicit treatment of these contributions is very difficult and leads to inefficient models.

In order to address these problems, we have developed the EISM model which is using an implicit representation of the surface, see Chapter 3.4 for a detailed description. EISM allows us to simulate the behavior of various peptide sequences towards multiple surfaces with a very high efficiency. It is using empirical data for the definition of the affinity of amino acids to the investigated surface under certain experimental conditions. Within this method, we are able to predict the strength of binding of selected peptide sequences and also to trace the behavior of the individual amino acids in contact with the surface. It is a novel versatile model which can be used for surfaces of any type, for which data, obtained either experimentally or theoretically, about its interactions is available for all amino acids.

2 Background

2.1 Binding mechanisms of single amino acids to inorganic surfaces

Depending on the acid-base properties of each amino acid there are several possible mechanisms of adsorption on inorganic surfaces, for comprehensive reviews see Refs. 106 and 107. Most generally, we can divide the interactions into two groups, short-range interactions (covalent) and long-range interactions (noncovalent).

2.1.1 Covalent bonding

Covalent bonding is in the group of short-range interactions and takes place when two atoms are sharing an electron pair. It is the most pronounced interaction, when the molecule is small and not yet dominated by long-range interactions. The size of the molecule determines its ability to orientate properly to form a chemical bonding. As reported in the theoretical paper of Collins and coworkers[108], who were using semi-empirical molecular orbital calculations, amino acids can form a so-called anhydride, or "surface ester", with surface hydroxyl groups. Concerning a surface A covered with hydroxyl groups, such reaction for glycine can be schematically written as

$$NH_2CH_2COOH + A{-}OH \longrightarrow NH_2CH_2COO{-}A + H_2O.$$

Much more rare, but also possible are bidentate coordinative bonds, which were investigated, e.g., by Qiu et al.[109] using scanning tunneling microscopy (STM) and describe binding of two unsaturated Ti^{4+} centers from titania (TiO_2) with deprotonated glycine (glycinate, NH_2CH_2COO), which is bound to the surface through both of the carboxylate O atmos.

2.1.2 Noncovalent bonding

There are several possibilities of interactions of amino acids with inorganic surfaces via noncovalent bonding. In case of peptides and proteins, the description of the long-range interactions is the most demanding task in any kind of computational simulations. The considered systems and molecules contain hundreds of amino acids, and noncovalent bonding covers interactions for all pairs of atoms located further than the sum of their van der Waals radii, and thus the number of the energy terms which need to be included in the calculations is increasing rapidly with the system's size. The bond energy of noncovalent interactions is typically in the range of 1–5 kcal mol^{-1} [110].

2.1.2.1 Electrostatic interaction

Electrostatic interactions are important for amino acids with electrically charged or polar side chains. Out of all amino acids, there are two with negatively charged side chains, namely glutamic acid (E) and aspartic acid (D), and three with positively charged side chains, namely arginine (R), lysine (K), and a less charged histidine (H). The protonation/deprotonation states of carboxyl (acidic) and amino groups (basic) of charged amino acids is strongly dependent on the pH of the solution in which the reaction takes place, see general reactions in Figures 2.1 and 2.2.

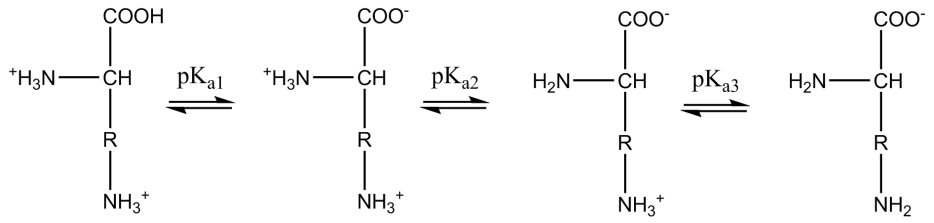

Figure 2.1: Protonation states of a positively charged amino acid in function of pH.

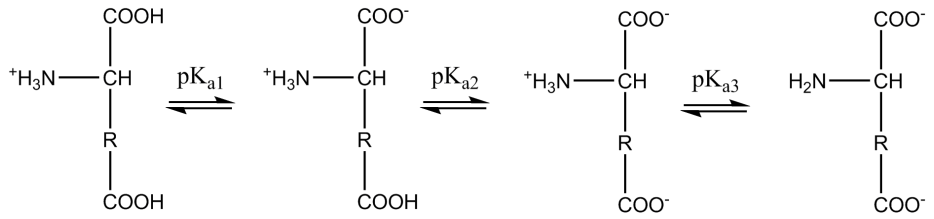

Figure 2.2: Protonation states of a negatively charged amino acid in function of pH.

Depending on the pH of the solution, the positively charged amino acids are having various charges, starting from '2+', over '1+" and '0' to '1-', but in the widest range of pH, i.e., between 2–10, their charges are equal to '1+'. In turn, the negatively charged amino acids are having charges between '1+" and '2-', and in the widest pH range, 4–10, their charge is equal to '1-'. It is worth to underscore that charged amino acids, due to the presence of amino and carboxyl groups, belong to the special group of amphoteric compounds, which are able to form zwitterions at a specific pH. That gives multiple possibilities of interactions. Furthermore, the oxide surfaces are slightly charged, and their charge is pH-dependent as well; in low pH a positive charge is observed, and in high pH ranges a negative one. For instance, point zero charge of magnetite lies at pH 7.8, i.e., magnetite has a negative charge above this pH value, and a positive below[111]. This effect is caused by the presence of the solvent ions. The closest neighbors of the surface create an electrical double layer, see Figure 2.3. The surface attracts oppositely charged ions from the solution, which strictly adhere and form a layer which is positively charged. Subsequently, the first layer of the positive ions is attracting a second layer of the negatively charged ions. These negative ions are less dense than the positive ones, but still dense enough to give a total negative charge to the system. In this way the surface is still visible as negatively charged for the environment, but its interactions will be mediated by ions on the surface.

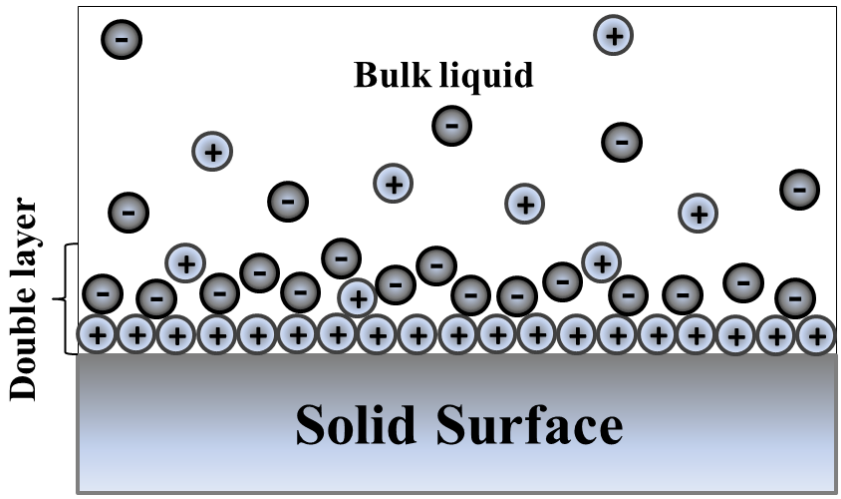

Figure 2.3: Electrical double layer formed in a liquid in a contact with negatively charged surface.

Electrically charged amino acids can bind by electrostatic interactions to the charged areas on the surface. The carboxyl group was found to be the privileged amino acid binding group, due to its deprotonation already at pH greater than around 4.0, which is much smaller than the physiological pH (7.4). This fact is explaining a special role in binding of two negatively charged amino acids: aspartic acid (D) and glutamic acid (E), which have two carboxyl groups each. But in general, all charged amino acids are able to bind to oppositely charged surfaces as a result of electrostatic attraction. However, it is not excluded to reactions of negatively charged amino acids and negatively charged surfaces (coated by solvent ions)[112]. There are two concurrent reactions, first the reaction of the surface with the solvent, and second the reaction of the surface with the amino acid. Reaction between the amino acid and the surface can occur if its pK_a is higher than the pK_a of the reaction between the surface and solvent ions. In such case, the amino acid substitutes solvent ions in the electrical double layer coating the surface.

Hydrogen bonding to some extent can be also considered as an electrostatic interaction[113]. This type of interaction is possible for both protonated and deprotonated forms of the amino acid. The first case was examined by Ikhsan et al. on the example of kaolinite $[Al_2Si_2O_5(OH)_4]$ and aspartic acid (D)[114]. As a result of binding there were reported two products $Al{-}OH_2^+\cdots(HAsp)^-$ and $Al{-}OH^{2+}\cdots(Asp)^{2-}$, depending on the pH of the solution. The second case has been evidenced by Vlasova et al., who considered adsorption of lysine, arginine, histidine and ornithine on the silica surface, and formed $Si{-}O^-\cdots(H_2X)^+$[115].

2.1.2.2 Hydrophobic effects

Hydrophobic effects are taking place when nonpolar compounds are present in aqueous solution. It causes the aggregation of these compounds in a way that the contact-area with water is maximally reduced, and the water molecules are excluded from the inner parts of the system. This effect is important in protein-folding processes, where nonpolar amino acids are maximally "hidden" inside the protein, the charged and polar ones, in turn, are exhibited to the solution. In the group of nonpolar amino acids containing hydrophobic side chains there are alanine (A), valine (V), isoleucine (I), leucine (L), methionine (M), pheny-

lalanine (F), tyrosine (Y), and tryptophan (W). It has been shown that hydrophobic effects should be taken into consideration, e.g., for the description of adsorption of phenylalanine on zeolites, and leucine oligopeptides on the quartz crystals[116,117]. Due to hydrophobic effects nonpolar molecules are mainly insoluble in water, because they are trapped by water molecules in "cages" stabilized by water hydrogen bonds. Additionally, they can be kept together via van der Waals forces. These two effects prevent them from interacting with water[110].

2.1.2.3 Van der Waals interactions

The van der Waals interactions are playing a fundamental role in defining properties of organic compounds such as their solubility in different solvents. They can be attractive or repulsive and vanish quickly at larger distances between atoms. These interactions occur between two atoms that are close to each other, but further apart than the sum of their van der Waals radii. It is caused by perturbations in the electron density of one of them, caused by the presence of the transient dipole in the second. This perturbation is generating a transient dipole in the first atom as well, and both dipoles are weakly attracting[110]. In general, van der Waals interactions are present in all kinds of systems, but they are relatively weak comparing to covalent bonding.

For several systems more than one type of bonding is possible. Such a situation was e.g. noted between silica surfaces and amino acids adsorbed from the gas phase, where both hydrogen and covalent bonds were present[118]. Also in case of phenylalanine with zeolite beta, the amino acid was adsorbed both electrostatically as $HPhe^+$ and specifically through a zwitterionic form[119,120].

2.2 Iron-oxide surface and nanoparticles

Iron-oxide nanoparticles considered in this work are rather built out of various iron oxides, than of a single oxide in a monocrystalline form. That implies specific electronic and magnetic properties. The electronic structure of such composite systems is shortly summarized in the following chapter. Furthermore, besides compounds containing only iron and oxide, also ones doped with manganese or zinc are investigated. Such an addition of other ions can be used for a systematic changing of the magnetic properties of the system.

2.2.1 Structure and magnetic properties of magnetite

Magnetite is an iron oxide with chemical formula Fe_3O_4, and is a member of the oxide spinel group of minerals[121]. This group contains around twenty oxides, which crystallize similarly in the cubic crystal system. The general chemical formula describing compounds belonging to this family is AB_2O_4. The oxide anions are arranged in a cubic close-packed lattice (fcc) and the metal cations denoted as A, and B are occupying the tetrahedral (T_d), and octahedral (O_h) sites in the cell, respectively. More precisely, in the group of metal cations denoted by A, one could find divalent metal cations, like iron, nickel, magnesium, manganese or zinc. It can be also occupied by a quadrivalent lead cation. The second group of cations (B) can contain trivalent ions such as iron, aluminum, chromium or manganese, as well as divalent lead or quadrivalent titanium ions. It is very common in this group of metals to have mixtures of certain percentages of different ions in any particular form,

which is referred to as solid solutioning. That provides a plethora of possible combinations, which manifests various interesting properties[122–124].

A spinel unit-cell is built of eight face-centered cubic (fcc) cells, constructed by cubes with oxygen ions in the corners (in the configuration $2 \times 2 \times 2$). As a whole the unit cell is containing 32 oxygen anions, 8 A metal cations and 16 B metal cations. Depending on the spatial distribution of the cations, one can distinguish between normal and inverse spinels.

In the normal spinel structure the A cations occupy 1/8 of the tetrahedral holes, whereas the B cations occupy half of the octahedral holes. In the inverse spinel structure all of the A ions placed on the tetrahedral sites switch places with half of the B cations placed on the octahedral sites. This gives a general formula of the inverse spinels $B(AB)O_4$, where the first B cation occupies the tetrahedral site, and A and B cations are on the octahedral sites, respectively. Apart from the normal and inverse spinel structures, so-called mixed spinels can be distinguished, forming something between the former ones.

The crystal field stabilization energy (CFSE) is the driving force of the crystallization in either inverse or normal spinel structure of the transition metal oxides. The value of CFSE shows the preference of an ion to stay in the octahedral or the tetrahedral site. For the trivalent metal cations, like, Cr, Mn, Fe, Co, and Ni, in their oxides a high spin electronic configuration is typical due to the weak ligand field of the O^{2-} anion. The general formula describing CFSE is given as,

$$\mathrm{CFSE} = \Delta E = E_{\text{ligand field}} - E_{\text{isotropic field}}, \tag{2.1}$$

where $E_{\text{ligand field}}$ is the energy of the electron configuration in the ligand field and $E_{\text{isotropic field}}$ is the energy of the electron configuration in the isotropic field.

In the magnetite, Fe_3O_4, there are two trivalent cations (3+) and one divalent cation (2+) in one formula unit. In order to decide, which cation is preferred on which site, namely, T_d or O_h, one needs to consider all possible configurations and choose the energetically most stable one. In this case, a normal spinel structure is given as $Fe^{2+}(T_d)[Fe^{3+}(O_h)]_2O_4^{2-}$, and the inverse spinel as $Fe^{3+}(T_d)Fe^{2+}(O_h)Fe^{3+}(O_h)O_4^{2-}$. To choose the preferred one, it is convenient to consider the ligand field splitting of the d-orbitals in tetrahedral and octahedral field for Fe^{2+} and Fe^{3+} ions, see Figures 2.4 and 2.5, respectively, and calculate the CFSE for both of them.

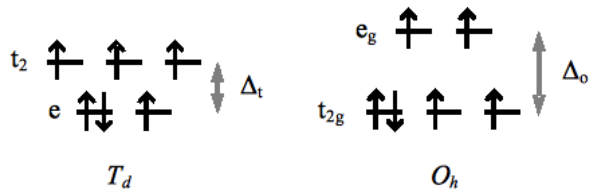

Figure 2.4: d-orbital energy diagram for Fe^{2+} cation both for T_d and O_h symmetric structures

In case of Fe^{2+} there are six d-electrons, which are distributed in high spin configuration in the T_d and O_h diagrams. The crystal field stabilization energy for the tetrahedral

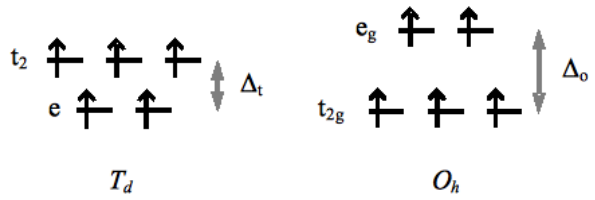

Figure 2.5: d-orbital energy diagram for Fe^{3+} cation both for T_d and O_h symmetric structures

configuration amounts to

$$\left[\left(3\cdot\frac{3}{5}\right)-\left(3\cdot\frac{2}{5}\right)\right]\Delta_t-P=\frac{3}{5}\Delta_t-P, \tag{2.2}$$

where P is the spin pairing energy and it corresponds to the energy needed to pair two electrons on the same orbital. It is assumed to be constant for a given metal and it is not changing with ligand and oxidation state of the metal ion.

Analogously, for the octahedral configuration:

$$\left[\left(4\cdot\frac{2}{5}\right)-\left(2\cdot\frac{3}{5}\right)\right]\Delta_o-P=\frac{2}{5}\Delta_o-P. \tag{2.3}$$

The size of the crystal field splitting of the octahedral structure, Δ_o is at about 9/4 times larger than of the tetrahedral one, Δ_t. It is because of two facts, first in a T_d structure no d-orbitals of the metal point directly at the ligands, and thus there is a lower overlap of the metal and ligand orbitals, also there is a fewer number of ligands in general. This two effects cause the differences in Δ_o and Δ_t. Considering that the crystal field stabilization energy of Fe^{2+} is higher for the octahedral configuration, which makes it preferential.

In case of the Fe^{3+} cation there are five d-electrons to distribute. The CFSE for the tetrahedral configuration amounts to

$$\left[\left(2\cdot\frac{3}{5}\right)-\left(3\cdot\frac{2}{5}\right)\right]\Delta_t=0, \tag{2.4}$$

and for the octahedral

$$\left[\left(3\cdot\frac{2}{5}\right)-\left(2\cdot\frac{3}{5}\right)\right]\Delta_o=0. \tag{2.5}$$

it is identical

Since the CFSE is equal for both configurations, for the Fe^{3+} cation none of them is preferential.

From the analysis of the CFSE for magnetite it turns out, that for the Fe^{2+} cation the octahedral site is preferential, and for the Fe^{3+} both octahedral and tetrahedral are equally preferred, thus we expect that the inverse spinel structure is energetically preferred in this case. Indeed, magnetite at room temperatures crystallizes in the inverse spinel structure, see Figure 2.6.

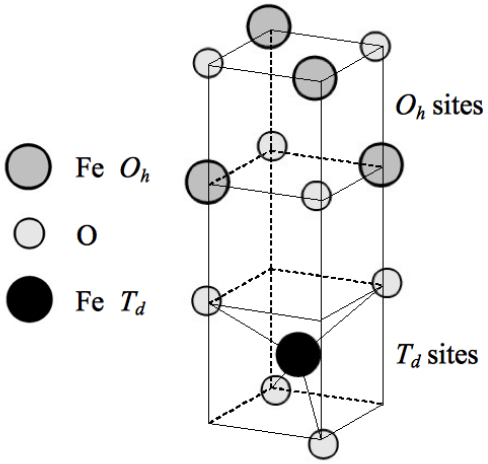

Figure 2.6: Schematic representation of the unit cell of magnetite, built of oxygen ions and iron ions occupying both tetrahedral (T_d) and octahedral (O_h) sites.

The distribution of the high-spin state iron cations manifests in the magnetic properties of magnetite. The magnetic moments at the Fe cations of the T_d and O_h sites are aligned antiparallelly, which results in a ferrimagnetic state, see Figure 2.7. Ferrimagnetism occurs when opposite magnetic moments are not equal and hence a net magnetization remains[125]. In case of magnetite, both Fe^{2+} and Fe^{3+} cations are present in the lattice. Similar properties are observed for ferromagnetics. In this case, the electron spins, and thus the magnetic moments, are aligned in one direction what results in a high net magnetic moment. The magnetic structure of ferrimagnets, in turn, is similar to anti-ferromagnets, in which the electron spins are aligned in opposite directions, but their magnitude is equal, resulting in the compensation of the magnetic moments and hence a zero net magnetic moment.

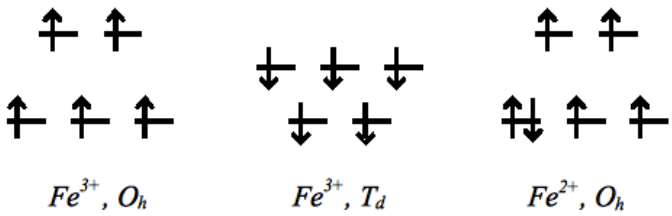

Figure 2.7: Ferrimagnetic ordering of electron spins in a unit cell of magnetite

In Figure 2.7, the antiparallel alignment of the Fe^{3+} ions placed on both the tetrahedral and the octahedral sites is shown. The contributions of the trivalent cations cancel out, and effectively the magnetic moment of the unit cell arises only from the Fe^{2+} ions. As a result, this cation provides a magnetic moment of 4 μ_B, what gives 24 μ_B per unit cell in cell[126].

In the considered inverse spinel structure of magnetite the octahedral sites are occupied both by Fe^{2+} and Fe^{3+} cations. However, it was observed with Mössbauer spectroscopy that at 300 K a rapid electron exchange (of the order of 1 ns) between the two octahedral sites takes place[121]. Therefore it was not possible to determine unambiguously by which ions,

either Fe^{2+} or Fe^{3+}, these sites were occupied. Effectively, a charge of 2.5+ was assigned to both octahedral sites. The same result was obtained by Noh et al., who investigated the electronic structure of magnetite theoretically by means of DFT methods [127]. Furthermore, they noticed that for different DFT exchange-correlation functionals, both situations, either having Fe^{2+} and Fe^{3+}, or only $Fe^{2.5+}$ ions on the octahedral sites, are possible. More specifically, range separated functionals HSE06 and HSE(15%) can give either distinct Fe^{2+}/Fe^{3+} or delocalized $Fe^{2.5+}$ case, respectively. With a PBE+U approach, also the latter delocalized results was obtained.

2.2.2 Compounds containing iron and other metal centers – ferrites

Ferrites are a group of minerals that contain all compounds which can be described by the formula $Me^{2+}Fe_2O_4$. Magnetite is one of the group members, but Fe^{2+} can be also replaced by other divalent ions, such as zinc (Zn^{2+}), manganese (Mn^{2+}), magnesium (Mg^{2+}), cobalt (Co^{2+}) or nickel (Ni^{2+}). Ferrites can form either normal or inverse spinel structures, but also mixtures of these two types, so-called mixed spinels, are observed. The preference of a certain spinel structure is determined by the crystal field stabilization energy of the divalent ion in the structure (Me^{2+}), since the CFSE of the Fe^{3+} cation is equal both for the tetrahedral and octahedral position, see Chapter 2.2.1. Hence, normal spinel structures are likely when the divalent ion energetically prefers the tetrahedral position. Also, when the stabilization energies for the non-iron and iron cations are equal, and the size of the former fits better than the Fe^{3+} (d^5) ion to the tetrahedral site, a normal spinel structure is observed. This occurs for Zn^{2+} (d^{10}) in $ZnFe_2O_4$. Inverse spinels are formed in opposite cases, i.e., when the divalent ion prefers to occupy an octahedral site, or if its size fits better to this site than the size of Fe^{3+}, when both have equal CFSE energies. Here, compounds containing Fe^{2+}, Co^{2+}, and Ni^{2+} cations are found. The group of the mixed spinel structures consists of $MnFe_2O_4$ and $MgFe_2O_4$, as all ions in these compounds have zero CFSE and thus no preferential site.

2.2.3 Iron oxide magnetic nanoparticles

One of the main topics in this thesis is the simulation of the interactions of iron oxide magnetic nanoparticles (IOMNPs) with peptides. IOMNPs are spherical nanocrystals, containing Fe^{2+} and/or Fe^{3+} ions, of typical size between 1 and 100 nm. Due to the magnetic nature of iron oxides, such nanoparticles can be manipulated using an external magnetic field. The iron magnetic nanoparticles may be divided into two main types: oxides and alloys. The oxidic nanoparticles can be obtained from the naturally occurring iron oxides, or easily synthesized. From the huge variety of oxides, for biotechnology and bioengineering applications mainly magnetite (Fe_3O_4), hematite ($\alpha-Fe_2O_3$) and maghemite ($\gamma-Fe_2O_3$) are used [30]. These oxides meet the following requirements: sufficient size (smaller than 100 nm), biocompatibility, large surface area, stability in high temperatures, high enough magnetic moment, low toxicity, stability in physiological conditions, and also a cost effective synthesis [27,29,33,128,129]. The surface of IOMNPs can be coated by organic or inorganic materials, such as biomolecules, silica, polymers, and many others [30,130–136]. This is called functionalization. For applications in biomedicine, such a coating has to be non-toxic and biocompatible. It can be successfully used for a targetable delivery, e.g., of a drug, where the

nanoparticles carrying a bioactive substance are homed to a specific part of the organism [27].

Besides the general applications of peptides with inorganic surfaces presented in Chapter 1.1, there are additional benefits of functionalized IOMNPs, which arise from their magnetic properties. For that reason, they are widely used as magnetic resonance imaging (MRI) contrast agents for in vitro diagnostics [27,30,137–142] or in bioseparation [27,30,132]. In magnetic hyperthermia, the IOMNPs are transported to cancer cells and produce heat under the stimulation of an alternating magnetic field [136,143–152]. This kind of treatment is destroying cancer cells, which are more sensitive to higher temperatures than healthy ones. Still the heat should be selectively delivered to the tumor area in order to avoid overheating of healthy tissues in the body, and this can be achieved with the specific transport agents present on the surface. An additional advantage of the magnetic properties of the IOMNPs in the cancer treatment is the possibility of transporting them into certain part of the organism with an external magnetic field.

The magnetic properties of the IOMNPs manifest interesting behavior strongly related to the size of the nanoparticle [30,153]. This behavior is schematically presented in Figure 2.8, where using the concept of magnetic domains, a dependence between the size and the magnetic properties is presented. Here, coercivity (Hc) is a useful parameter to monitor. When the size of the nanoparticle reaches a critically small value it becomes a single domain. In this case, it is assumed that magnetization is uniform for the entire nanoparticle. Up to a certain diameter (D_{SP}) a superparamagnetic behavior is observed. Superparamagnetism in nanoparticles is caused by thermal effects, which are strong enough to spontaneously demagnetize them. Material possessing such properties can be magnetized due to the presence of an external magnetic field. This kind of behavior is likely in living cells, because magnetic properties are "switched on" when needed only. With increasing size up to D_{SO}, also the magnetic coercivity is growing corresponding to a ferromagnetic character. Out of many materials exhibiting ferromagnetism (Fe, Co, Ni, and others), magnetite is the most magnetic of all crystals occurring in nature. For all biological applications it is used in its superparamagnetic form [154–156]. Above this limits more than one magnetic domain appear in the nanoparticle, and the multidomain character leads to the decrease of the coercivity, due to effective cancellation of the magnetic moments. For nanoparticles of bigger size, in the multi-domain range, the magnetization is nonuniform [157–159].

Synthetic magnetite nanoparticles, with a size varying from 7–18 nm are mostly superparamagnetic. In nature, however, bigger crystals of magnetite, being part of magnetosomes, are observed. Magnetosomes are unique prokaryotic organelles synthesized by magnetotactic bacteria [160–165]. The size of these crystals varies from 10–60 nm what places them in the single magnetic domain range, see Figure 2.8, yet with ferromagnetic properties. This specifically large size of magnetosome magnetite crystals arises from the strict control of biomineralization carried out by bacteria. Natural magnetic nanoparticles differ from the synthetic ones not only by the characteristic magnetic properties, but also by other features, e.g., the chemical groups present on surfaces are different. On the surface of synthetic NPs only hydroxyl groups are observed, while on the natural ones primarily amino and carboxyl groups are found. The latter groups are very convenient concerning linking of small biomolecules to the surface. These specific properties of the magnetosome magnetite NPs suggest that they could be widely used in various fields such as biomedical applications, e.g., for magnetic drug and gene delivery systems [6,8,10–12].

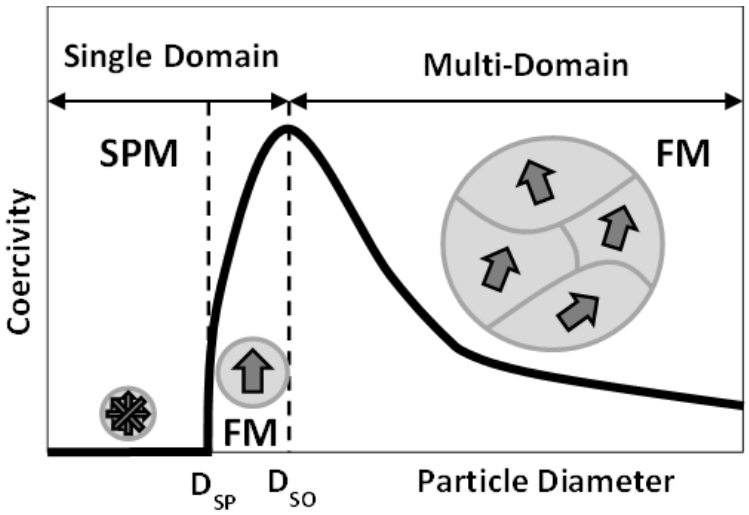

Figure 2.8: Schematic illustration of the coercivity-size relation in IONP. SPM denotes superparamagnetic NPs, and FM ferromagnetic NPs. Adapted with permission from *Pharmacological Research*, **2010**, 62(2), 126–143. Copyright 2010 Elsevier.

2.2.4 Surface of magnetite and magnetic nanoparticles

Compounds made of iron and oxygen can form many different structures, depending on concentration, distribution, oxidation state of iron and presence of hydroxyl groups in the crystal structure[166]. This groups consists of sixteen compounds being oxides and hydroxides, such as wüstite (FeO), hematite ($\alpha-Fe_2O_3$), maghemite ($\gamma-Fe_2O_3$), goethite ($\alpha-FeOOH$), akaganeite ($\beta-FeOOH$), lepidocrocite ($\gamma-FeOOH$) and magnetite (Fe_3O_4). As reported in literature, many of those can be found on the surface of magnetic nanoparticles (MNPs) in higher or lower percentage, depending on conditions.[167]. The experimental determination of the surface termination of the MNPs is complicated, and an unambiguous assignment is difficult as the actual termination is sensitive to the conditions, like, solvent type, temperature, pH, etc. The basic experimental tool to characterize the crystal structure, and the composition in terms of types of magnetic iron oxides, of magnetic nanoparticles is X-ray powder diffraction (XRD) technique[30].

Crystal structures of individual iron oxides can be more or less complex, e.g., the simplest one is wüstite (FeO), which crystallizes in an NaCl-like structure, with cubic crystal system and the same number of iron ions (2+) and oxygen ions occurring alternately. To build a model of the wüstite surface in the water solution, one needs to consider additionally OH groups which cover the surface[168]. It is also the case for other iron oxides, due to presence of Nernst layer formed in aqueous solution, as described in Chapter 2.1.2.1. For magnetite nanoparticles Tombacz et al. showed that water adsorbs on the surface both experimentally and theoretically[169].

In nanoparticles, iron oxides have inhomogeneous surfaces with defects in the form of kinks, adatoms, vacancies, terraces and steps, see simplified block model of various defects presented in Figure 2.9.

The composition of the synthetic crystals is determined during annealing processes, when the iron oxides can be transformed in each other by oxidation or reduction. This indicates how closely related the various iron oxides are, e.g., the structures of maghemite ($\gamma-Fe_2O_3$)

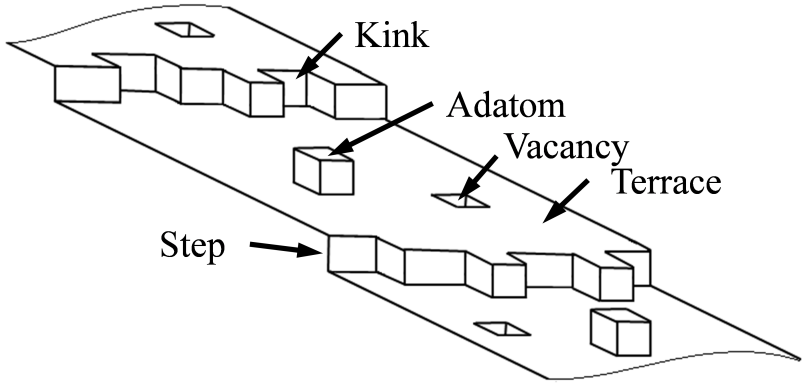

Figure 2.9: Simple block model of defects on single-crystal surface. Adapted with permission from *Chemical Reviews*, **1999**, 99(1), 77–174. Copyright 1999 American Chemical Society.

and magnetite (Fe_3O_4) are very similar, and therefore maghemite can be considered as a fully oxidized magnetite[30]. Hematite ($\alpha-Fe_2O_3$), n turn, is the most stable, i.e., maximally oxidized, iron oxide and can be used to synthesize both maghemite and magnetite[170]. Magnetite can be prepared in various conditions what results in different surface faces, including (100), (111), (110), (311), (331), and (511)[171–175]. The most stable surface of magnetite is the (111) surface, with three possible terminations[176]. These terminations can be related to different positions of the slice through the bulk structure, see Figure 2.10 for the unit cell of the (111) surface. Depending on the conditions of the sample preparation, only one of those terminations, or a few of them simultaneously, is observed[176–179]. This makes the interpretation of the data from experimental techniques complicated. The various terminations of the surface find also reflection in the reactivity. It was found that oxygen-terminated surfaces are inert, while iron-terminated ones reactive toward adsorbates like H_2O and CCl_4[178–180].

The (111) surface of a naturally grown Fe_3O_4 single crystal was investigated using scanning tunneling microscopy (STM) and scanning tunneling spectroscopy (STS) combined with first-principles calculations[176]. STS is an extension of STM and it is providing information about the density of electrons as a function of their energies. It was found that the commonly observed surface termination is Fe_{tet1}, with iron ions on tetrahedral positions, see Figure 2.10. The existence of the terminations with iron ions on octahedral positions, namely Fe_{oct1} and Fe_{oct2}, was confirmed only for systems prepared under oxygen-poor conditions. The thermodynamic stability and electronic structure of different (111) surface terminations was also studied theoretically, by use of first principles DFT calculations[181]. It was found that surfaces modified with point defects and adatoms are close in surface energy and they can be more stable than bulk-like terminations.

Additionally, as mentioned before, in solution the iron-oxides surfaces are coated by solvent ions. Therefore, to investigate the interactions of such surfaces with organic molecules a proper description of the surface, including all mentioned effects, is required. However, an explicit treatment of these contributions is very difficult and leads to computationally inefficient models. In order to address these problems, we have developed a computational model, the Effective Implicit Surface Model (EISM), which is using an implicit representation of the surface, see Chapter 3.4 for a detailed description.

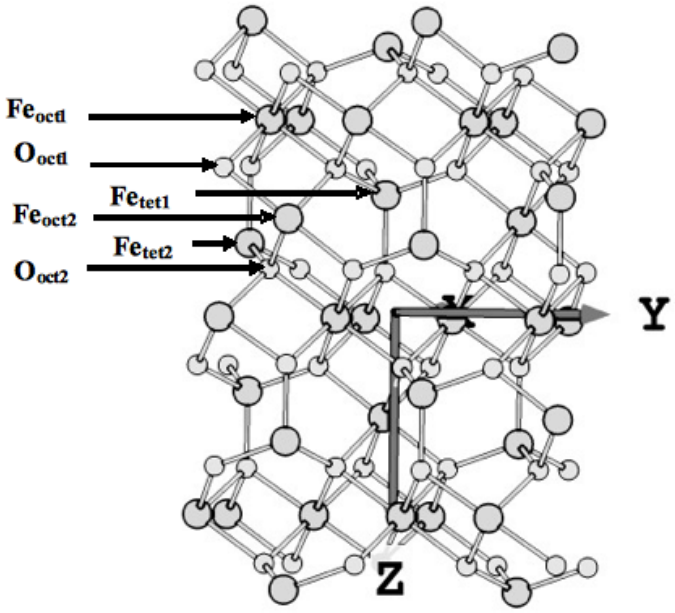

Figure 2.10: Unit cell of the (111) magnetite surface, positioned in z-direction perpendicular to the surface. Planes containing tetrahedral and octahedral iron ions are denoted as Fe_{tet} and Fe_{oct}, respectively. Numbers 1 and 2 denote different surrounding for atoms of the same type.

2.3 Experimental methods providing large sets of peptide sequences

In order to test theoretical models describing peptide-surface interactions experimentally, a large set of different peptide sequences needs to be provided. Peptide array screening is the main experimental technique used by the experimental collaborators at TUM to assess the binding affinity of peptide sequences to magnetite nanoparticles. The results obtained with this method became a basis for the theoretical investigations presented in this thesis. In Chapter 5.1, a theoretical model is introduced which allows to explain the peptide-screening results, i.e., the binding between charged peptides and magnetite nanoparticles under different conditions. In Chapter 5.2, in turn, I am using the peptide-screening data from a membrane containing different homopeptides to calibrate the EISM model. Also in Chapter 5.2, this model is used for calculating Gibbs free energies of binding for the heteropeptides stored on a second membrane, which are then compared with the experimental results.

2.3.1 Peptide array screening

In the peptide array screening experiment a membrane covered with various peptides is washed with a buffer solution containing nanoparticles. Each peptide, in a desired amount, is placed on a separate spot on the membrane. Next, the binding affinities between the peptides and the nanoparticles are measured. One can estimate the binding by observing the change of the color intensity for a respective spot, before and after washing the membrane with the nanoparticle solution. This change is visible, due to the photo activity of the

nanoparticles, which is influenced by the adsorption. The magnitude of the change in the color intensity is proportional to the binding affinity. A picture of one of the arrays, investigated by the group from TUM, is shown in Figure 2.11. Two peptide arrays were designed for the peptide screening experiment to particularly analyze the peptide-magnetite interactions. The first membrane was containing mostly hexa-homopeptides, built up by all amino acids. The second membrane was containing various heteropeptides, consisting mostly of amino acids which presented strong binding affinity in the first experiment.

Both membranes were prepared by the Intavis Company in CelluSpot procedure, using an instrument called Slide Spotting Robot. In this procedure, the arrays of peptides are synthesized on a planar surface, e.g., a glass slide, with a support of modified cellulose. The C-termini of the individual peptides are bound to cellulose via covalent bonds and spotted on the chosen surface. After solvent evaporation, a three-dimensional layer is formed. In this method at most 384 peptide spots can be printed on a single membrane.

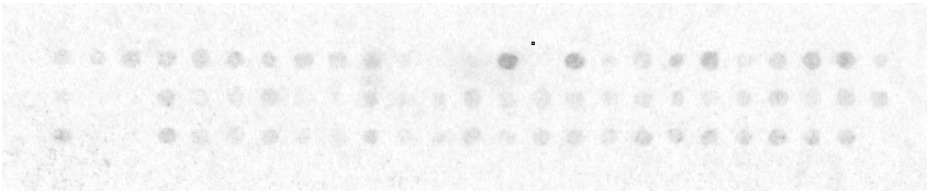

Figure 2.11: The example peptide-array membrane after the screening procedure. The darker the spot color, the stronger affinity of the particular peptide to the nanoparticles. Made by Silvia Blank-Shim (TUM).

The characteristics of the binding affinities for specific peptides depend on the buffer solution, as well as the type of the nanoparticles. The peptide array screening experiment was carried out in different buffers and at different pHs, what was found to significantly influence the observed results. More details about the experimental conditions and results can be found in Chapters 5.1 and 5.2. In Figure 2.12, one set of experimental results for the first membrane, containing only homopeptides, in phosphate buffer and different pHs is shown.

The horizontal red line in Figure 2.12 denotes the background noise level of this particular experiment, as one can see its value is rather high. It is done by calculating the standard deviation of the darkness of the spots which are empty, i.e., do not contain any peptides. The noise level in peptide-array screening has to be calculated separately for each experiment.

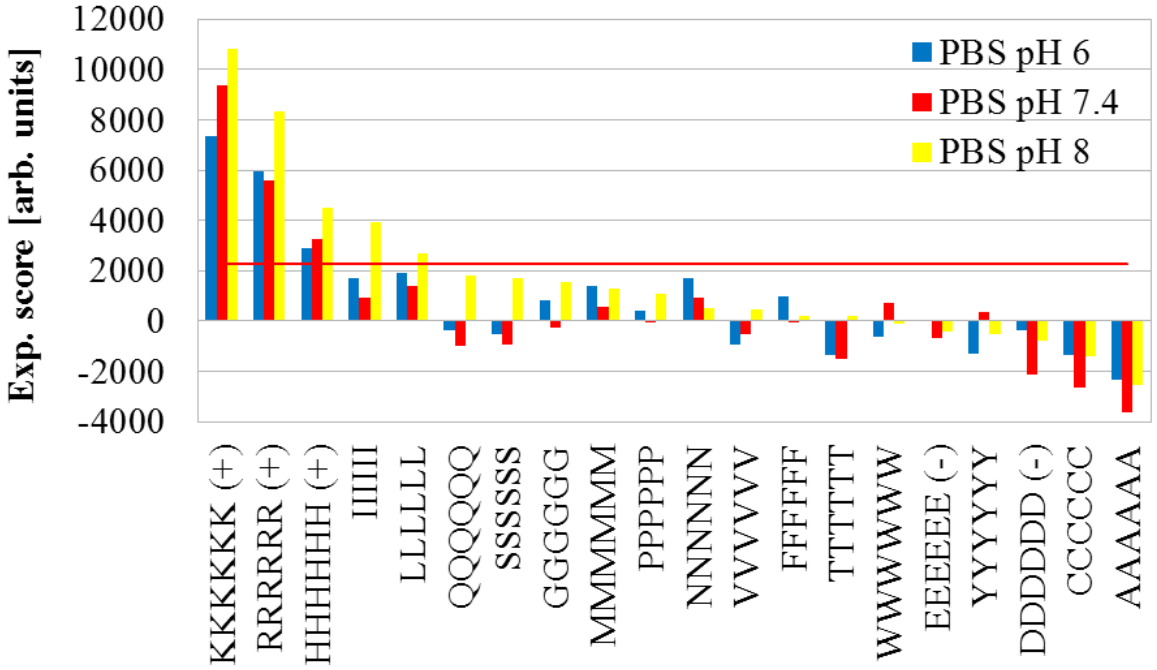

Figure 2.12: The experimental scores of binding affinities of homopeptides to magnetite nanoparticles in phosphate buffer solution and three different pH.

3 Methods

The results presented in this work were obtained mainly by using two computational methods for simulations, i.e., molecular dynamics (MD)[69–71] and the Metropolis Monte Carlo method (MC)[182]. MD simulations were used in order to relax the structures of the peptides in presence of the explicit solvent molecules but without the surface. This was performed to equilibrate the system prior to the essential free-energy calculations, namely to obtain a relaxed peptide structure in solution. These calculations were performed by means of the GROMACS package[183,184]. To investigate the interactions of peptides with inorganic surfaces, Metropolis Monte Carlo simulations, implemented in the SIMONA package[185], were applied in this work. The force field used in the calculations was defined with the EISM model, in which both the solvent and the surface are described implicitly, see Chapter 3.4 for details. In order to explore a large part of the free energy surface and to speed up the calculations, the metadynamics procedure available in the PLUMED package was applied[186], see Chapter 3.3 for details. To reduce the numerical error, the profile of the Gibbs free energy of binding was computed twenty times for every single peptide sequence in particular environment, and an average of those 20 runs was taken as the final result. Each simulation had 4 millions of steps and was carried out in 300 K.

3.1 Molecular dynamics

This method is, in most cases, based on solving the classical (Newton's) equation of motion numerically, for groups of interacting atoms (particles),

$$\vec{F}_i(t) = m_i \cdot \frac{\partial^2 \vec{r}_i}{\partial t^2} \tag{3.1}$$

where, m_i represents the mass of the atom i, and $\vec{r}_i$ its position[70,184]. For a given arrangement of atoms, the forces can be obtained from a molecular-mechanics force field and interatomic potentials[69,71]. Based on these forces, the trajectory following the dynamical evolution of the system is obtained.

The number of particles describing naturally occurring processes, and hence the number of degrees of freedom, is usually way too large to solve the problem analytically, and thus numerical methods are essential for MD. One of the widely used integration techniques is the Verlet-Störmer algorithm[187]. For each time step (Δt) the atomic coordinates and velocities of the atoms are calculated. However, during long simulations some numerical errors can occur and accumulate, what leads to an unphysical behavior of the investigated systems. This can be reduced by a proper selection of algorithms and parameters.

Molecular-dynamics-based methods still require relatively long runs for well equilibrated simulations. Therefore, it is also problematic to find a good compromise between the accuracy, the scale of the studied system, and the computational resources. In modern MD

simulations, both the maximal number of atoms and the maximal length of the simulations are not strictly defined. Typically runs for 10^2–10^8 atoms simulated for over 10 ps–100 ns are feasible. The size of the investigated system is limited mostly by the computational cost of the calculation of the forces. Concerning the real-time scale, the MD simulations are time consuming and additionally limited to systems with well-defined structures. Also, relatively long runs are required to probe a large enough part of the phase space, and thus fulfill the ergodicity condition. For the systems investigated in this thesis, the biggest difficulties arise from the huge number of atoms in the surface, and its proper description. Therefore we decided to use implicit models for the solvents and the surfaces[188,189]. In such implicit models, the surrounding of the investigated system is replaced by different dielectric regions. The interactions are captured by an additional external potential, and only the forces between atoms within the molecule have to be computed explicitly.

In this work, the AMBER99SB*-ILDN force field[190–192], provided in the GROMACS package, was used to describe the energies of peptides in vacuum. The peptide sequences were built with the molecular graphic system PyMOL[193]. For defined peptide structures, the topology files were constructed by GROMACS, to obtain the atomic coordinates, and define the force-field parameters, i.e., atomic bonds, atomic angles, torsion angles, atom types, residue types, atomic charges and masses. For each atom type present in the structure, the Lennard-Jones parameters were assigned as well.

3.2 Metropolis Monte Carlo

Monte Carlo is one of the methods which can reduce the computational cost of the MD simulations, as it can more effectively probe the phase space. However, at the same time the information about the time evolution of the investigated process is lost, and thus an access to time-dependent properties, like, vibrational spectra, is lost. Considering processes in which the time scale is not the main problem of interests, such as investigations of the interaction strength, MC can outperform MD simulations.

In Monte Carlo methods, changes in the positions of atoms in the structure are not driven by the forces on these atoms, as it is the case for MD, but the next-step structure is chosen from a randomly proposed set of structures. MC methods sample the property of interest by weighting each structure with a Boltzmann distribution. For each structure the probability-weighted contribution is calculated. This procedure was later on modified by Metropolis et al.[182], who proposed that the sets of structures are assessed by their Boltzmann probability and that the property is averaged over the set of accepted structures. The Metropolis MC algorithm is schematically presented in Figure 3.1. We start from the structure $R^{(i)}$, generate a random structure $R^{(t)}$, and evaluate the Boltzmann probability $\pi_{i\to t}$, Eq. 3.2, of the transition from the old to the new structure, and compare this probability with a random number r.

$$\pi_{i\to t} = \begin{cases} e^{\frac{\Delta E_{it}}{k_B T}} & \Delta E_{it} > 0 \\ 1 & \Delta E_{it} < 0 \end{cases} \tag{3.2}$$

If the Boltzmann probability of transition is larger than the random number, the move is accepted, if not we go back to the initial structure $R^{(i)}$. At the end, a set of conformations is obtained and the expectation value of the desired property is calculated as an arithmetic

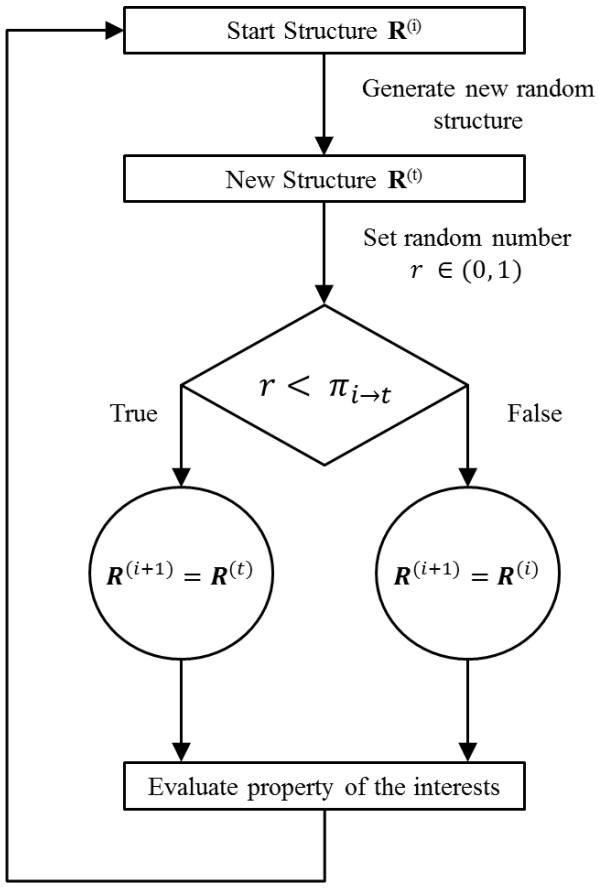

Figure 3.1: The block scheme of the Metropolis Monte Carlo Method.

average of its value for N individual accepted structures,

$$\langle E \rangle = \frac{1}{N} \sum_{i=1}^{N} E_i. \tag{3.3}$$

3.3 Metadynamics

As it was mentioned in Chapter 1.3, many methods of speeding up the computational simulations, like, umbrella sampling, or thermodynamic integration, require information about the reaction path between the substrate and the product. This requires some experience and intuition to provide a proper guess, but also constrains the simulation. In situations, where a larger area of the free energy landscape is of interest, metadynamics is a more suitable approach[100].

To describe what metadynamics is one can poetically say that it corresponds to filling the free energy wells with "computational sand"[194]. In general this method uses collective variables (CVs) to reduce the number of degrees of freedom and control the direction of the simulation. The CVs are defined as a few selected degrees of freedom in space $\mathbf{s}(q)$. The simulation is biased by a history-dependent potential $V(\mathbf{s}, t)$ constructed as a sum of

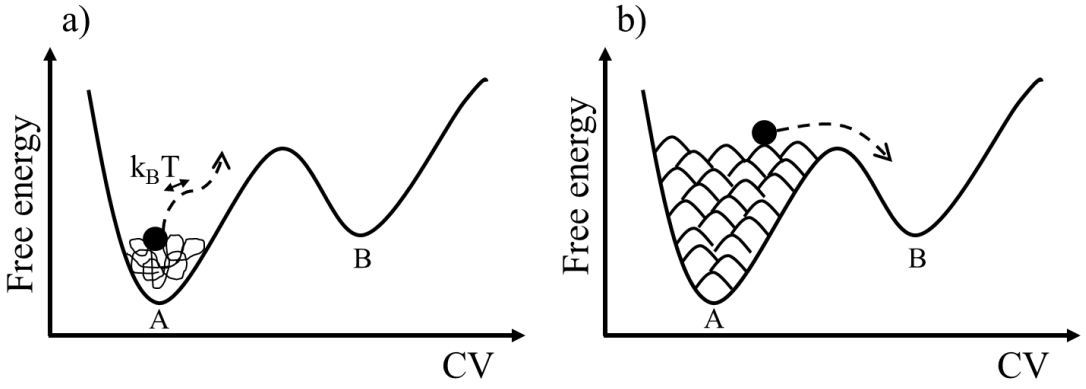

Figure 3.2: Schematic comparison of the classical MD (a) and metadynamics (b), where the addition of Gaussians to the potential makes it possible to escape local minima on the free energy surface.

Gaussians centered along the trajectory in the collective variable space:

$$V(\mathbf{s},t) = \sum_{k\tau<t} W(k\tau) \exp\left(-\sum_{i=1}^{d} \frac{(s_i - s_i(q(k\tau)))^2}{2\sigma_i^2}\right), \tag{3.4}$$

where τ is the frequency of Gaussian deposition, σ_i the width of the Gaussian for the i-th CV, and $W(k\tau)$ the height of the Gaussian.

Due to the Gaussians added along the trajectory, the system avoids already visited points of the space, and the metadynamics bias potential is pushing the system away from the local minima to visit new regions of the phase space. In Figure 3.2 a comparison of the MD with (a) and without metadynamics (b) is shown. One can compare how addition of Gaussians in metadynamics is helping to escape one minimum and explore another one. In the case of usual MD, where changes in geometry depend on the temperature, an average energy difference between two steps (roughly k_BT) is much smaller than the energy barrier. Thus it may happen that the system is not able to escape the minimum, and go over the barrier.

3.4 Effective Implicit Surface Model (EISM)

The prediction of peptide sequences manifesting desired properties in interactions with inorganic surfaces is still a computationally demanding task. For this purpose an efficient computational protocol for evaluation of the binding affinity between peptides and surfaces is needed. To this end, a computational protocol based on the SIMONA-PLUMED engine, performing Monte Carlo calculations, supported by metadynamics, using force-field methods as a description of the system, was used. However, an explicit representation of the inorganic surface is computationally very demanding. To address this problem, a new model describing the peptide-surface interactions implicitly, namely, the Effective Implicit Surface Model (EISM) was developed.

The description of the peptide-surface interactions introduced in the EISM model allows

for a quick and yet accurate enough calculation of the energy, which allows to distinguish between strong and weak binding sequences. In this empirical model, all water- and surface-related degrees of freedom are integrated out, and represented in an implicit manner.

The total energy of the system consists of five terms:

$$E = E_{\mathrm{INT}} + E_{\mathrm{SLIM}} + E_{\mathrm{SASA}} + E_{\mathrm{SLJ}} + E_{\mathrm{PIT}}. \tag{3.5}$$

The first term (E_{INT}) contains the standard interactions of a peptide in vacuum, i.e., Lennard-Jones (LJ), Coulomb and dihedral terms as described by a typical force-field, the second term (E_{SLIM}) is used to model the electrostatic desolvation of the peptide close to the surface, the third term (E_{SASA}) is including the empirical description of the peptide-surface interaction. The fourth term (E_{SLJ}) describes the Lennard-Jones interaction between peptide and surface and is mainly used to keep the peptide from entering into the surface. The fifth term (E_{PIT}) keeps the peptide within a cubic box around the surface and pushes it back when it approaches the borders of the box. A schematic picture of the EISM model, showing the peptide above the implicit surface is given in the Figure 3.3. Each of the energy terms will be described in details in the following.

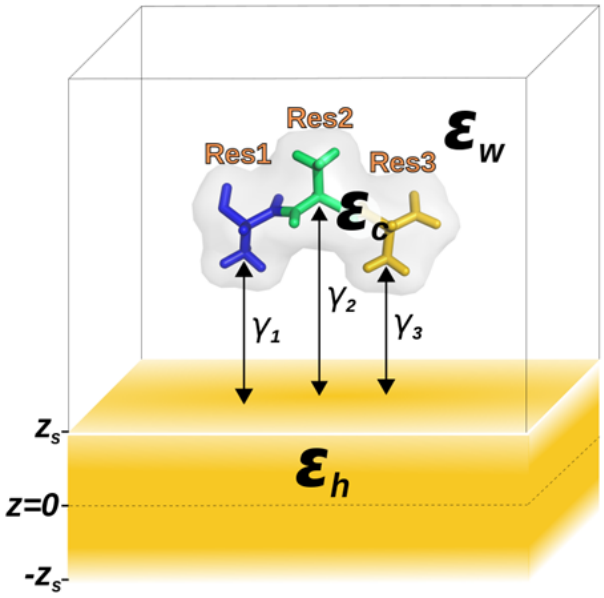

Figure 3.3: Schematic representation of the EISM model. Some of the key parameters and regions in the model for the description of the peptide-surface interactions are denoted. The surface is characterized by its dielectric constant ε_{h} and thickness z_{s}. Also, the peptide and water are characterized by their dielectric constants, ε_{c} and ε_{w}, respectively. γ_i denotes an empirical parameter describing binding affinity of the i-th residue to a given surface under certain conditions.

3.4.1 Energy of the peptide in vacuum, E_{INT}

The energy of the peptide in vacuum, E_{INT}, stands for its standard interactions as defined by a usual force field. The assignment of parameters is defined for all atoms in the pep-

tide's structure by the AMBER99SB*-ILDN [190–192] force field provided in the GROMACS package [183,184]. For the desired peptide sequences, the topology files are constructed. Such files contain information about atomic coordinates, atomic bonds, atomic angles, torsion angles, atom types, residue types, Coulomb terms (charges) and masses. For each type of atom, the Lennard- Jones parameters are assigned as well. AMBER (Assisted Model Building and Energy Refinement) refers to a set of molecular mechanics force fields for the simulation of biomolecules. The AMBER99SB*-ILDN force field was chosen to describe peptides in this work. It provides accurate amino acids side-chain torsion potentials [192].

The E_{INT} term describes a potential energy of the peptide in vacuum and consists of two terms, defining bonded and nonbonded interactions,

$$E_{\mathrm{INT}} = E_{\mathrm{bonded}} + E_{\mathrm{nonbonded}}. \tag{3.6}$$

In the bonded part, the terms for the atoms which are connected by torsion angles, and for the 1-4 interactions are included. It does, however, not include atomic-bond, and valence-angle terms.

$$E_{\mathrm{bonded}} = E_{\mathrm{dihedral}} + E_{1-4} + E_{\mathrm{bond}} + E_{\mathrm{angle}} \quad \text{where} \quad E_{\mathrm{bond}}, E_{\mathrm{angle}} = 0. \tag{3.7}$$

The short-range interactions, E_{dihedral} and E_{1-4}, considered in the E_{bonded} term are the geometry of the system. E_{dihedral} describes two types of dihedral angles. First, the torsion potentials around covalent bonds, the so-called proper dihedral angles, see Figure 3.4,

$$E^{\mathrm{proper}}_{\mathrm{dihedral}}(\theta) = \sum_{n=1}^{4} k_{\theta,n}(1 + \cos(n\theta - \theta_n)), \tag{3.8}$$

where θ is the angle, and the coefficients $k_{\theta,n}$ and θ_n are force constant of the cosine potential, and equilibrium angle of this potential, respectively. Second, the improper dihedrals, which

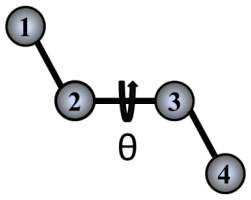

Figure 3.4: Schematic representation of the proper dihedral angle.

prevent the deformations of the planar chemical formations or rings, see Figure 3.5,

$$E^{\mathrm{improper}}_{\mathrm{dihedral}}(\theta) = \frac{k_\theta}{2}(\theta - \theta_0)^2, \tag{3.9}$$

where θ is the improper dihedral angle, k_θ is the force constant, and θ_0 is an optimal improper dihedral angle.

The last term,E_{1-4}, includes nonbonding interactions of two end atoms of a torsion angle. In this term, the Lennard-Jones and Coulomb interactions between two atoms (i and j)

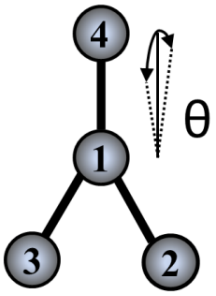

Figure 3.5: Schematic representation of the improper dihedral angle.

separated by three covalent bonds are considered.

$$E_{1-4}(i,j) = f_{\mathrm{LJ}} E_{\mathrm{LJ}}(i,j) + f_{\mathrm{Coulomb}} E_{\mathrm{Coulomb}}(i,j), \tag{3.10}$$

where f_{LJ} and f_{Coulomb} are constant scaling factors used to scale LJ and Coulomb interactions of atoms i and j, respectively.

The nonbonded (non-covalent) energy term includes the long range interactions, such as electrostatic and van der Waals forces:

$$E_{\mathrm{nonbonded}} = E_{\mathrm{electrostatic}} + E_{\mathrm{vanderWaals}}. \tag{3.11}$$

To this term belong electrostatic interactions described by Coulomb forces between partial charges (q_i) assigned to every atom. These partial charges are fitted in such a way that they reproduce the electrostatic potential from the nuclei and the electron density around the molecule properly. The total Coulomb force is given by

$$E_{\mathrm{Coulomb}} = \frac{1}{4\pi\varepsilon_0\varepsilon_s} \sum_{i<j}^{N} \frac{q_i q_j}{r_{ij}}, \tag{3.12}$$

where ε_0 is the permittivity of the vacuum, ε_s is the assumed dielectric constant in the molecule, and r_{ij} is a distance between atoms i and j, q_i and q_j are their partial charges, N is the total number of atoms in the system.

The second term of the long-range interactions is defined by the Lennard-Jones potential which describes van der Waals forces[195]. These forces are including Pauli repulsions of overlapping electronic orbitals and dispersion attraction of induced electrostatic dipoles. The Lennard-Jones potential is given as

$$E_{\mathrm{LJ}} = 4 \sum_{i<j}^{N} \epsilon_{ij} \left(\left(\frac{\sigma_{ij}}{r_{ij}} \right)^{12} - \left(\frac{\sigma_{ij}}{r_{ij}} \right)^{6} \right), \tag{3.13}$$

where i and j denote two atoms of the molecule, r_{ij} is the distance between them, ϵ_{ij} and σ_{ij} describe the interaction of two atoms represented by atom-type dependent Lennard-Jones parameters (ϵ and σ), see Eqs. 3.14 and 3.15, and N is the total number of atoms in the

system.

$$\epsilon_{ij} = \sqrt{\epsilon_i \epsilon_j}, \tag{3.14}$$

$$\sigma_{ij} = \frac{1}{2}(\sigma_i + \sigma_j), \tag{3.15}$$

where ϵ_{ij} is the depth of the potential well between atoms i and j, and σ_{ij} is the finite distance at which the potential between atoms i and j is equal to zero, see Figure 3.6.

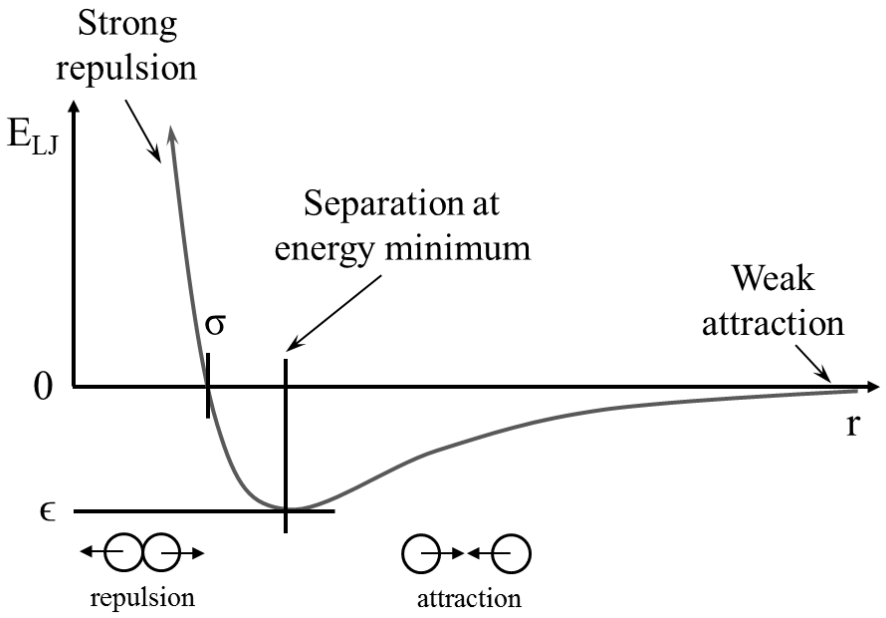

Figure 3.6: Schematic representation of the Lennard-Jones interatomic potential, where r is the distance between the atoms, σ and ϵ are the Lennard-Jones parameters.

3.4.2 The SLIM energy term

The E_{SLIM} term refers to the SLIM model[196], which is used to model the desolvation of the peptide close to the implicit surface. SLIM is the abbreviation of SIMONA Layered Implicit Membrane, similarly to the implicit solvent models it offers the possibility of reduction of the computational cost of simulations.

The SLIM energy term introduces the implicit definition of the surface and solvent to the EISM model. The SLIM model is defined in a way to improve the generalized Born implicit solvation model, which is limited to the presence of only two different dielectric regions. With SLIM, more than two dielectric regions can be considered. Born proposed a model of ion hydration[197], which can be written in the form

$$\Delta G_{\mathrm{B}} = -\frac{1}{4\pi\varepsilon_0}\left(\frac{1}{\varepsilon_{\mathrm{s}}} - \frac{1}{\varepsilon_{\mathrm{w}}}\right)\frac{q^2}{R}, \tag{3.16}$$

where ΔG_{B} is solvation free energy of an ion with charge q, and dielectric constant ε_{s}, ε_{w} is

the dielectric constant of a water, R is the Born radius, which is determined experimentally as the amount of polarization induced by the ion's charge surrounded by solvent. The extension of the generalized Born model from ions to molecules was proposed by Still et al[189].

$$\Delta G_{\mathrm{GB}} = -\frac{1}{4\pi\varepsilon_0}\left(\frac{1}{\varepsilon_{\mathrm{s}}} - \frac{1}{\varepsilon_{\mathrm{w}}}\right)\sum_{i<j}^{N}\frac{q_i q_j}{r_{ij}}\frac{1}{f_{\mathrm{GB}}(r_{ij}, R_i, R_j)}. \tag{3.17}$$

Again, ε_0 is the permittivity of the vacuum, ε_{s} is the dielectric constant in the molecule, ε_{w} is the dielectric constant of water, and r_{ij} is the distance between the atoms i and j, q_i and q_j are their partial charges, R_i and R_j their Born radii, N is the total number of atoms in the system, the f_{GB} is a factor which scales the interaction terms $i \neq j$:

$$f_{\mathrm{GB}}(r_{ij}, R_i, R_j) = \sqrt{1 + \frac{R_i R_j}{r_{ij}^2}\exp\left(-\frac{r_{ij}^2}{4R_i R_j}\right)} \tag{3.18}$$

In this way the polarization charges induced by atom i interacting with the charge of atom j are modelled. In general, these charges screen the Coulomb interaction between two atoms, which is the main effect of the generalized Born approach.

As shown in Figure 3.3, there are three dielectric regions when considering interactions of peptides and surfaces in water solution, These are represented in the EISM model by the E_{SLIM} energy term. These three dielectric regions can be treated as two separated generalized Born terms. The electrostatic solvation free energy (ΔG_{elec}) is approximated with the E_{SLIM} energy term,

$$E_{\mathrm{SLIM}} = \Delta G_{\mathrm{elec}}^{\mathrm{SLIM}}(\varepsilon_{\mathrm{c}}, \varepsilon_{\mathrm{h}}, \varepsilon_{\mathrm{w}}) = \Delta G_{\mathrm{GB}}(\varepsilon_{\mathrm{c}}, \varepsilon_{\mathrm{h}}) + \Delta G_{\mathrm{GB}}(\varepsilon_{\mathrm{h}}, \varepsilon_{\mathrm{w}}) \approx \Delta G_{\mathrm{elec}}(\varepsilon_{\mathrm{c}}, \varepsilon_{\mathrm{h}}, \varepsilon_{\mathrm{w}}) \tag{3.19}$$

After decomposition, the first generalized Born term treats the peptide (ε_{c}) and the surface (ε_{h}), and the second term is devoted to the surface (ε_{h}) and water (ε_{w}). Using this methodology, we still can use the generalized Born approach, with two dielectric constants in each term. The dielectric constant of the peptide (ε_{c}) is assumed to be 1. The surface is modelled as a single dielectric slab, with dielectric constant (ε_{h}) which is equal to the bulk dielectric constant of the surface material. It is assumed have a finite thickness of z_{s}. The dielectric constant of water ε_{w} is equal to 80.

3.4.3 The Solvent Accessible Surface Area (SASA) term

The third term is the solvent accessible surface area (SASA) term, E_{SASA}. This term is essential in the formulation of the EISM model, as it empirically describes the interaction between the peptide and the surface. The term corresponds to the attractive and the repulsive interactions, except for the LJ interaction, between the amino-acid residues and the surface. The SASA is the surface given by the center of a ball (approximating a solvent molecule) rolling over a molecule, see Figure 3.7.

The interaction of the peptide and the surface is assumed to be proportional to the SASA of the peptide with a residue-specific surface tension, denoted as γ_i,

$$E_{\mathrm{SASA}} = \sum_i \gamma_i f(z_i - z_{\mathrm{s}}) A_i + \gamma_{\mathrm{w}} \sum_i A_i. \tag{3.20}$$

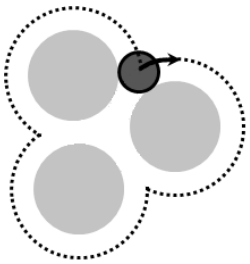

Figure 3.7: Schematic representation of the Solvent Accessible Surface Area, the dotted line denotes the SASA, the grey balls are atoms, and the graphite ball is the approximate molecule of the solvent, e.g. water.

Here, z_i is the distance of residue i from the surface, placed at position z_s, A_i is the SASA for the particular residue, γ_w is the standard surface tension of water used in the generalized Born surface area implicit solvent models.

The strength of this interaction varies with the distance of the i-th residue from the surface, and is damped by a polynomial function $f(z_i - z_\mathrm{s})$, which determines the range of interaction, see Figure 3.8. This range is defined by the value z_w, where the function varies smoothly by a polynomial from $f(0) = 1$ to $f(z_\mathrm{w}) = 0$, and is zero for all arguments larger than z_w . The gamma (γ_i) parameter is crucial, as it represents the affinity of the amino acid to a given surface. The values of γ_i have to be fitted to experimental or theoretical data, depending on the investigated surface and the experimental conditions (pH, temperature). In the next chapters, Chapters 4 and 5, such calibration against both theoretical and experimental reference data is introduced. The second term of Eq. 3.20 describes the nonpolar solvation free energy in water.

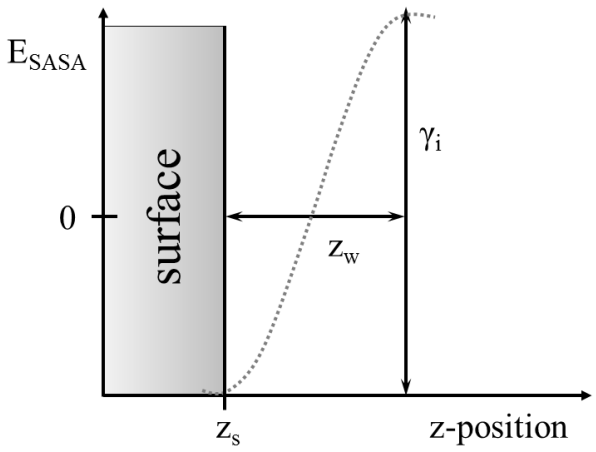

Figure 3.8: Surface SASA term as a function of the z-position of a single ion with charge $q = 1$, z_w denotes the range of the interaction between surface and peptide, and γ_i is a residue specific surface tension coefficient that describes the maximal binding affinity of that particular residue to the surface (obtained experimentally).

3.4.4 The surface Lennard-Jones term, E_{SLJ}

Furthermore, the Lennard-Jones interaction between the surface and the peptide is modeled by the surface Lennard-Jones term, E_{SLJ},

$$E_{\mathrm{SLJ}} = 8 \sum_i \sqrt{\epsilon_i \epsilon_{\mathrm{h}}} \left(\left(\frac{0.5(\sigma_i + \sigma_{\mathrm{s}})}{z_i - z_{\mathrm{s}} - \sigma_{\mathrm{s}}} \right)^{12} - \left(\frac{0.5(\sigma_i + \sigma_{\mathrm{s}})}{z_i - z_{\mathrm{s}} - \sigma_{\mathrm{s}}} \right)^{6} \right). \tag{3.21}$$

Here σ_i and ϵ_i are the Lennard-Jones parameters of an atom i in a peptide (see Figure 3.6 for LJ parameters), whereas σ_{s} and ϵ_{s} characterize the Lennard-Jones interactions for the surface. σ_{s} and ϵ_{h} are empirical parameters and account for the presence and position of different atom types in the surface, by making an average of their LJ parameters. The z_{s} parameter defines the position of the surface in z direction, and is equal to the dielectric slab boundary of the surface in the SLIM term. z_i is the distance of the peptide atom i from the surface. Note that E_{SLJ} is multiplied by 2 in contrast to the usual LJ equation (see Eq. 3.13). This term is mainly used to avoid peptides from entering the surface.

3.4.5 The pit potential, E_{PIT}

The last term, E_{PIT}, corresponds to the pit potential, which restricts the position of the center of mass for each peptide chain to a given cubic box around the origin, see Figure 3.3. If the center of mass is outside the bounding box, a penalty function, increasing quadratically with the distance from the cubic box, is applied.

The box is a cuboid defined by $x_{\min}$, $x_{\max}$, $y_{\min}$, $y_{\max}$, $z_{\min}$, and $z_{\max}$. The energy penalty is proportional to energy:

$$E_{\mathrm{PIT}} = s \sum_{\alpha=x,y,z} d_\alpha^2, \tag{3.22}$$

where d_α is the distance of the geometric center of the peptide from the center of the box in α-direction, and s is the user-defined steepness parameter, which determines how strong the peptide is pushed back into the box.

3.4.6 Limitations of the model

Due to its empirical nature, the EISM model has some limitations. Since the model assumes that the interaction between peptide and surface is proportional to the γ_i parameter of the E_{SASA} term (Eq. 3.20), all residues without this parameter do not interact with the surface. Moreover, all interactions between the surface and the peptide are short-ranged. However, a charged surface should also possess long-range interactions with the peptides. In addition, these long-range interactions should be proportional to the atomic partial charges and not the SASA term. Such long-range interactions could be treated with a Zeta potential, e.g., an exponentially decaying electrostatic potential. Since the presence of such a charged surface would also require ions to be present in the water, the GB term (Eq. 3.17) should also account for the presence of the ions to yield a consistent force field. Unfortunately, due to the charged surface, the ion concentration near the surface varies with the distance from the surface and the charge of the considered ions. A modified GB term that can handle such cases has not yet been developed.

4 Tests of the EISM model

In order to validate the EISM model, it was calibrated against theoretical reference data to reproduce the peptide binding affinities to gold (111) and silver (111) surfaces. Theoretically obtained binding affinities of single amino acids were used as a basis for the calibration. As there are available multiple sources containing required data, we picked two different sets of binding affinities for all amino acids to the gold (111) surface, and one set for the silver (111) surface.

4.1 Calibration of the EISM model

Before the EISM model could be applied for predicting and analyzing peptide surface interactions it has to be calibrated. This means that the γ_i parameters in Equation 3.20 should be proportional to theoretical or empirical data, providing binding affinities for all 20 amino acids to the chosen surface. For this purpose, literature values of the binding Gibbs free energy were used. From the available data I have chosen one that was well described and contained information about binding strength for all of the 20 amino acids [84,198]. Unfortunately, the values present in the literature are not consistent and the binding strength of a particular amino acid to a particular surface is often different, what also reveals in different global trends. This may be due to the high complexity of the process, which is in turn differently approximated in the literature methods. Therefore, I have independently calibrated the EISM model using amino acid data available in Refs. 84 and 198. First, the binding affinities reported by Hoefling et al. for gold (111) surface were used (Chapter 4.2.1) [84]. Second, ones reported by Palafox-Hernandez et al. [198], for two surfaces: gold (111) (Chapter 4.2.2) and silver (111) (Chapter 4.3). Using the model calibrated with respect to two different training sets I have performed simulations for test peptides. The results were then compared to experimental and calculated literature values.

4.1.1 Inconsistency of the reference data

The Gibbs free energy of the amino acid binding affinity from Hoefling et al. and Palafox-Hernandez et al. are compared on the plot in Figure 4.1. The data shown in the plot were scaled, in a way to multiply the Hoefling scores by factor 0.6, to make the two sets directly comparable. One can notice that not only the values are different, but also the binding trends. At first sight it is clear that the values reported by Palafox-Hernandez, for all amino acids, are much more scattered, and binding of tyrosine (Y), tryptophan (W), cysteine (C) and arginine (R) is clearly the strongest. The important difference is also that lysine (K) in theirs study manifests as a weak binder, what is surprising, because it is an electrically charged amino acid, and such are known to be strong binders [112].

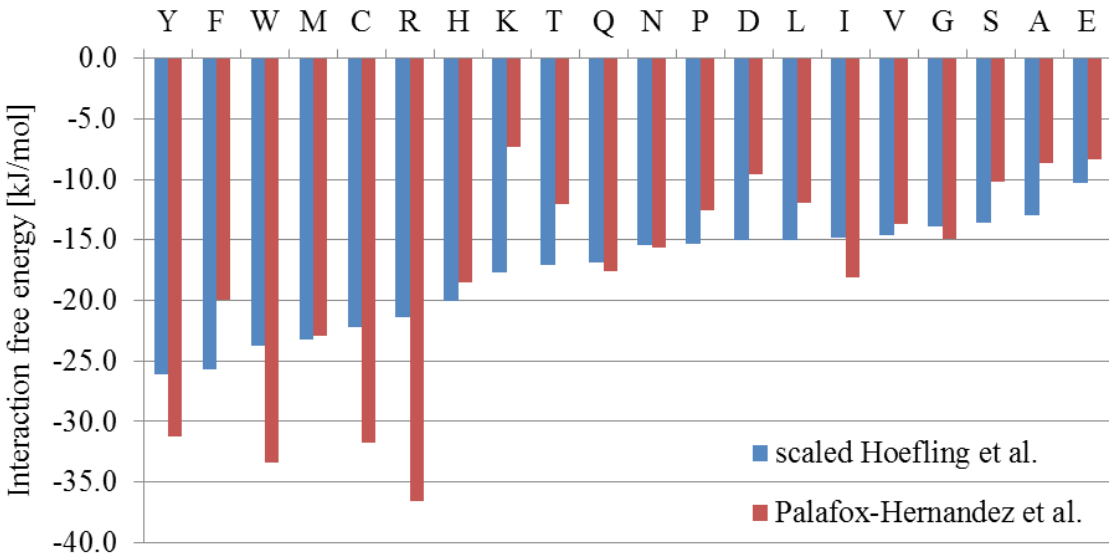

Figure 4.1: Comparison of the amino-acid binding affinity to the gold (111) surface as reported by Hoefling et al. (multiplied by 0.6), and Palafox-Hernandez et al.

4.2 Gold-binding peptides

4.2.1 The first calibration set

First, the EISM model was calibrated using the data provided by Hoefling et al., obtained by use of molecular dynamics (MD) simulations[84]. The EISM binding affinities of all 20 amino acids (γ_i), cf. Eq. 3.20, have been calculated in a way to be proportional to the reference values of free energies of binding and collected in Table 4.1. In order to verify what values of γ_i are correct, to reproduce the desired values of the binding affinities for single amino acids, we have calculated free energy profiles with different values of the parameters in the range between -0.08 and -0.01. An example free energy curve for glutamic acid is given in Figure 4.2

If we then check how the free energy of binding of a single amino acid depends on the value of γ_i, we can find a linear dependence, see example for glutamic acid (GLU) in Figure 4.3. In this way we can correlate the reference free energy of binding for all amino acids with corresponding binding affinity coefficients (γ_i) to parametrize the EISM model for data obtained in particular conditions.

In order to assess the quality of this calibration, five peptides were taken into account, and their calculated binding affinities were compared with work of Heinz et al.[200] Two of them: AYSSGAPPMPPF (A3), DYKDDDDK (Flg) are found to be very good gold (111) binders[22,25] and the remaining three of them: DYKDDDK (Flgd), GGGGGGGGGG (G10), PPPPPPPPPP (P10) are presenting various affinity. The binding free energy profile of the considered peptides to the gold (111) surface calculated with the EISM model is presented in Figure 4.4. The region of binding lies around 4 Å above the surface, and the region above this distance represents the unbound state. The binding strength is defined as an energy difference between the unbound and bound state.

In the presented results, the A3 peptide is the best binder, the Flg peptide is the second best binding peptide. These two peptides have mostly electrically-charged amino acids

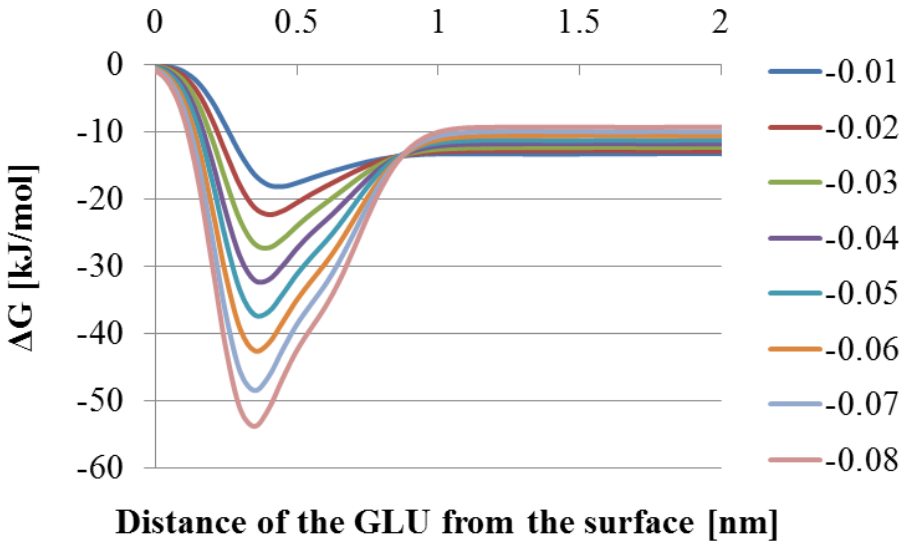

Figure 4.2: Free energy profiles of GLU obtained with different values of the γ_i coefficient, made by Dr. Priya Anand (KIT).

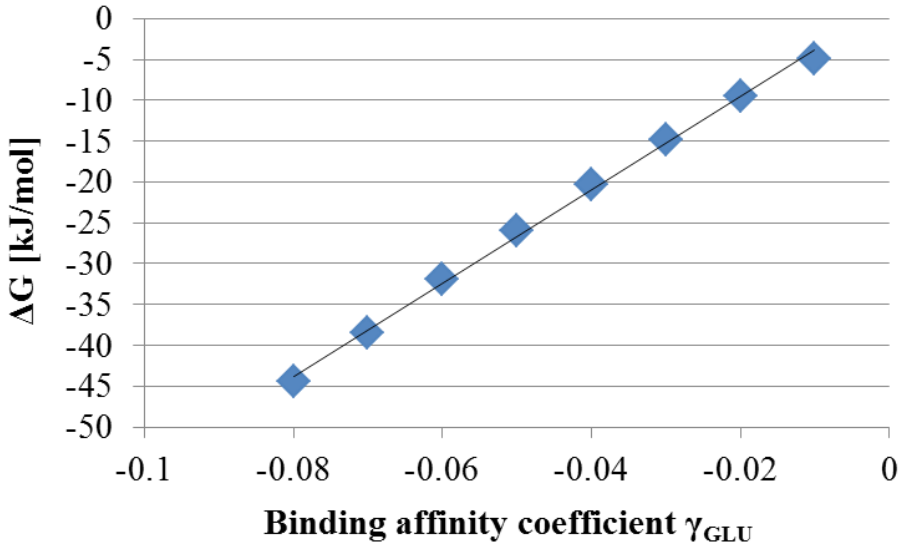

Figure 4.3: Dependence of the free energy of binding for GLU on the value of the γ_i coefficient, made by Dr. Priya Anand (KIT).

Amino acid	3-letter code[199]	1-letter code[199]	Ref. ΔG [kJ mol^{-1}]	EISM γ_i	EISM γ_i [kJ mol^{-1}]
Alanine	Ala	A	-21.9	-0.0438	-21.9
Arginine	Arg	R	-36.3	-0.0726	-36.3
Asparagine	Asn	N	-26.1	-0.0522	-26.1
Aspartic acid	Asp	D	-25.5	-0.0510	-25.5
Cysteine	Cys	C	-37.7	-0.0754	-37.7
Glutamic acid	Glu	E	-17.5	-0.0350	-17.5
Glutamine	Gln	Q	-28.6	-0.0572	-28.6
Glycine	Gly	G	-23.6	-0.0472	-23.6
Histidine	His	H	-34.0	-0.0680	-34.0
Isoleucine	Ile	I	-25.1	-0.0502	-25.1
Leucine	Leu	L	-25.4	-0.0508	-25.4
Lysine	Lys	K	-30.0	-0.0600	-30.0
Methionine	Met	M	-39.3	-0.0786	-39.3
Phenylalanine	Phe	F	-43.6	-0.0872	-43.6
Proline	Pro	P	-26.0	-0.0520	-26.0
Serine	Ser	S	-23.1	-0.0462	-23.1
Threonine	Thr	T	-28.9	-0.0578	-28.9
Tryptophan	Trp	W	-40.2	-0.0804	-40.2
Tyrosine	Tyr	Y	-44.2	-0.0884	-44.2
Valine	Val	V	-24.8	-0.0496	-24.8

Table 4.1: γ_i parameters used in the EISM model adapted from Ref. 84.

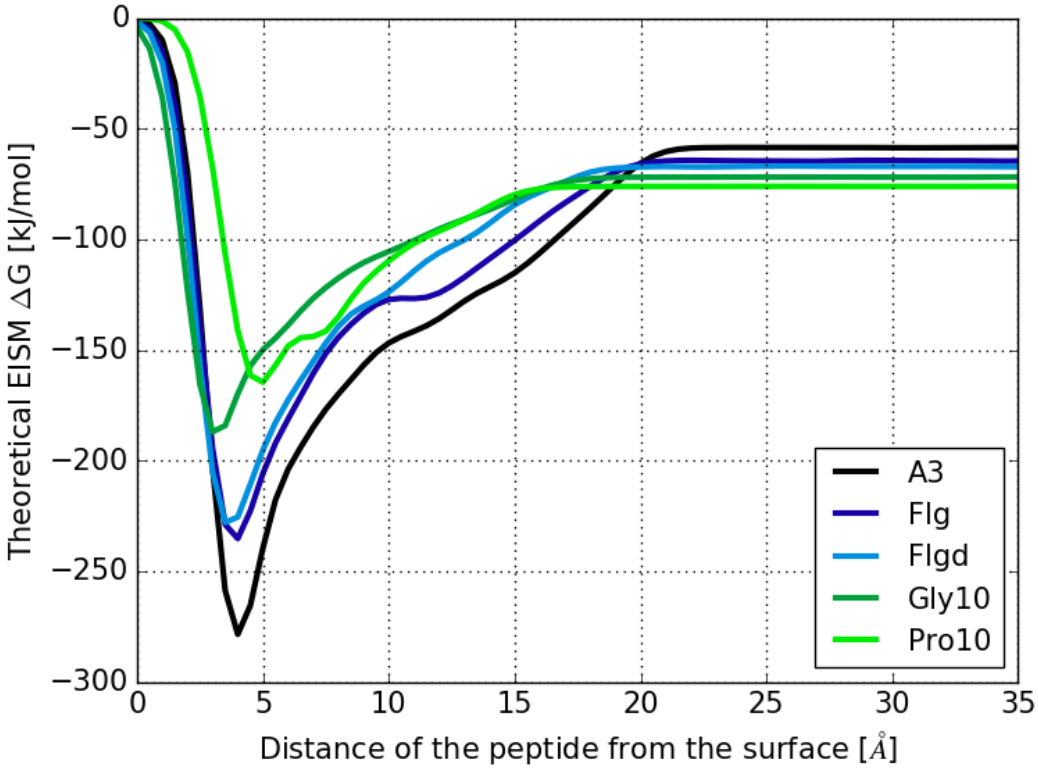

Figure 4.4: Binding free energy profiles obtained with the EISM method calibrated against data from Ref. 84.

in their sequences (D, K), what makes them good binders to a metallic surface. Flgd is the third, however, there is almost no difference in binding comparing to the Flg. The unexpected almost equal binding of the Flg and Flgd peptides may be explained by their similar geometrical flexibility which exposes the side chains important for binding. Gly10 and Pro10 peptides are the worst binding peptides, which is also consistent with the expectations. This can be explained by the properties of glycine and proline, which are small amino acids with nonpolar side chains, with limited possibility of binding.

Next, these results were scaled by multiplying them by factor of 1.4, to be in the same range of values, and compared with findings of Heinz et al.[200], see Figure 4.5. The reference results were obtained with molecular dynamics simulations, using an efficient computational screening technique, including 1000 explicit water molecules and physically meaningful peptide concentrations at pH = 7.

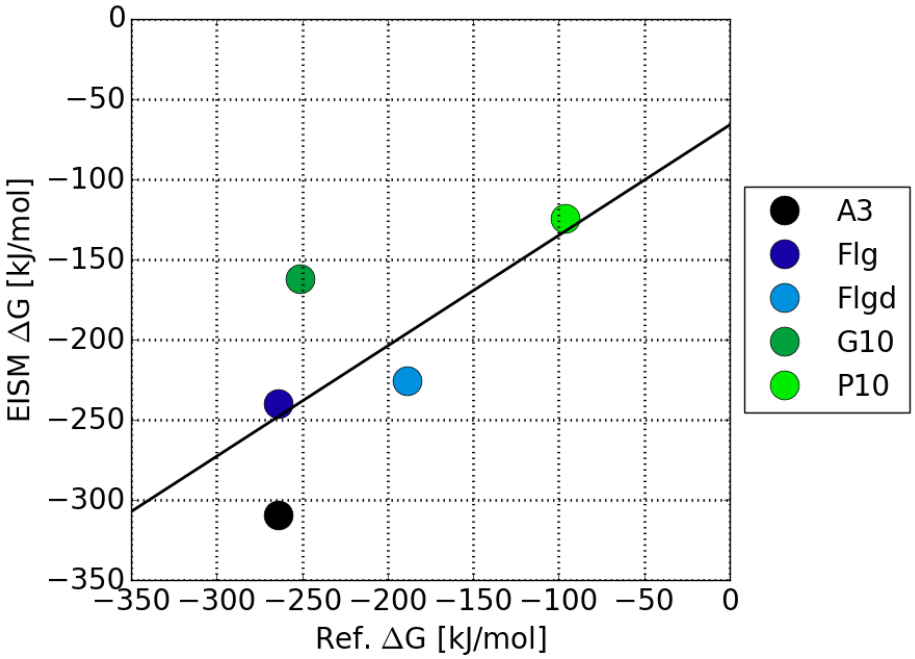

Figure 4.5: Comparison of the EISM binding and the theoretical reference data from Ref. 200. Linear fit: $f(x) = 0.69x - 66.24$.

In this comparison one can see that the EISM results are not always consistent with the reference. In both cases gold bonding peptides (A3, Flg) are the strongest binders, even though they have not exactly the same energy of binding. What is somewhat surprising in the reference paper is that the binding of the Gly10 peptide, which is built of weak binding amino acids, to the gold (111) surface is stronger than the binding of the Flgd peptide. This may be due to the fact that 10 subsequent glycines form a very flexible chain and its behavior might be very difficult to predict.

All in all, the accuracy of the EISM is difficult to judge, it can predict a certain trend of binding for the set of peptides, which sequence will bind better, and which worse, but due to its empirical nature exact binding energies are out of the reach.

4.2.2 The second calibration set

In the next calibration another reference data set was used. Now the binding affinities were adapted from the free energies of binding of all 20 amino acids provided by Palafox-Hernandez et al.[198], who used well-tempered metadynamics MD simulations, see Table 4.2. The procedure of parametrization of the EISM γ_i was the same as in the previous chapter. The experimental reference for peptides was reported by Tang and co-workers[201], where the affinity of the peptides and gold (111) surface was investigated by means of Quartz Crystal Microbalance (QCM) measurements.

Amino acid	3-letter code[199]	1-letter code[199]	Ref. ΔG [kJ mol^{-1}]	EISM γ_i	EISM γ_i [kJ mol^{-1}]
Alanine	Ala	A	-8.6	-0.0182	-8.6
Arginine	Arg	R	-36.6	-0.0773	-36.6
Asparagine	Asn	N	-15.7	-0.0331	-15.7
Aspartic acid	Asp	D	-9.6	-0.0202	-9.6
Cysteine	Cys	C	-31.7	-0.0670	-31.7
Glutamic acid	Glu	E	-8.4	-0.0177	-8.4
Glutamine	Gln	Q	-17.5	-0.0371	-17.5
Glycine	Gly	G	-15.0	-0.0316	-15.0
Histidine	His	H	-18.5	-0.0390	-18.5
Isoleucine	Ile	I	-18.1	-0.0382	-18.1
Leucine	Leu	L	-11.9	-0.0252	-11.9
Lysine	Lys	K	-7.4	-0.0156	-7.4
Methionine	Met	M	-22.9	-0.0484	-22.9
Phenylalanine	Phe	F	-20.0	-0.0422	-20.0
Proline	Pro	P	-12.5	-0.0265	-12.5
Serine	Ser	S	-10.2	-0.0216	-10.2
Threonine	Thr	T	-12.1	-0.0255	-12.1
Tryptophan	Trp	W	-33.4	-0.0706	-33.4
Tyrosine	Tyr	Y	-31.3	-0.0661	-31.3
Valine	Val	V	-13.6	-0.0288	-13.6

Table 4.2: γ_i parameters used in the EISM model adapted from Ref. 198.

In order to validate the calibration of the EISM model against the new reference set, another group of peptides was considered. In Table 4.3, the peptide sequences along with their experimentally obtained (QCM) surface affinities are given. The binding affinities obtained with the EISM model were rescaled, in a way to multiple them by factor of 0.2, to place them in the same range of values, and are compared in Figure 4.6.

The fit of the EISM data to the QCM results is showing a good trend, especially if we take into account the fact that there is a standard deviation in the experiment ± (0.1–1.2 kJ mol^{-1}). The best agreement is achieved for peptides AuBP1, AgBP2, QBP1, Z1, Z2, Pd4, AgBP1 and A3. A worse agreement is observed for peptides Midas2, B1 and GBP1, and the worst result, with a rather bad prediction is obtained for the AuBP2 peptide. That suggests that the binding affinities of some of the amino acids used in the calculations are overestimated or underestimated.

Peptide	Seqence	Exp. ΔG [kJ mol^{-1}]
AuBP1	WAGAKRLVLRRE	-37.6 ± 0.9
GBP1	MHGKTQATSGTIQS	-37.6 ± 1.0
B1	LKAHLPPSRLPS	-36.6 ± 1.2
AuBP2	WALRRSIRRQSY	-36.4 ± 0.3
Midas2	TGTSVLIATPYV	-35.7 ± 1.2
AgBP2	EQLGVRKELRGV	-35.3 ± 1.2
Z2	RMRMKMK	-35.0 ± 0.6
QBP1	PPPWLPYMPPWS	-35.0 ± 1.1
A3	AYSSGAPPMPPF	-31.8 ± 0.3
AgBP1	TGIFKSARAMRN	-31.6 ± 0.2
Z1	KHKHWHW	-31.3 ± 0.1
Pd4	TSNAVHPTLRHL	-30.3 ± 0.2

Table 4.3: Reference peptides, and their binding affinities to the gold (111) surface, used to validate the calibration of the EISM model.

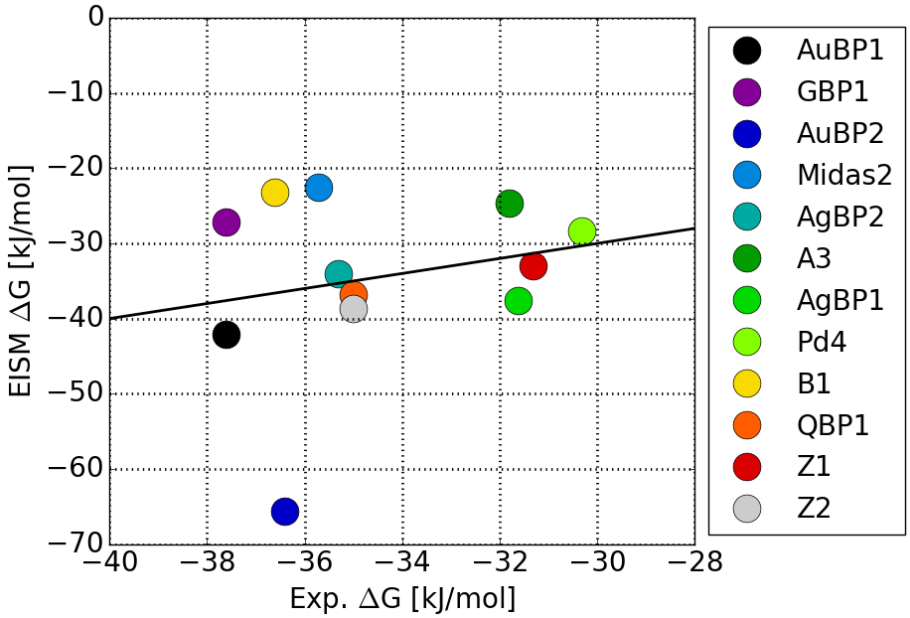

Figure 4.6: Comparison of the binding affinities obtained with the EISM model calibrated against data from Ref. 198 and the experimental reference data of Ref. 201. Linear fit: $f(x) = 1.00x - 0.04$.

4.2.3 Optimization of the EISM parameters

In order to reduce the discrepancy between the EISM-simulated and experimentally-obtained binding affinity an optimization procedure can be introduced. The way of proceeding is to analyze the composition of chosen peptides. Subsequently, check how a manipulation of the binding strength factor (γ_i) for the amino acids with the highest occurrence in the 'failing' sequences will influence the binding of the peptides compared to the experiment. Such an optimization was carried out by Florian Gußmann (KIT). His optimized amino-acid affinities were used in subsequent EISM simulations. Comparison of the binding affinities before and after optimization is included in Figure 4.9. Therein obtained binding affinities, with new optimized γ_i, for the group of peptides considered in the Chapter 4.2.2 are compared to the experimental ones in Figure 4.7.

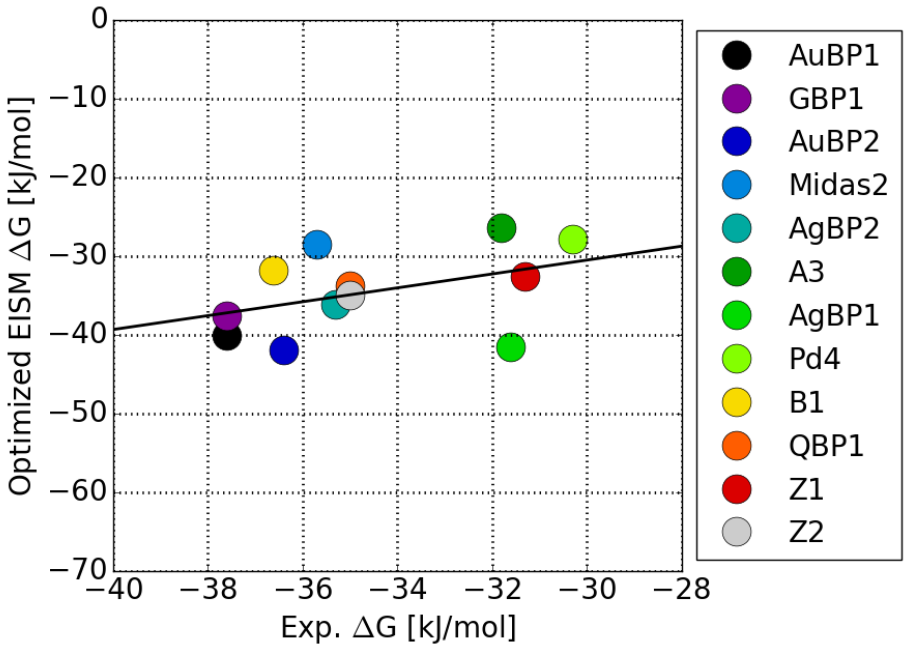

Figure 4.7: Comparison of the binding affinities obtained with the EISM model using optimized amino-acid affinities and the reference experimental data of Ref. 201. Linear fit: $f(x) = 0.89x - 3.95$.

We can clearly see that after the optimization the agreement of the simulated and the experimental ΔG is better. An especially visible change is observed for the AuBP2 (navy blue dot) which was an outlier in the previous comparison. Now, it is in the group of the well-reproduced peptides. The improvement is also noticeable for peptides GBP1, B1, and Midas2, which were quite far from the trend, and now they represent a good agreement.

In Figure 4.8 an analysis of the sequences of the peptides with the highest ΔG improvement is presented, and in Figure 4.9 the binding affinities of all amino acids (γ_i) to the gold (111) surface, before and after the optimization.

According to Figure 4.8, arginine (R) is an important component of the AuBP2, it represents in around 33% of all residues in the structure. Its binding affinity (γ_i parameter) was reduced for about a half upon the optimization (see Figure 4.9). This was the most important contribution to the reduction of the ΔG for AuBP2. Initially, GBP1, B1 and

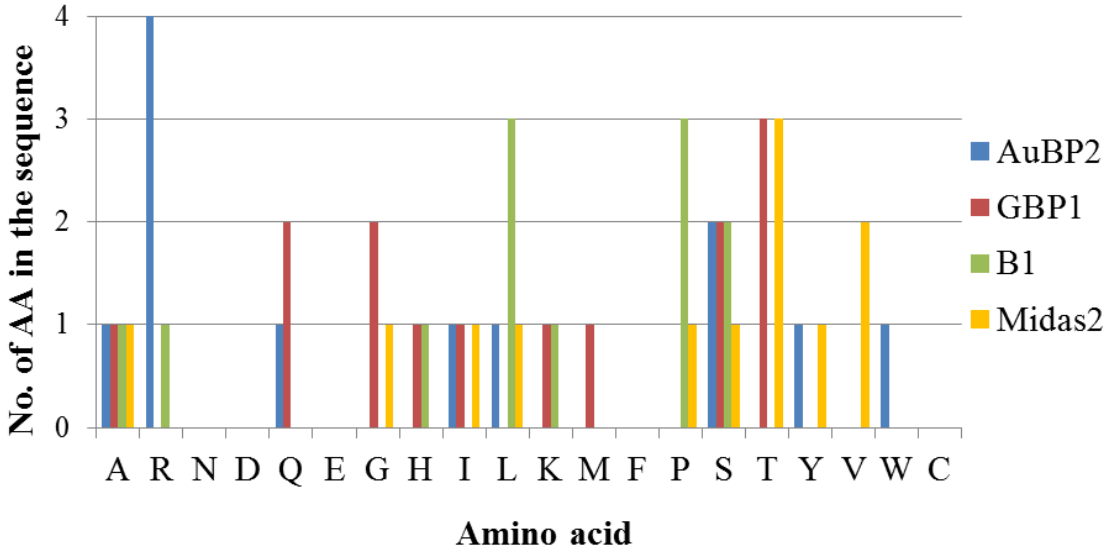

Figure 4.8: Amino-acid composition of the selected peptides used in the optimization procedure.

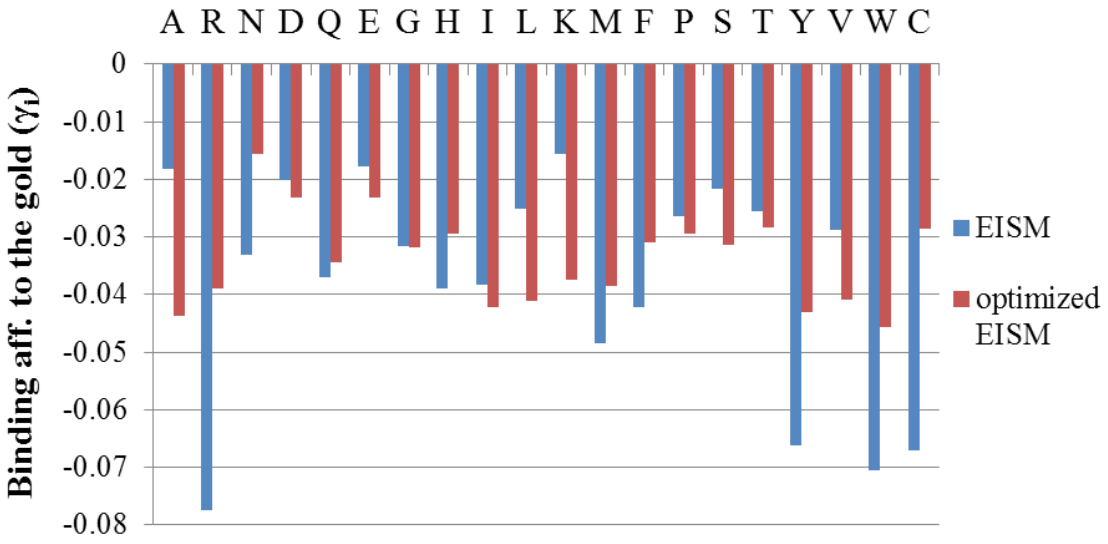

Figure 4.9: Amino-acid binding affinities (γ_i parameters) before and after the optimization.

Midas2 peptides were predicted by the EISM to be worse binders compared to experiment. The optimization of the amino-acid binding affinities strengthened some of them. As a consequence, alanine (A), leucine (L) and lysine (K) became better binders for about 40—60%; serine (S) and valine (V) were also better at about 30%; proline (P) and threonine (T) slightly better as well. All these changes affected the binding of mentioned peptides to have slightly higher absolute ΔG and therefore fit better to the experimental results.

The optimization procedure was carried out for all 20 amino acids for a chosen set of peptides. It is noteworthy that B1, QBP1, Z1 and Z2 peptides were not included in the refinement procedure. Despite that their free energies of binding are also improved when the optimized set of amino-acid binding factors is used. This fact is promising for other peptide sequences which were not investigated here, since a suitably chosen training set could yield universal optimized amino-acid binding affinities (γ_i).

4.3 Silver-binding peptides

Up to this point interactions of peptides with gold (111) were investigated. In the next step, another metal surface, namely silver, was considered. There is an interesting fact that so-called gold-binding peptides are also in the group of silver-binding peptides. The reason for that is that in terms of chemical properties gold and silver surfaces are almost identical. Hence, it is a challenge to find silver-specific binding peptides. A set of peptides: AuBP1, AuBP2, AgBP1, AgBP2 was investigated by Palafox-Hernandez et al.[198] in order to find silver-specific binders. They experimentally found that only AgBP1 was a selective silver-binder (better binding to silver than to the gold surface), while the remaining peptides have strong and comparable affinities for both surfaces. I have performed EISM simulations to find out whether these results can be reproduced by the EISM method. In order to parametrize the EISM model for the new surface (the new γ_i), the new set of binding free energies for all 20 amino acids to the silver (111) surface provided in Ref.2 198 is used. See Chapter 4.2.1 for details of the parametrization procedure.

In Figure 4.10 the binding Gibbs free energies of the selected peptides to the silver (111) surface obtained by means of EISM model, and scaled by factor of 0.5, are compared with the reference experimental QCM data[198]. For all peptides a good agreement is observed, especially if we take into account the experimental standard deviation in a range of 0.8 and 1.0 kJ mol^{-1}, which makes experimentally obtained ΔGs almost indistinguishable.

Finally, the binding properties of silver and gold surfaces are compared. The comparison of the free energies of binding of the same peptides (AuBP1, AuBP2, AgBP1, AgBP2) and two different surfaces, namely, silver (111) and gold (111), is plotted in Figure 4.11. All the peptides are binding well to both surfaces and all of them are binding better to the gold (111) surface, except for the AgBP1 peptide which might be called a silver-specific binder. However the difference is not very distinct. In general, the EISM results are consistent with the reference paper[198].

4.4 Summary

To summarize, the EISM model was calibrated against three sets of computed amino acid specific binding affinity (γ_i), two different sets for gold and one set for silver surface. It is shown that the EISM model can reproduce both simulated and experimentally obtained

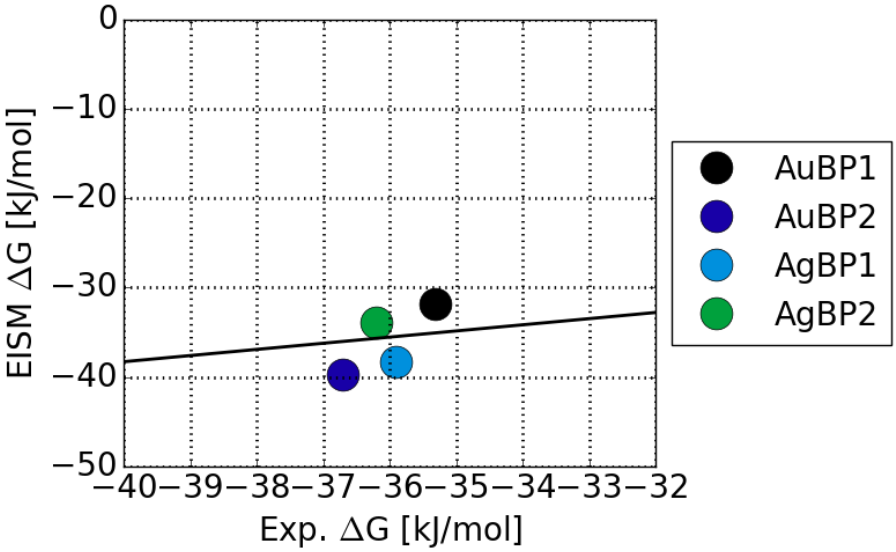

Figure 4.10: Comparison of the theoretical (EISM) and experimental (Ref. 198) binding affinities to the silver (111) surface. Linear fit: $f(x) = 4.75x + 135.12$.

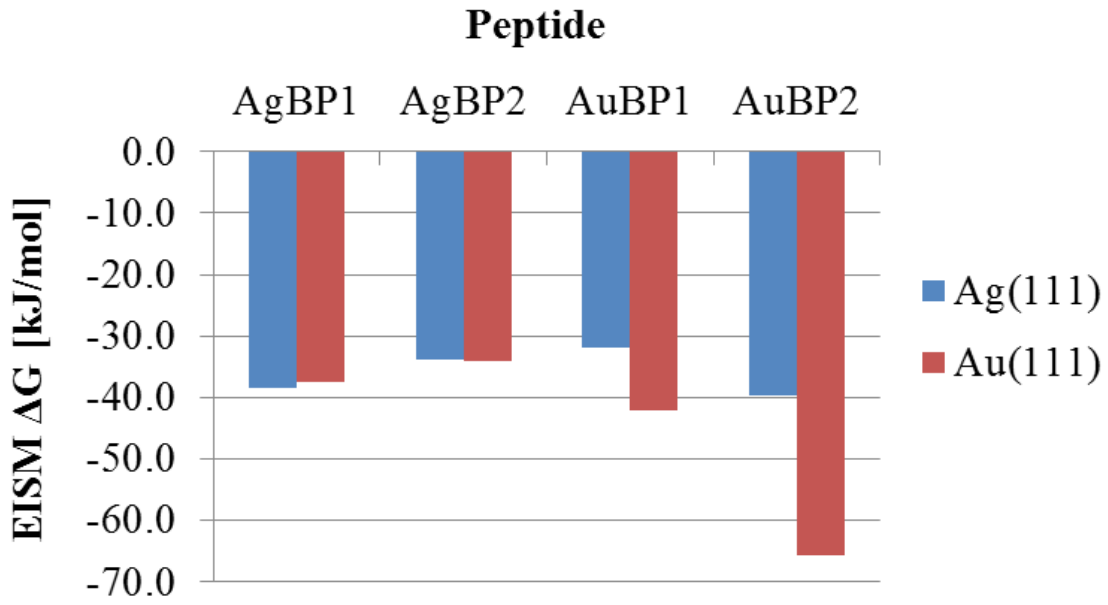

Figure 4.11: Comparison of the EISM binding affinities of the peptides to the silver (111) and gold (111) surfaces.

binding affinities for entire peptides with a good accuracy. Some single discrepancies can be overcome by a careful analysis of the sequences of the failing peptides, and reoptimization of the binding affinity for the most contributing amino acids. The presented method can be efficiently used to compare binding to silver and gold surfaces, and thus provide surface-specific binders. To perform simulations for the new surface and environment with EISM model, new set of binding affinities for all amino acids is required. Knowing the composition of the amino acids included in the peptide sequence, the binding free energy for the whole peptide can be calculated.

5 Interactions of peptides with magentic nanoparticles (MNPs)

As a result of the experimental procedure of peptide array screening, see Chapter 2.3.1 for description, one can obtain relative binding affinities for chosen peptide sequences, placed on the membrane, to the nanoparticles present in the buffer solution. Two different membranes were designed, containing sets of peptides which are in particular suitable for a systematic analysis of peptide binding to iron oxide magnetic nanoparticles (MNPs). The first membrane, containing homopeptides, see Figure 2.12, was mainly used to propose theoretical description and model of binding between the charged amino acids and the surface in different buffers, see Chapter 5.1. It was used also to parametrize the EISM model for the interactions of peptides with MNPs in Tris buffer solution and pH 7.4, see Chapter 5.2. The second membrane, presented in Figure 5.14, containing different peptide sequences, mostly D-peptides mutated with other amino acids, was used as a reference for calculated binding free energies of peptides with EISM model. This comparison is also in Chapter 5.2.

5.1 Experimental conditions and observations

The peptide array experiment, for the membrane with homopeptides, was carried out in three different buffers, Tris(hydroxymethyl)aminomethane [Tris], phosphate buffer [T-PBS], and citric acid buffer at three different pH values, 6.0, 7.4, 8.0. The experimental conditions are summarized in Table 5.1.

pH	Buffer set 1	Buffer set 2
6.0	T-PBS	Citric Acid
7.4	T-PBS	Tris
8.0	T-PBS	Tris

Table 5.1: Experimental conditions, pH values and respective buffers, for the peptide array screening procedure.

Out of many peptides present on the membrane, only the strongest-binding peptides were selected for further analysis, the two positively and two negatively charged homopeptides, respectively RRRRRR(+), KKKKKK(+) and EEEEEE(-), DDDDDD(-). For these peptides experimentally obtained binding affinities to the MNPs, in two different buffer sets, can be found in Figures 5.1 and 5.2.

In Figure 5.1, the results obtained for the first buffer set are shown. The binding occurs only for positively charged peptides. In Figure 5.2, in turn, all peptides bind. It is worth to underscore that positively charged peptides in citric acid buffer are binding almost three

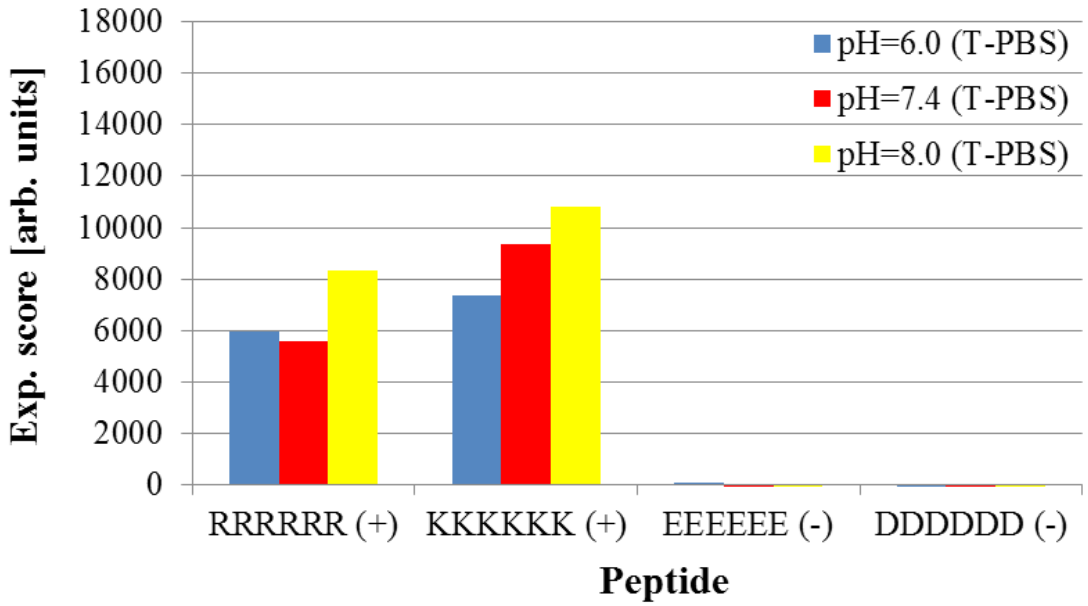

Figure 5.1: Experimentally obtained binding affinities for charged peptides in phosphate buffer (T-PBS) and three different pH values.

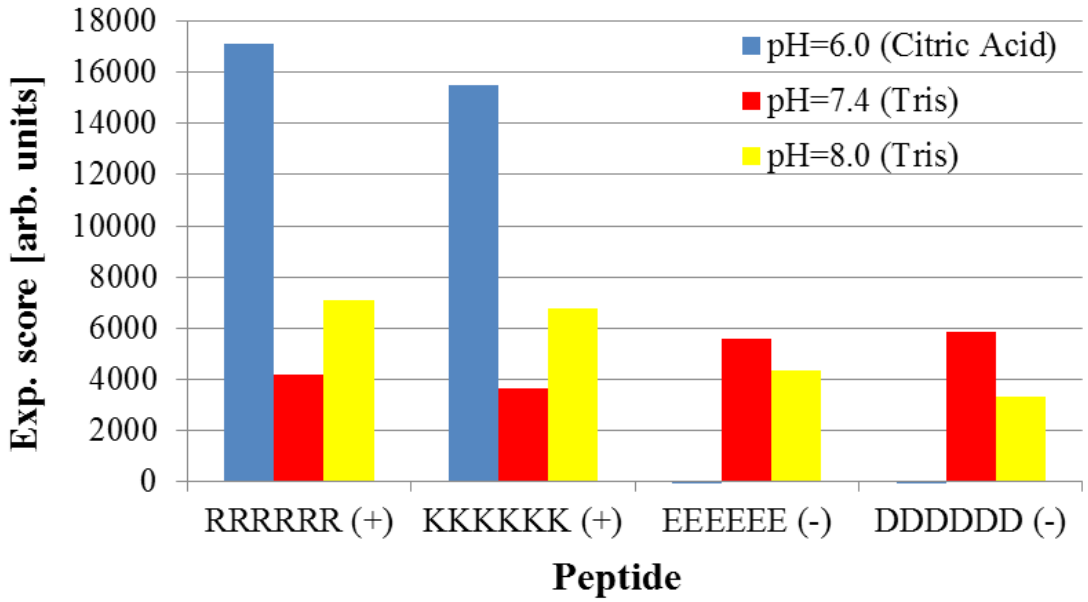

Figure 5.2: Experimentally obtained binding affinities for charged peptides in citric acid buffer at pH=6.0, and Tris buffer at pH=7.4, and 8.0.

times stronger than in Tris buffer. In order to understand the observations, a theoretical model was developed, which can explain processes occurring in the considered inhomogeneous systems. The method is based on the occurrence of the equilibrium reactions in the solution. As a result of the analysis it is possible to predict the binding strength of the charged amino acids to the MNPs in a certain buffer, both qualitatively and, to some extent, quantitatively. In the following section the procedure is introduced.

5.1.1 Foundations of the model

To predict how strong the interaction of the charged amino acids to the MNPs will be, it is necessarily to know the percentage and types of ions present in the solution of the mixture AA/buffer/surface. The next step is to define possible reactions and calculate the amounts of products.

First, one has to check the concentration of each reagent in the mixture. In the analyzed case, the concentration of the buffer is at least an order of magnitude larger than the concentration of the magnetic nanoparticles, and even seven orders of magnitude larger than the concentration of the peptide. This means that the concentration of the final product, after all occurring reactions, would be limited by the concentration of the peptide, i.e. the lowest value. At the same time, all the reactions are dominated by the activity of the buffer ions, which are dominating in the solution. Note that the reaction equilibrium of the dissociation of the buffer will not be perturbed during the process, since it is present in excess.

The pH of the solution is an important parameter. This determines the ratio of the respective ionic species of the buffer systems. For instance, for the phosphoric acid, feasible to dissociate three protons, there are three equilibrium reactions, as shown in Table 5.2.

Equilibrium	Equilibrium general	pK_a value
$H_3PO_4 + H_2O \rightleftarrows H_2PO_4^- + H_3O^+$	$HB + H_2O \rightleftarrows B^- + H_3O^+$	$pK_{a,1} = 2.14$
$H_2PO_4^- + H_2O \rightleftarrows HPO_4^{2-} + H_3O^+$	$B^- + H_2O \rightleftarrows B^{2-} + H_3O^+$	$pK_{a,2} = 7.20$
$HPO_4^{2-} + H_2O \rightleftarrows PO_4^{3-} + H_3O^+$	$B^{2-} + H_2O \rightleftarrows B^{3-} + H_3O^+$	$pK_{a,3} = 12.37$

Table 5.2: Dissociation reactions of the phosphoric acid.

In a certain pH, the ratio of the ionic species of the particular compound is constant and it can be provided by the equilibrium reactions. The most preferred equilibrium reaction, taking place in the solution, is the one which pK_a is the closest to the pH of the solution, e.g., for the phosphoric acid, in pH=7.4, the most pronounced reaction is

$$H_2PO_4^- + H_2O \rightleftarrows HPO_4^{2-} + H_3O^+. \tag{5.1}$$

Thus, in the solution there are mainly two types of buffer species present: $H_2PO_4^-$ and HPO_4^{2-}. To calculate the exact amount of each of the species, the concentration of phosphoric acid has to be known. The sum of molar concentrations of all buffer species is equal to the molar concentration of phosphoric acid. Using the equation,

$$pH = pK_a + \log_{10} \frac{[B^-]}{[HB]}, \tag{5.2}$$

the molar fraction of species $[B^-]/[HB]$ is obtained. There is also another way to get those values, using speciation plots available in literature[202], for certain compound and read the values in selected pH, see Figure 5.3 for such a plot for the phosphoric acid example.

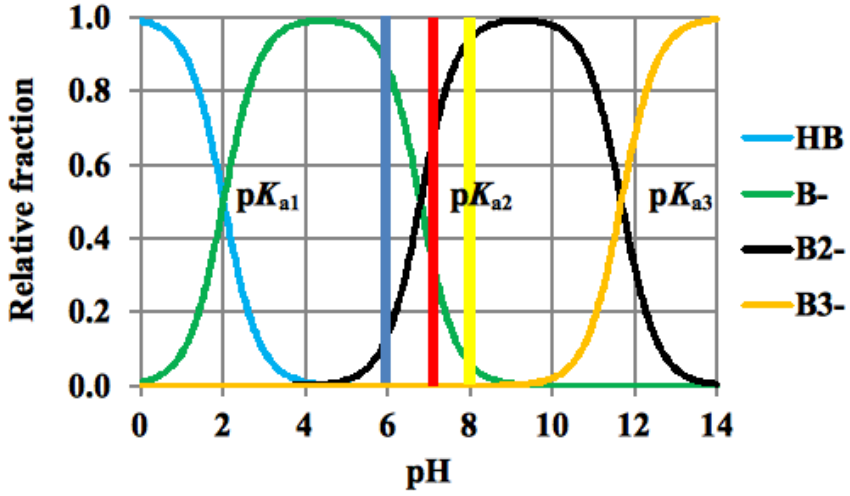

Figure 5.3: Relative fractions of all phosphoric acid species in the function of pH.

In the plot in Figure 5.3, three different pH values were marked (6.0 — blue line, 7.4 — red line, 8.0 — yellow line), corresponding to experimental conditions in the analyzed case. Here and in the following, the specific color code is used to denote the pH conditions. Now, the differences in the composition of the buffer in different pH conditions become visible, see Figure 5.4.

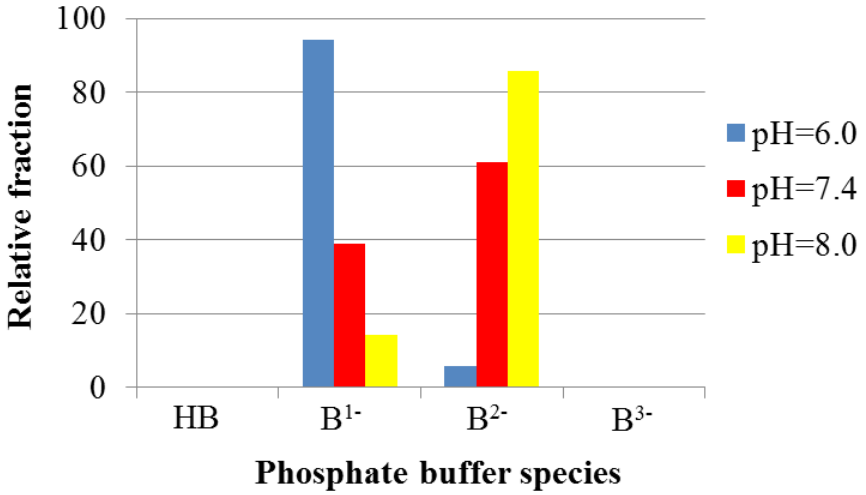

Figure 5.4: Phosphate buffer species at pH 6.0, 7.4, and 8.0.

In the considered example, one can observe that the higher pH is, the more species with charge '2–' over species with charge '1–' occur in the solution. For the citric-acid buffer, which has more species with higher charge already in pH = 6.0, see Figure 5.5, there is dominating amount of '2–' species, but also a non-negligible amount of the '3–' species.

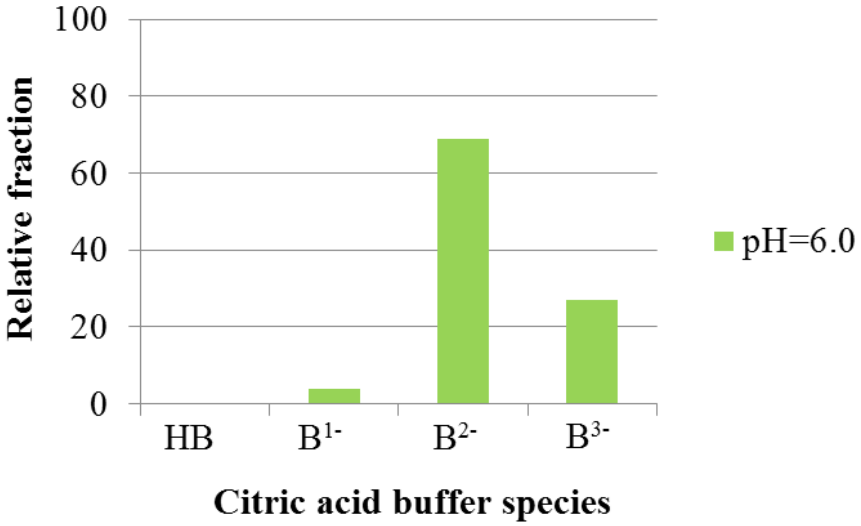

Figure 5.5: Citric buffer species at pH 6.0.

These observations can now be compared to the experimental results. The binding affinity of charged homopeptides (RRRRRR and KKKKKK) to the magnetic nanoparticles in the above-presented buffers is shown in Figure 5.6.

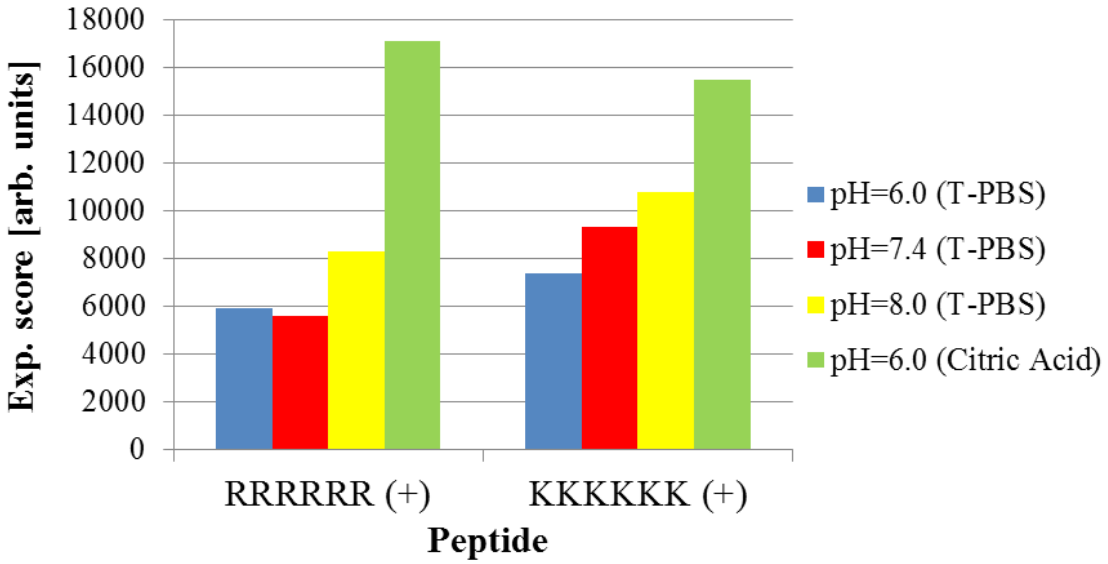

Figure 5.6: Experimental binding affinities of positively-charged peptides in phosphate buffer at pH 6.0, 7.4, and 8.0, and citric acid buffer at pH 6.0.

Now, a clear relation between the speciation plots for the buffers and binding between the MNPs and the peptides can be noticed. The more species with higher charges in the solution the stronger binding for the oppositely charged peptides is observed. This observation leads to a general assumption which is the basis of the presented model, that the binding between peptides and MNPs is mediated by the buffer. Note that all charged buffer species, not only those with the highest charges, contribute to the binding, because

the ratio of the buffer species in a certain pH needs to be constant and a small amount of peptide is not enough to perturb this equilibrium.

From other experimental observations, namely potentiometric acid–base titrations[111], it can be found that the magnetic nanoparticles are slightly charged, and apart from sign of the total charge, they bind to the charged buffer species. In this model, positively and negatively charged areas on the surface of the nanoparticles are considered. The sum of these area-charges results in the total charge which in turn depends on the pH of the solution. An overall positive charge of the MNPs was observed below pH 7.8, and a negative charge above pH 7.8. The ratio of the products of the binding reactions is proportional to the ratio of the corresponding buffer species, due to the high concentration of the buffer.

Among many peptides present on the membrane, we have chosen the ones which contain six amino acids of the same type. These are used as test cases to explain the method. Moreover, for simplicity, the entire peptide is treated as a single amino acid (AA), what does not change the result.

All buffer species, namely positively charged (B^+), neutral (B^0), and negatively charged (B^-), analogously defined peptide species, i.e., (AA), as well as nanoparticles (NP) are the substrates. The NPs are additionally able to bind to all kinds of charged species. Nevertheless, already at the early stage, based on the experimental observations, some of the combinations are excluded. It can be noticed, in Figure 2.12, that reactions between charged and neutral species do not occur, or are below the noise level, e.g.,

$$\mathrm{NPB}^{+/-} + \mathrm{AA}^0 \rightleftarrows \text{no reaction.} \tag{5.3}$$

Where NPB denotes a nanoparticle covered with buffer species. In the presented model such an observation is explained by the lack of the possibility of the electrostatic interaction between a neutral AA and a charged NPB.

In the following part only the reactions of nanoparticles and amino acids possibly occurring in the solution are considered. For each of them, their influence on he observed total binding is briefly discussed.

5.1.2 Reactions of oppositely charged species

In the experiments, the nanoparticles are first solved in the buffer solution, and afterwards this mixture is applied on the peptide array. Therefore, two steps are considered.

In the first step the charged buffer species are binding to the respective positive and negative spots of the nanoparticles:

$$\mathrm{NP} + \mathrm{B}^{\mathrm{n}+} \rightleftarrows \mathrm{NPB}^{\mathrm{n}+} \quad \text{or} \quad \mathrm{NP} + \mathrm{B}^{\mathrm{n}-} \rightleftarrows \mathrm{NPB}^{\mathrm{n}-}. \tag{5.4}$$

In the second step the nanoparticles coated with buffer are reacting with the peptides:

$$\mathrm{NPB}^{\mathrm{n}+} + \mathrm{AA}^{\mathrm{m}-} \rightleftarrows \mathrm{NPBAA}^{\mathrm{n}-\mathrm{m}} \quad \text{or} \quad \mathrm{NPB}^{\mathrm{n}-} + \mathrm{AA}^{\mathrm{m}+} \rightleftarrows \mathrm{NPBAA}^{\mathrm{m}-\mathrm{n}}. \tag{5.5}$$

This step is more complex, and many factors have to be considered at the same time.

Considering the reactions given above, the binding strength, and therefore ΔG, directly depends on the values of the charges. According to Coulomb's law, the electrostatic force is proportional to the product of charges ($\mathrm{m} \cdot \mathrm{n}$). Thus, the more opposite charges, the stronger binding is observed.

	pH = 6			
	Charge	Relative fraction	Charge	Relative fraction
Phosphate buffer (−)	1−	94%	2−	6%
Arg ($^+$)	1+	100%		
Scaling factor $\lvert\text{charge}_{\text{buffer}} \cdot \text{charge}_{\text{AA}}\rvert$	1	94%	2	6%
Calculated binding affinity	$(1 \cdot 94) + (2 \cdot 6) = 106$			
Bindig affinity scaled to the experimental values	6461			

Table 5.3: Example of the calculation of the binding affinity for the arginine homopeptide to the MNPs in presence of the phosphate buffer, at pH 6.

In Table 5.3, the buffer/amino acid proportions at pH 6 are presented. At this pH, there is 94% of $H_2PO_4^-$ species and 6% of HPO_4^{2-} species. Concerning the amino acid (Arg), only the singly charged species (1+) are available. Thus, the whole amount of peptide is available for the adsorption reaction. As the buffer species are available in excess, out of the 100% of charged amino acid species, 94% will react with nanoparticles coated with singly charged buffer species and 6% will react with NPs coated with doubly charged buffer species. Assuming that the binding energies are dominated by the Coulomb interaction, these two reaction efficiencies are then scaled with different factor, which is proportional to product of charges of buffer and amino acid species. The obtained values, here 94 and 12 for singly and doubly charged buffer species coating the nanoparticle, respectively, are added and taken as characteristic for the peptide under the considered conditions. These characteristic values are assumed as being proportional to the Gibbs free energy and can be compared with the experimentally obtained scores.

The introduced procedure was carried out for all charged peptides with respective buffers providing oppositely charged species. Altogether 12 data points were considered. The obtained results were compared to the experimentally obtained binding affinities, both recalculated to ΔG expressed in [kJ mol^{-1}]. The correlation plot of the theoretical and experimental results is given in Figure 5.7. Overall a good agreement can be observed.

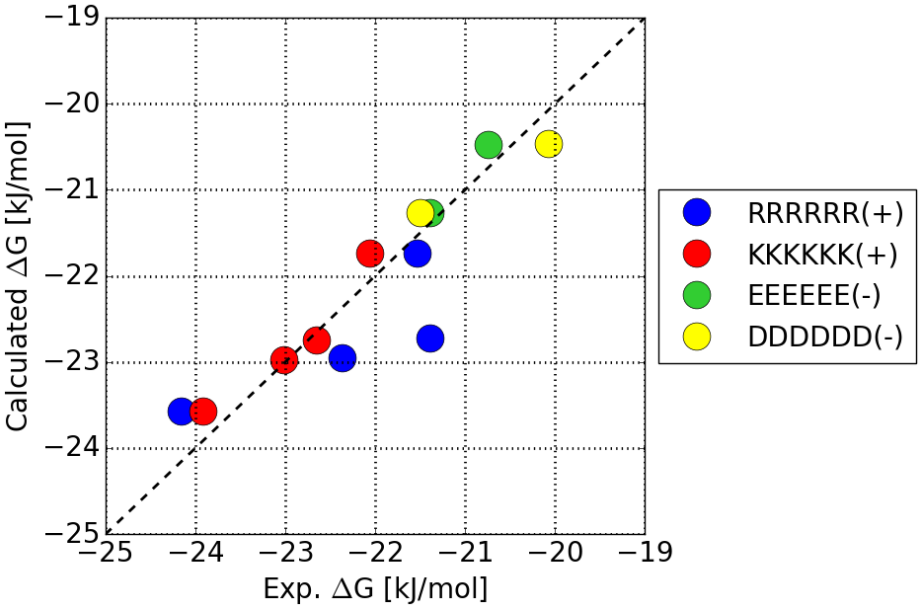

Figure 5.7: Comparison of the theoretically (Calculated ΔG) with experimentally (Exp. ΔG) obtained binding affinities, for charged homopeptides in oppositely charged buffers and different pH. All values were recalculated to be proportional to Gibbs free energy of binding. In the given example the ΔG was obtained with the equation $\Delta G = -RT \ln(K)$, where K is assumed to be proportional to the calculated or experimental score.

5.1.3 Reactions of the uniformly charged species

Up to this point, only situations where oppositely charged buffer and peptides were considered. Binding is also observed in cases where the buffer and the amino acids possess the same charge. The behavior is the same for both the positive and the negative charges, and here only the first case is presented. In this case competitive reactions take place. Now, the buffer competes with the amino acid and does not mediate in binding as before.

Here, several possibilities are considered, depending on the relation of the equilibrium constants of the two reactions, first reaction of the buffer with NPs, and second of the AA with NPs.

$$2\mathrm{NPB^{n+}} + \mathrm{AA^{m+}} \rightleftarrows \mathrm{NPAA^{m+}} + \mathrm{NPB^{n+}} + \mathrm{B^{n+}} \quad \text{if } \mathrm{pK_{NPB^{n+}}} \approx \mathrm{pK_{NPAA^{m+}}} \tag{5.6}$$

In this case we achieve equal amounts of products (the $\mathrm{NPAA^{m+}}$ and $\mathrm{NPB^{n+}}$), when the pH of the solution is approximately equal to $\mathrm{pK_a}$. Because both reactions occur with a similar preference, the amino acid substitutes half of the buffer species from $\mathrm{NPB^{n+}}$. In case of unequal $\mathrm{pK_a}$ values, the buffer can only be partially substituted by the amino acid.

$$\mathrm{NPB^{n+}} + \mathrm{AA^{m+}} \rightleftarrows \mathrm{NPAA^{m+}} + \mathrm{B^{n+}} \quad \text{if } \mathrm{pK_{NPB^{n+}}} \ll \mathrm{pK_{NPAA^{m+}}} \tag{5.7}$$

In the next case, the reaction of the amino acid with the nanoparticle dominates and all buffer species which were bound to the nanoparticles are replaced by the AA species.

$$\mathrm{NPB^{n+}} + \mathrm{AA^{m+}} \rightleftarrows \text{no reaction} \quad \text{if } \mathrm{pK_{NPB^{n+}}} \gg \mathrm{pK_{NPAA^{m+}}} \tag{5.8}$$

In the last case, the buffer species are binding to the nanoparticle much stronger than the amino acid, so there is no possibility of substituting the buffer, thus the AA does not bind to the NP.

In general, for equally charged species it is not possible to predict binding affinities for completely new conditions, since the reaction constants of these reactions are unknown. In Figure 5.8, relative fractions of the Tris buffer species for two pHs are shown. For the same pHs, in Figure 5.9 the experimentally obtained binding affinities for positively charged peptides are shown. Comparing these plots one can notice that the more of the charged buffer species are in the solution the fewer equally charged peptides bind to the NPs.

I assume that the above mentioned dependence between the affinity of the peptides to the NPs (proportional to K) and the molar fraction of charged buffer species is linear. The function describing this dependence is the same for all equally charged peptides in particular conditions. In the peptide-binding process there are two consecutive reactions.

First, the reaction of buffer and nanoparticles

$$\mathrm{NP^0} + \mathrm{B^{n+}} \rightleftarrows \mathrm{NPB^{n+}}, \tag{5.9}$$

with the equilibrium constant equal to,

$$K_{\mathrm{NPB^{n+}}} = \frac{[\mathrm{NPB^{n+}}]}{[\mathrm{B^{n+}}][\mathrm{NP^0}]}. \tag{5.10}$$

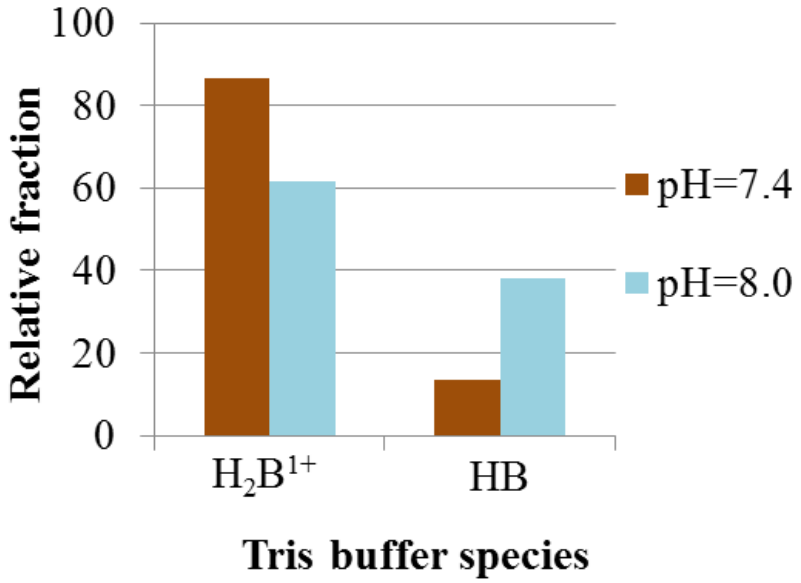

Figure 5.8: Composition of the Tris buffer at pH 7.4 and 8.0.

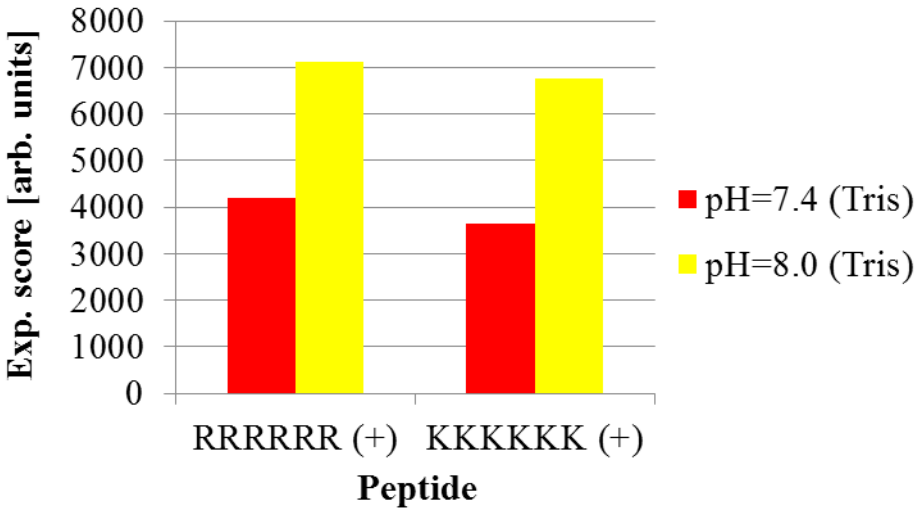

Figure 5.9: Experimentally obtained binding affinities of positively charged homopeptides in Tris buffer at pH 7.4 and 8.0.

Second, the reaction of amino acid species and nanoparticles

$$\mathrm{AA^{m+}} + \mathrm{NP} \rightleftarrows \mathrm{NPAA^{m+}} \tag{5.11}$$

The equilibrium constant is equal to,

$$K_{\mathrm{NPAA^{m+}}} = \frac{[\mathrm{NPAA^{m+}}]}{[\mathrm{AA^{m+}}][\mathrm{NP}]}. \tag{5.12}$$

We know that these are concurrent reactions, and that the reaction of nanoparticles with buffer takes place before the reaction of AA with NP, so the concentration of the nanoparticles which can react with AA is equal to:

$$[\mathrm{NP}] = [\mathrm{NP^0}] - [\mathrm{NPB^{n+}}] = [\mathrm{NP^0}] \left(1 - \frac{[\mathrm{NPB^{n+}}]}{[\mathrm{NP^0}]}\right), \tag{5.13}$$

and

$$\frac{[\mathrm{NPB^{n+}}]}{[\mathrm{NP^0}]} = K_{\mathrm{NPB^{n+}}}[\mathrm{B^{n+}}]. \tag{5.14}$$

Thus

$$[\mathrm{NP}] = [\mathrm{NP^0}] \left(1 - K_{\mathrm{NPB^{n+}}}[\mathrm{B^{n+}}]\right). \tag{5.15}$$

Also the equilibrium constant is related to the change of the standard Gibbs free energy of the reaction between nanoparticles and amino acids with equation,

$$\Delta G_{\mathrm{NPAA^{m+}}} = -RT \ln K_{\mathrm{NPAA^{m+}}}. \tag{5.16}$$

One can transform it to obtain an equation for the equilibrium constant of the peptide-binding reaction:

$$K_{\mathrm{NPAA^{m+}}} = e^{-\frac{\Delta G_{\mathrm{NPAA^{m+}}}}{RT}}. \tag{5.17}$$

The concentration of the nanoparticles bound to the AA can be expressed by:

$$[\mathrm{NPAA^{m+}}] = K_{\mathrm{NPAA^{m+}}}[\mathrm{AA^{m+}}][\mathrm{NP}] = e^{-\frac{\Delta G_{\mathrm{NPAA^{m+}}}}{RT}}[\mathrm{AA^{m+}}][\mathrm{NP^0}] \left(1 - K_{\mathrm{NPB^{n+}}}[\mathrm{B^{n+}}]\right) \tag{5.18}$$

While $[\mathrm{AA^{m+}}]$ and $[\mathrm{NP^0}]$ are constant for all experiments, $K_{\mathrm{NPAA^{m+}}}$ needs to be proportional to $[\mathrm{NPAA^{m+}}]$ and this corresponds to the affinity of the peptide to the NP which is observed in the experiment.

Now, we can calculate Gibbs binding free energy for a given $[\mathrm{NPAA^{m+}}]$. To calibrate the model in this situation I need at least two values of experimentally obtained affinities, for two charged peptides, fit them with two linear functions and make an average of these two, see Figure 5.10.

Using this averaged function as presented in Figure 5.10, we can predict the binding affinities of charged peptides to the NPs in the considered buffer when equally charged species (of buffer and AA) are present.

In Figure 5.11 results obtained using the average function of Figure 5.10 are presented, for

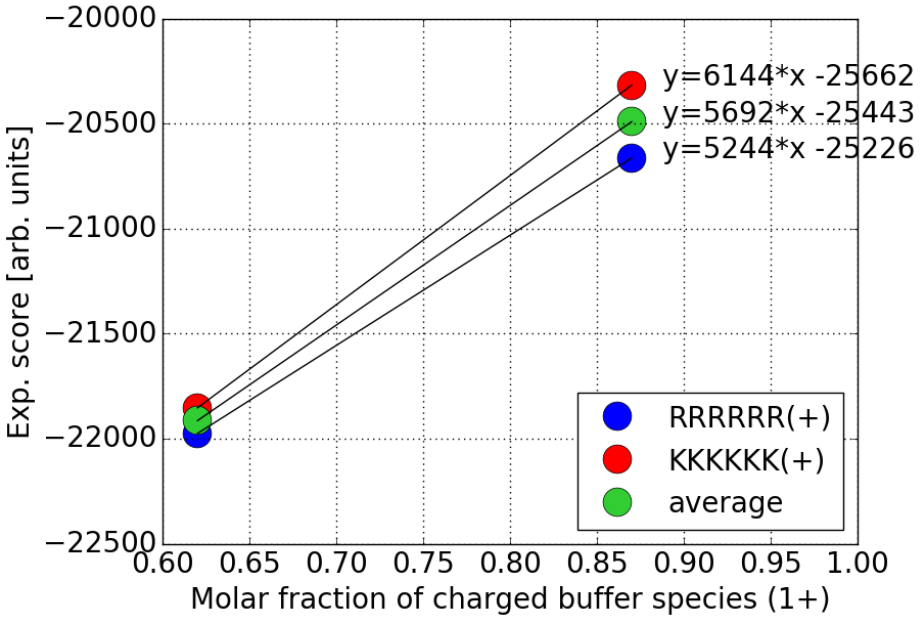

Figure 5.10: Experimentally obtained binding affinity of two positively charged homopeptides correlated with the molar fraction of singly positively charged buffer species, fitted with a linear function.

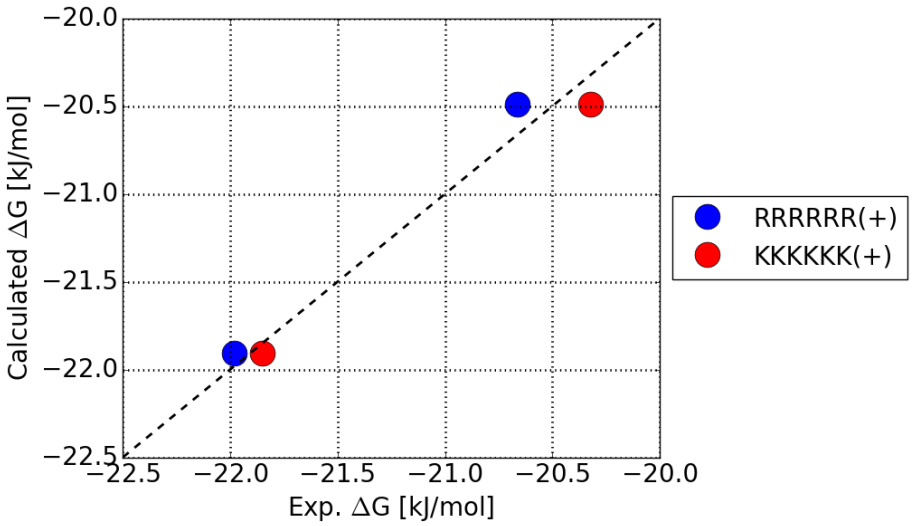

Figure 5.11: Comparison of the theoretically and experimentally obtained binding affinities for positively charged homopeptides in presence of singly-positively charged buffer Tris, at pH 7.4 and 8.0.

two positively charged homopeptides in presence of the singly-positively charged buffer Tris, and at two pH 7.4 and 8.0. The results obtained with the model fit well to the experimental affinity, nevertheless additional improvement could be achieved by a calibration of the function to other pH conditions.

5.1.4 Summary

Combining the methodology presented in this chapter, carrying out a detailed analysis of the experimental results, we are able to reproduce the binding affinities of charged amino acids to magnetic nanoparticles. As shown in Figures 5.7 and 5.11, the calculated values, proportional to Gibbs free energy, present a trend similar to the experimental observations. This may be a valuable input for understanding the complicated phenomena of reactions between nanoparticles and amino acids. Additionally, this model gives an insight how each of the process stages can be influenced in order to obtain desired results.

5.2 Calibration of the EISM against experimental data

In this chapter the results of the peptide array experiment, were used for calibration and evaluation of the EISM model. These experiments were carried out for chosen peptides, for which the binding abilities to the magnetic nanoparticles in various solvents and pHs were investigated. There were two membranes of peptides provided by the experimentalists from TUM. The first membrane containing homopeptides, see Figure 5.12, was used to calibrate the EISM model. The second membrane containing different peptide compositions, see Figure 5.14, was used to validate the EISM model, by checking its ability to reproduce the experimental findings. The experiment which is considered here was carried out in pH = 7.4 and in presence of the Tris(hydroxymethyl)aminomethane (Tris) buffer.

5.2.1 Method of calibration

In order to make the EISM applicable for the chosen peptides, surfaces and experimental conditions (pH, solvent) a calibration of its parameters is required. For this purpose, experimental data, obtained for peptide arrays containing peptide chains built of the same amino acid, homopeptides, are required. With this data the binding affinity of a single amino acid in the EISM model, namely, the γ_i of the Eq. 3.20, could be obtained as described in Chapter 4.1. The obtained affinities for all amino acids used in the EISM model are shown in Figure 5.13.

Analyzing the experimental results for the first membrane, with homopeptides, we can see that practically only for the charged peptides a clear binding occurs, see Figure 5.12. The other peptides are showing weak binding, or no binding at all as their affinities are located below the noise level, marked in the graph with the orange line.

There is a direct relation between an experimentally measured affinity of a homopeptide (Figure 5.12) and the affinity of a single amino acid used in EISM for the simulations (Figure 5.13), see Chapter 3.4 for the details. The binding affinities for single amino acids were chosen as proportional to binding affinities of respective homopeptides, see Chapter 4.1 for the parametrization procedure, except for the values close and below zero, all of them are set to the γ_i=0.

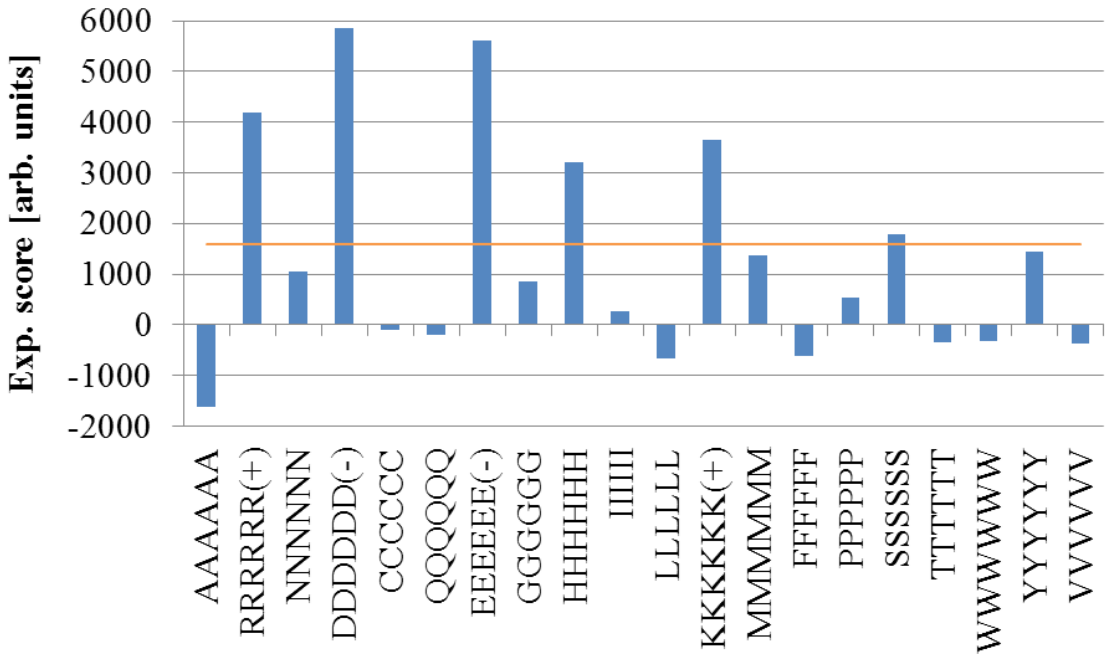

Figure 5.12: Results of the peptide array screening experiment, binding affinities for homopeptides made of all twenty amino acids.

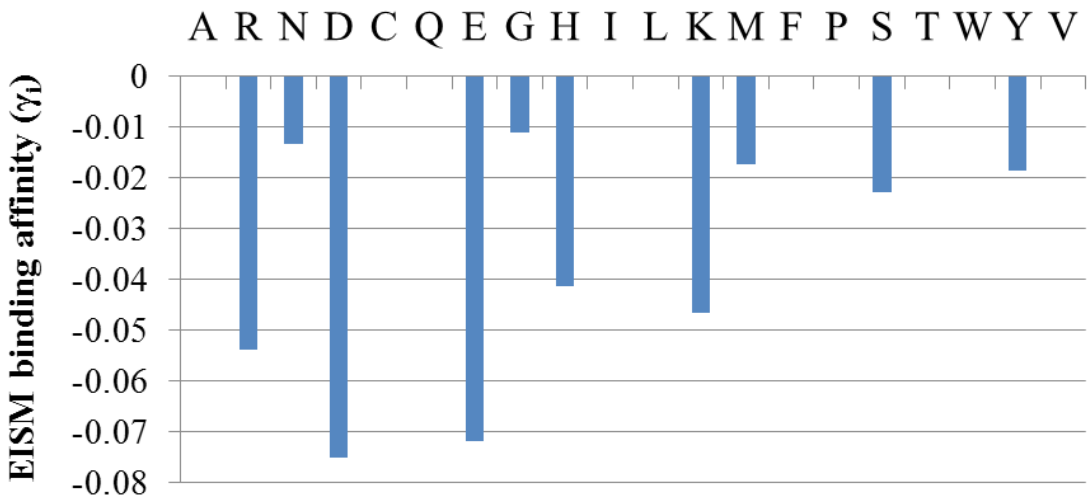

Figure 5.13: Binding affinities, γ_i of Eq. 3.20, for all twenty amino acids as used in the EISM model.

5.2.2 Validation of the calibration

With the calibrated EISM, the free energies of binding (ΔG) of various peptides present in the second peptide array to magnetic nanoparticles were considered theoretically. In all plots, where binding of peptides to the nanoparticles obtained by the EISM is compared to the experimental data, the experimental binding affinity is converted to Gibbs free energy using the relation with the equilibrium constant $\Delta G = -RT \ln K$, where K is proportional to the experimental score.

The theoretically obtained free energies of binding to the magnetic nanoparticles were rescaled to match the range of the experimental data, by multiplying them by a factor of 0.18. Sequences of the considered peptides and their experimental binding affinity are collected in Figure 5.14. I focused mostly on the peptides containing aspartic acid (D) in the sequence, which was the best binding amino acid according to the results from the first membrane, see Figure 5.12. As it was explained in Chapter 5.1, the fact that D is a negatively charged amino acid and there are positively charged buffer species in the solution is crucial for strong binding.

5.2.2.1 D homopeptides

First, the EISM simulations were carried out for D homopeptides. In Figure 5.15, a comparison of the experimentally obtained free energies of binding (ΔG) with the calculated and scaled values of ΔG obtained with the EISM model, for these peptides is shown. The number of Ds in the sequence is continuously increased from 4 to 10. A good agreement between the experimental and theoretical results can be observed.

A clear trend can be observed, namely, the more Ds in the structure, the better binding. This observation is valid both for the EISM simulations and the experimental findings. An exceptionally similar binding is observed for 5D and 6D, and it should be underlined here, that this effect occurs both, for the calculated and the experimental results. It can be explained by the flexibility of the peptide chain. Depending on the number of amino acids in the sequence, a different number of the side chain atoms has a possibility to be close to the surface. To demonstrate this effect Figure 5.16 shows the energetically most favorable structures of the 5D and 6D peptides. Here, the peptides are seen, from the surface perspective. The atoms are colored according to the distance from the surface. The red color corresponds to atoms which are closer to the surface, whereas, the blue to those that are further. The black arrows mark the groups responsible for the binding.

In Figure 5.17 the distance of the terminal C-atoms, located on the side chains of the D residues, from the surface of magnetite is plotted. This graph approximately represents the shape of the peptide above the surface. In the 5D peptide four side chains are close to the surface (below 4 Å), and one is further away (above 4 Å). In case of the 6D structure, in turn, three side chains are close and three are further away. Looking at the structures in Figure 5.16, the side chains of the 6D peptide are close to the surface and lie flatter on the surface (not only the terminal atoms are close), in a trap of a local minimum. This, however, prevents the 6D peptide from changing the conformation and exposing more binding groups to the surface. Therefore, the 6D peptide, despite a larger amount of strong binding residues, has a binding similar to the shorter 5D peptide.

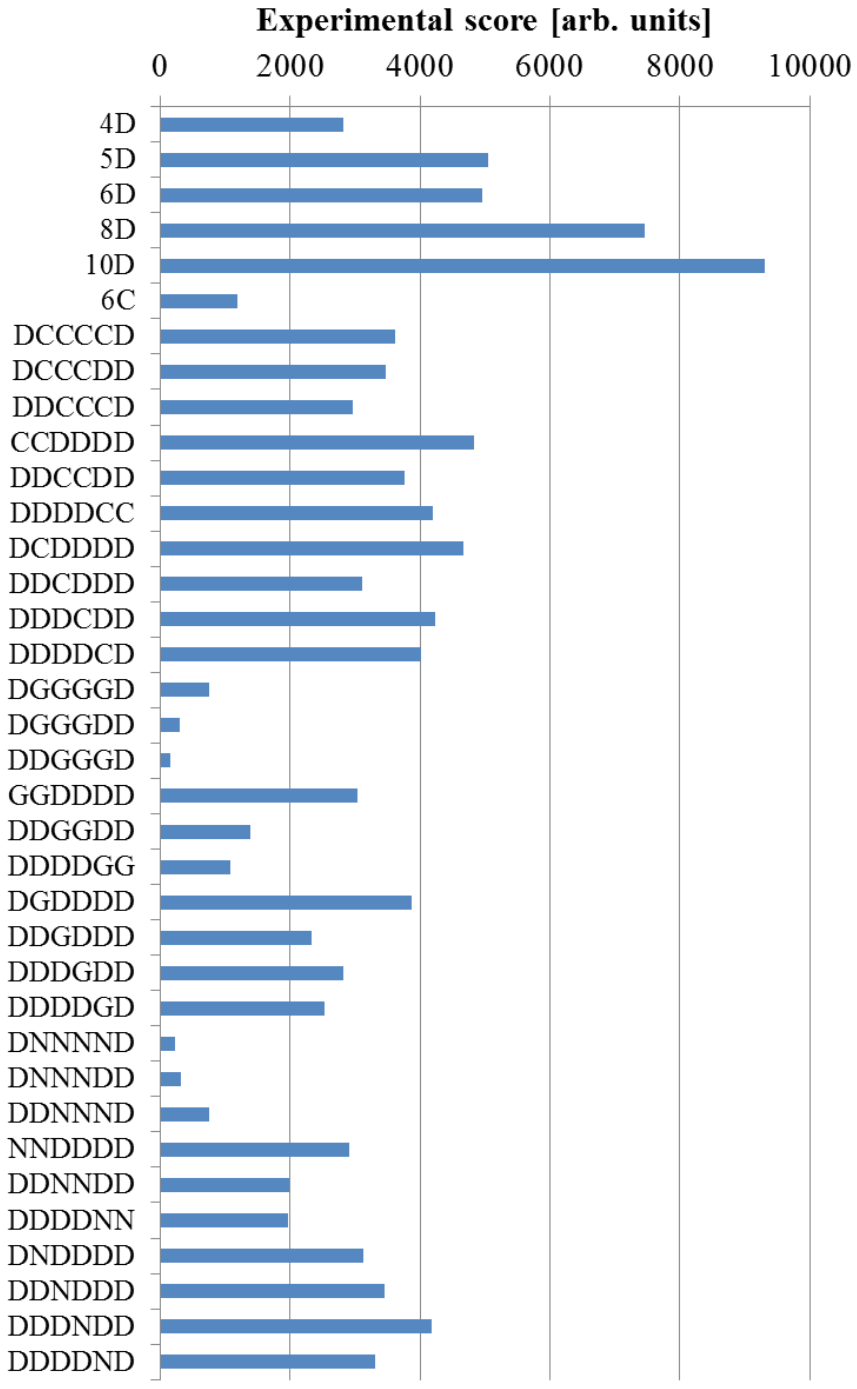

Figure 5.14: Experimentally obtained binding affinities for designed set of peptides, collected on the second membrane.

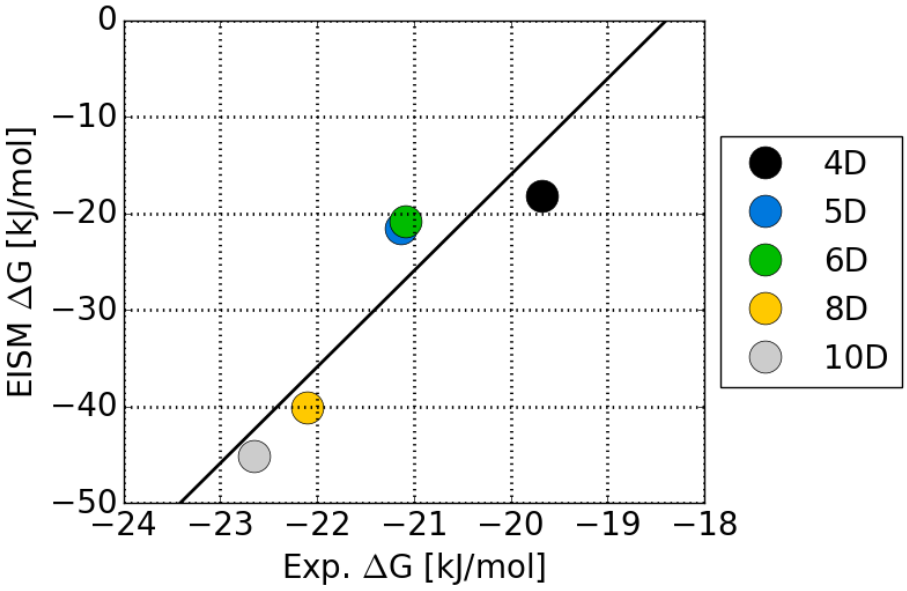

Figure 5.15: Comparison of the binding affinities obtained with the EISM model calibrated against data from the peptide array screening for the first membrane and the experimentally obtained binding affinities for D homopeptides present on the second membrane. Linear fit: $f(x) = 9.97x + 183.31$.

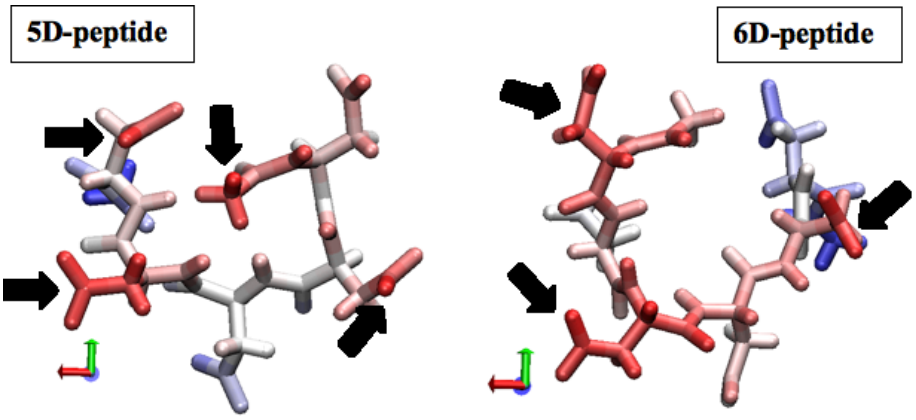

Figure 5.16: Energetically most favorable structures of 5D and 6D peptides as seen from the surface. See text for the description.

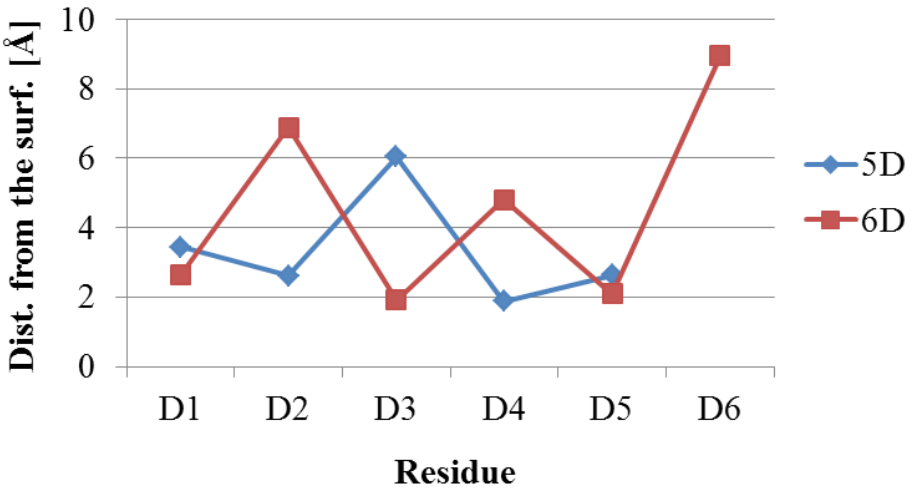

Figure 5.17: Distance from the surface for the carbon atoms terminating the side chains of all residues of the 5D and 6D peptides.

5.2.2.2 Effects of mutations

Subsequently the peptides containing not only aspartic acid (D) in the sequence, were mutated with different amounts of cysteine (C), glycine (G) or asparagine (N). Interestingly, these additional amino acids themselves are weak binders. All of the peptides considered here have six residues. Ds in different configurations in the structures are combined in different ratios with one of the mentioned weak binders, i.e., C, G and N. In Figure 5.18 calculated binding affinities are compared with the experimental data for peptides being built of respectively one, two, three and four cystein amino acid. In general good agreement is observed, however, two cases, DCCCCD (purple dot) and DDCDDD (orange dot), show larger deviations.

To have better insight into relation between sequence of amino acids and free energy of binding (ΔG), an additional analysis is performed.

Starting from the DDDDDD homopeptide, one, two, three and four Ds are respectively replaced by Cs, in different configurations. In the last sequence all Ds were substituted with Cs giving a CCCCCC homopeptide. In Figure 5.19 the binding free energies are plotted against the number of cysteine residues in the structure for the whole set of peptides. The obtained relation is intuitive, the fewer well binding Ds in the sequence the smaller ΔG of the entire peptide. It is noteworthy that different peptides containing one cysteine (C) and five aspartic acids (D) despite the same number of components, manifest different binding affinity depending on the position of the C residue. A similar effect an be observed for peptides containing two Cs. For larger number of Cs the differences became negligible.

In the next step a similar analysis was carried out for D-peptides with different numbers of glycine (G) substituents in the sequence. The EISM calculated binding affinities are compared with the experimental results in Figure 5.20. In this case a better agreement is observed. Similarly like in the previous case, the sequence with four weak binders, DGGGGD (black dot), does not fit to the trend line.

For singly G-substituted peptides various binding affinities are observed, depending on the position of the substitution, Figure 5.21. Here, the differences are even larger, than in the case of cysteine.

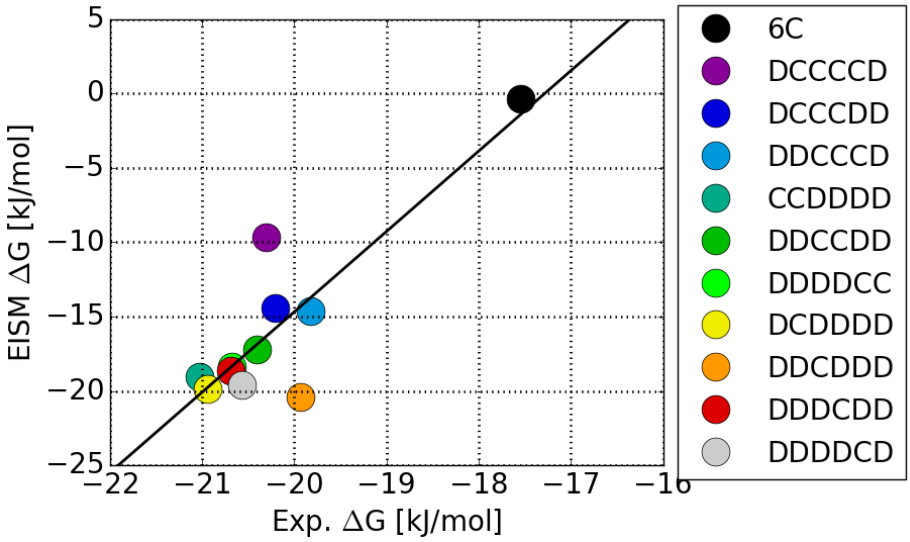

Figure 5.18: Comparison of the calculated and experimental binding affinities for peptides containing D and C amino acids. Linear fit: $f(x) = 5.40x + 93.39$.

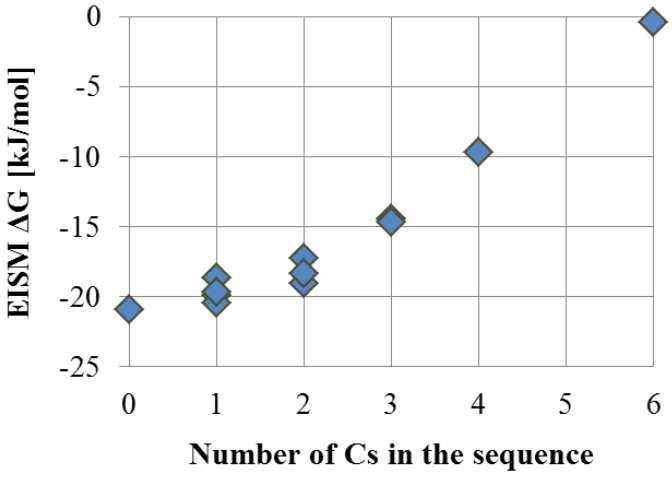

Figure 5.19: Relation between the number of C substituents in 6D peptides and the EISM binding affinity.

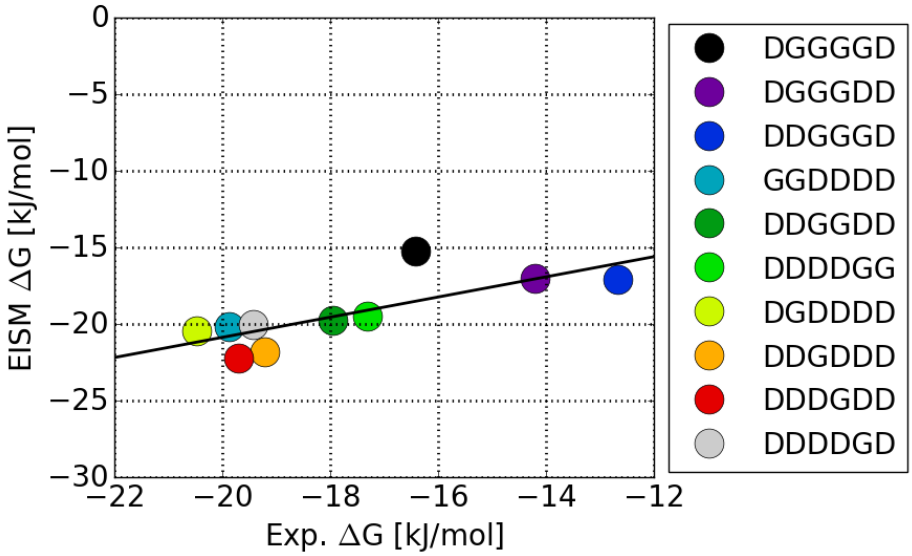

Figure 5.20: Comparison of the calculated and experimental binding affinities for peptides containing D and G amino acids. Linear fit: $f(x) = 0.66x - 7.69$.

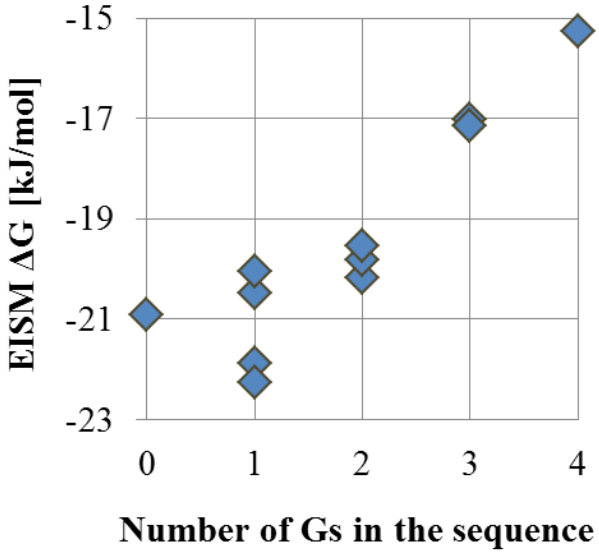

Figure 5.21: Relation between the number of G substituents in 6D peptides and the EISM binding affinity.

The binding free energy for the 6D homopeptides upon a single G replacement is maximally increasing for about 1.3 kJ mol^{-1} (DDDGDD) or decreasing for about 0.9 kJ mol^{-1} (DDDDGD). This indicates how a position of a small amino acid influences the flexibility of the chain and consequently the binding affinity. This also means that the free energy of binding is not a simple sum of the binding affinities of all amino acids, but also the order in the sequence matters. In Figure 5.22 the structures of two interesting sequences are presented, DDDDGD and DDDGDD. Again, the red-colored atoms are closer to the surface, and the blue-colored are further. DDDDGD is more bent than DDDGDD, which is the strong binder.

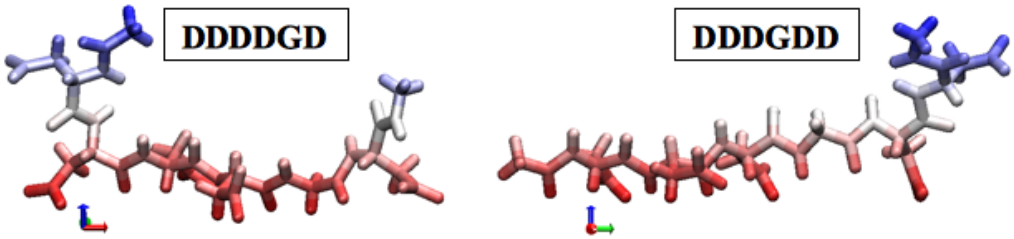

Figure 5.22: Two conformers of sequence containing 5D and one G amino acids with different total energies, lying above the surface, side view.

Next, these two peptides are compared with the unsubstituted 6D homopeptide, to find a relation between the structure and the binding affinity. Specifically, to explain, why the potentially best binder 6D, based on the strong interaction of the amino acid, does not differ from the monosubstituted sequences.

In Figure 5.23, a comparison of the distances of the outermost carbon atoms located in the side chains of each residue from the surface is shown. Two peptides have five Ds in the sequence (DDDDGD and DDDGDD) of which four are bound to the surface. On the other hand in the 6D peptide only three Ds are close to the surface and the other residues are rather far from the surface and effectively they do not contribute to the binding. All in all, these three structures have almost equal binding affinity.

A similar analysis was performed for mutants with asparagine (N). A good agreement of the calculated and experimental ΔG values is observed, see Figure 5.24. In Figure 5.25 the influence of the number of substitutions on the binding affinity is shown. Here, as in the previous example a similar trend is observed, with a large derivation for singly substituted sequences.

5.2.3 Summary

In this chapter, a calibration of the EISM model γ_i parameters with respect to the experimental results was introduced. This calibrated EISM model was used to investigate the influence of mutations on the binding of hexapeptides to the magnetite surface. Independently of the type of the weak binding amino acid the observed trends were always similar. It can be noticed that for sequences containing six amino acids with high binding affinity, substitution of two and more by amino acids with a low binding ability decreases the free energy of binding. However, when only one strong binder is substituted by a weak one, we

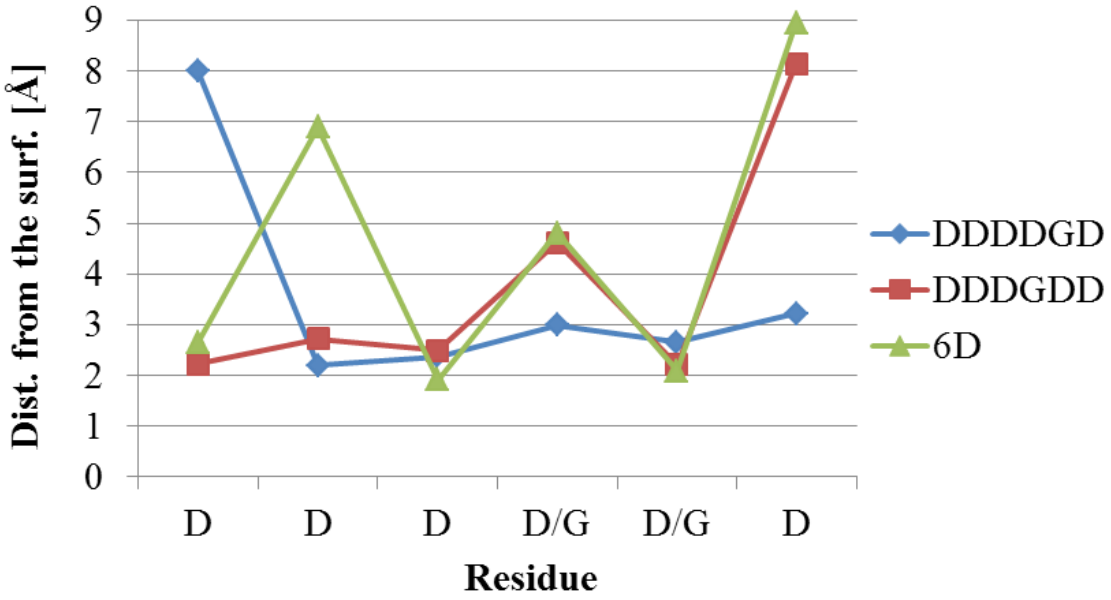

Figure 5.23: Distance from the surface for the carbon atoms terminating the side chains of all residues of the 6D homopeptide and its two mutants with one D replaced by G.

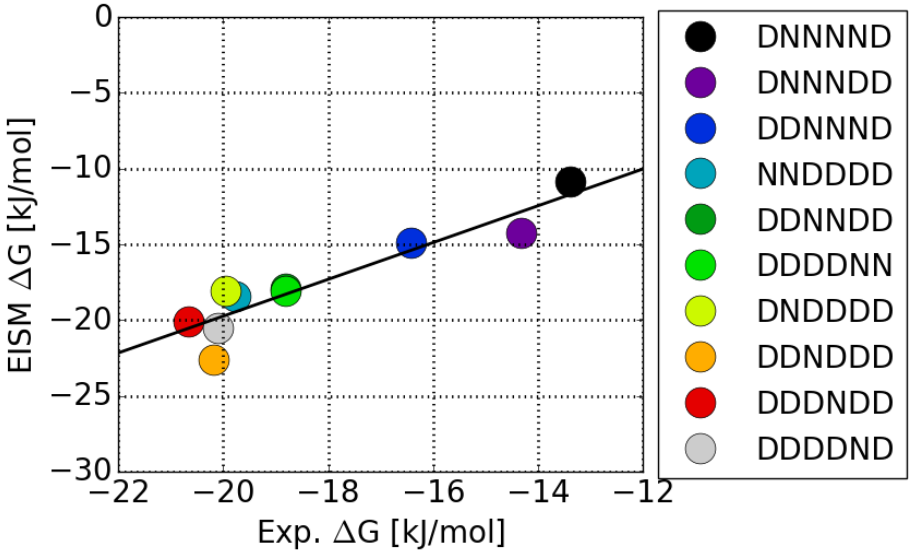

Figure 5.24: Comparison of the calculated and experimental binding affinities for peptides containing D and N amino acids. Linear fit: $f(x) = 1.22x + 4.56$.

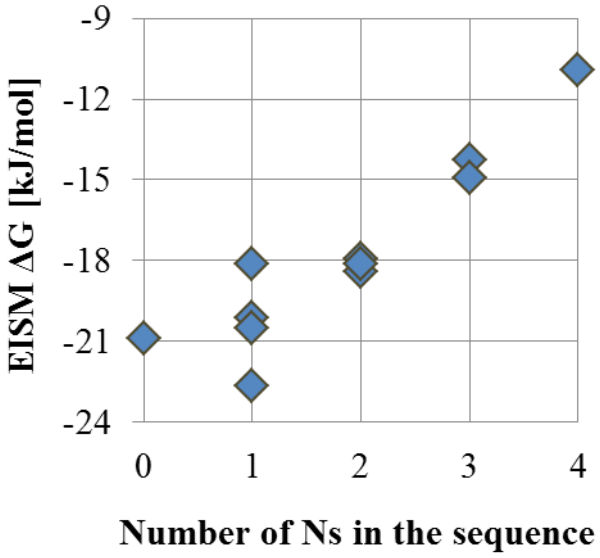

Figure 5.25: Relation between the number of N substituents in 6D peptides and the EISM binding affinity.

can achieve an increase, a decrease or no change in the binding strength, depending on the position of the substitution. This effect can be explained by the influence of the position of the substitution on the flexibility of the peptide's chain. This in turn influences its ability to expose its binding groups toward the surface.

5.3 Towards a theoretical peptide design

In this chapter a theoretical study of the sequence-affinity relation, based on EISM simulations, for peptides of different lengths and compositions is presented. Binding affinities for the amino acids building the peptides are the same as in Chapter 5.2, i.e., they are calibrated with respect to the experimental results obtained at pH 7.4 in Tris buffer. First, I will focus on sequences containing only amino acids with high binding affinity, namely, pure aspartic acid (D) chains or its mixtures with glutamic acid (E). The values of the binding free energies presented here are not scaled to the experimental values, so they lie in a different range. However, they are not supposed to be compared to the experimental ones, and only changes in the binding affinities for various sequences are of interest.

5.3.1 Strong binders

I started from the analysis, how the extension of the length of a D-homopeptide reflects in its binding free energy, see Figure 5.26.

The dependence of the binding free energy with respect to the number of D residues in the sequence is roughly linear. This shows that although the EISM model is simple, ΔG is not a simple sum of the binding affinities of all amino acids in the sequence. However, additional effects are present, mainly due to the structure of the peptide chain at the surface. In the graph, there are also regions, where the binding is nearly equal for sequences with various number of Ds, e.g., 5–6D and 10–12D peptides. This indicates that the flexibility

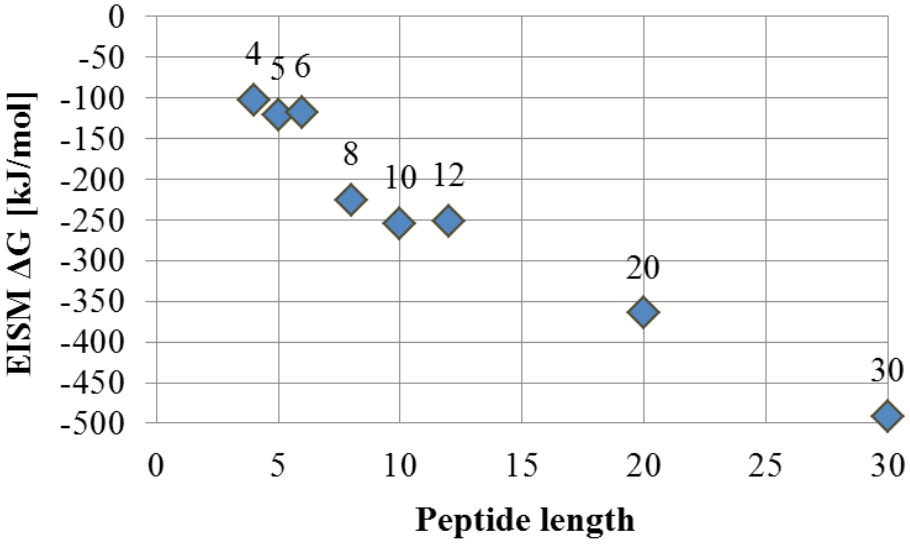

Figure 5.26: Relation between the length of D-homopeptide and the theoretically obtained binding affinity.

is important not only in hetero-, but also in homopeptides, cf. Chapter 5.2.2.2.

5.3.2 Mutations with strong binders

In the next step, the D-homopeptides are extended with glutamic acid (E). Both D and E are strong-binding amino acids, with EISM binding parameters of -0.0752 and -0.0719, respectively. In Figure 5.27 the dependence of the EISM ΔG on the number of added E residues is presented. Starting from the 6D sequence (0 E on the plot) the number of added Es is increased by adding symmetrically located 2, 4 and 6 Es, giving DDEDDEDD (2E), DEDEDDEDED (4E), and DEDEDEDEDEDE (6E) sequences, respectively.

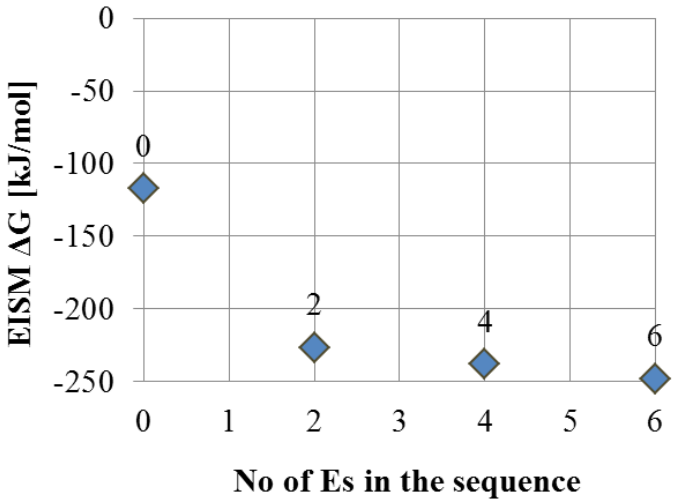

Figure 5.27: Relation between the length of D-homopeptide, with different number of additional E amino acids, and the theoretically obtained binding affinity.

In the beginning, from 0E to 2E, the addition enlarges the binding affinity drastically, for more than 100 kJ mol^{-1}. The two further extensions are not as strong as the first one, and increase the binding strength by around 10 kJ/mol. These observations are consistent with findings for the pure D sequences, in Chapter 5.3.1. In some ranges of the peptide chain length, here 8, 10 and 12 amino acids, the binding abilities are very similar, showing a linear trend. This suggests that the longer chains, despite a larger number of potentially-binding side chains, cannot expose them to the surface. A small addition of a strong binder in the sequence improves the binding, but for larger amounts this effects weakens. This may be caused by the restriction of rotation, due to steric hindrance of the additional residues.

5.3.3 Mutations with weak binders

Next, the binding behavior of mixed strong-weak sequences is investigated. As model system, different configurations of D peptides mutated with glycine (G) were chosen. In the first example I have analyzed seven sequences containing twelve amino acids each. In all of them the ratio of Ds to the Gs is different. Starting from a 12D-homopeptide, in every step two Ds are replaced by two Gs, to end up with a 12G-homopeptide. The mutated sequences, and corresponding EISM binding free energy are given in Table 5.4. The relation between the number of the G-substituents and the EISM ΔG is shown in Figure 5.28.

Sequence	No. of Gs	EISM ΔG [kJ mol^{-1}]
DDDDDDDDDDDD	0	-251.1
DDDDDGGDDDDD	2	-233.9
DDDDGGGGDDDD	4	-194.2
DDDGGGGGGDDD	6	-163.8
DDGGGGGGGGDD	8	-121.5
DGGGGGGGGGGD	10	-98.3
GGGGGGGGGGGG	12	-35.7

Table 5.4: Sequences of the D homopeptides mutated with G amino acid used for the EISM calculations and their binding free energies.

This dependence shows a linear character with an expected trend. The more strong binders (Ds) are replaced by the weak binders (Gs), the weaker is the binding of the whole peptide.

In order to investigate the influence of the central position of inclusion of the weak binders, four G amino acids are located in the middle of the peptide and a systematically increased number of Ds is added on both ends of the peptide. The considered sequences and their EISM free energies of binding are presented in Table 5.5.

In this case the relation is not exactly linear, see Figure 5.29. The most important difference compared to the previous example is that in this case the length of the peptide is different for each structure. Therefore, the initially linear trend in binding increase is broken when 8 D amino acids are added, namely, a weaker than expected effect occurs. This observation agrees with the previous observation, see Chapter 5.2.2.1, that the caused by a limited flexibility of the chain the binding contribution of the D amino acids is not always equal.

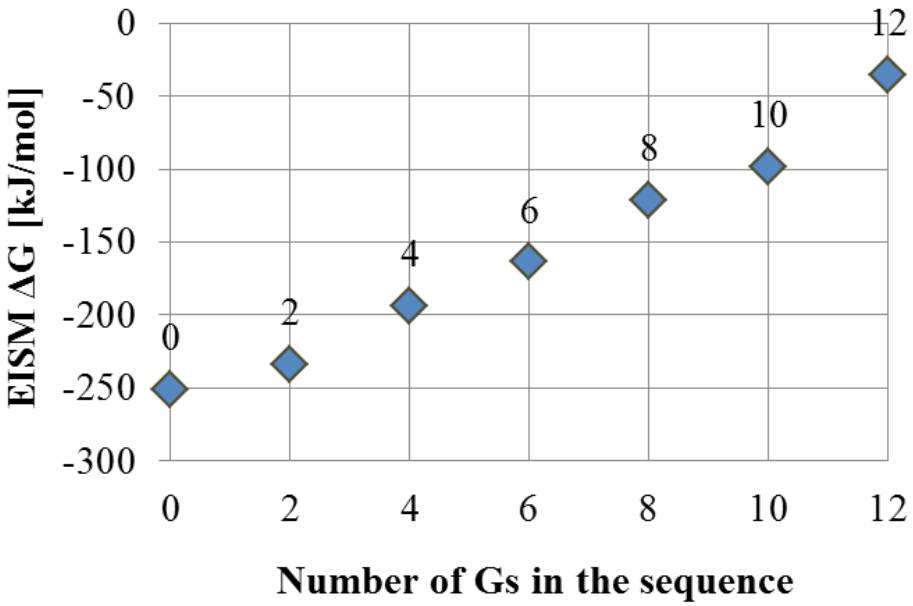

Figure 5.28: Relation between the sequence of 12D-homopeptide, with different number of Ds replaced by Gs, and the theoretically obtained binding affinity.

Sequence	No. of Ds	EISM ΔG [kJ mol^{-1}]
DGGGGD	2	-85.8
DDGGGGDD	4	-134.1
DDDGGGGDDD	6	-182.7
DDDDGGGGDDDD	8	-194.2

Table 5.5: Sequences of the D homopeptides mutated with G amino acid used for the EISM calculations and their binding free energies.

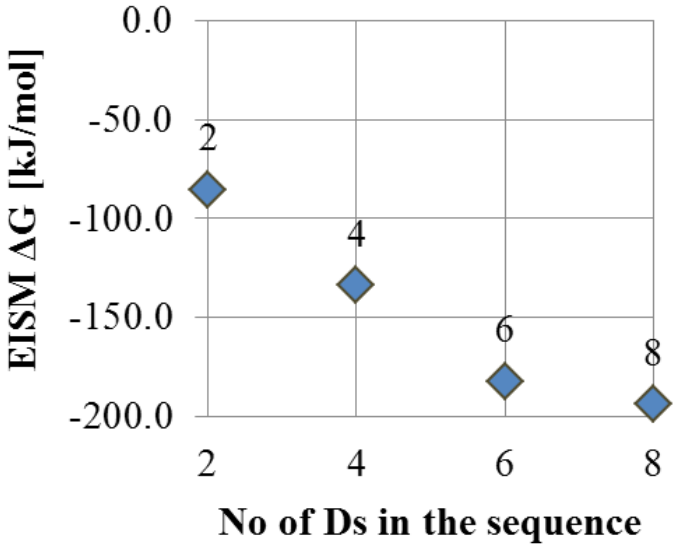

Figure 5.29: Relation between the length of DGGGGD sequence, with different number of Ds on its ends, and the theoretically obtained binding affinity.

Next, the number of strong binders at the ends of the sequence was kept constant, and the weak-binder sequence in the middle was extended. The sequences and their Gibbs free energies of binding are shown in Table 5.6. The relation between the binding affinity and number of the central weak binders is shown in Figure 5.30.

Sequence	No. of Ds	EISM ΔG [kJ mol^{-1}]
DDDDDD	0	-117.6
DDDGGDDD	2	-170.5
DDDGGGGDDD	4	-182.7
DDDGGGGGGDDD	6	-163.8
DDDGGGGGGGGDDD	8	-141.1

Table 5.6: Sequences of the D homopeptides mutated with G amino acid used for the EISM calculations and their binding free energies.

Here, as before, the length of the peptide is different in each case. What is interesting, despite the constant number of the strong binders, already at the beginning (with the first addition of weak binders) the binding affinity is increasing by about 50%. Comparing with the results in Table 5.4, one could expect a small, of ca. 3 kJ mol^{-1}, increase in binding coming from a single G residue. Here, however, the increase is much larger, and amounts to around 26 kJ mol^{-1} per added G residue. This suggests that the larger than expected change must arise from the D residues itself, due to a more effective exposition of the binding side chains to the surface. However, this effect is not continuous and the binding affinity is increasing when up to four Gs are added. Then, it starts to decrease and gets closer to the result achieved for the pure D sequence. This can be caused by an increase of entropy due to higher flexibility. To relate these effects with the structure, a closer look on

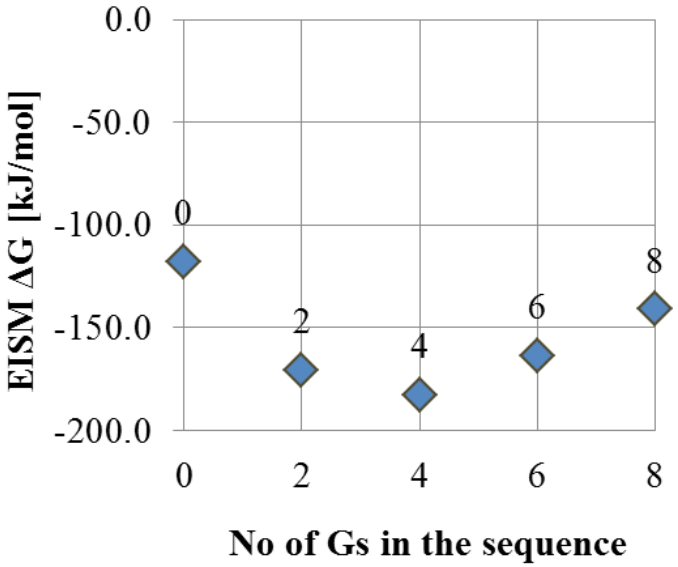

Figure 5.30: Relation between the length of 6D-homopeptide, with different number of additional Gs in the middle of the sequence, and the theoretically obtained binding affinity.

the most characteristic and energetically lowest structures is shown in Figure 5.31.

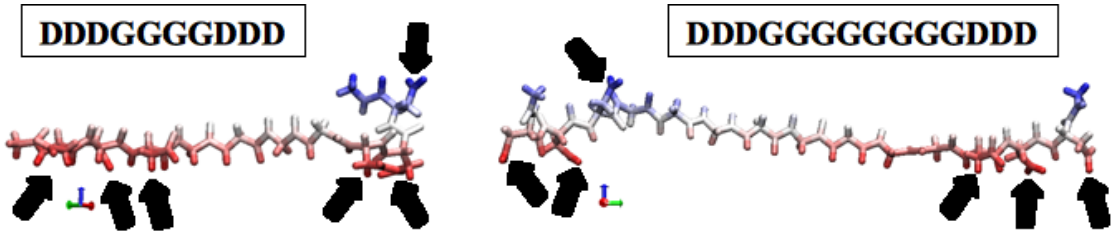

Figure 5.31: Comparison of the two structures of 6D sequences with different number of Gs in the middle, lying above the surface, side view. Black arrows point at the positions of the D residues side chains.

As previously, the red-marked atoms are closer to the surface. From the first look on both peptides, DDDGGGGDDD and DDDGGGGGGGGDDD, it is visible that the first structure lies flatter on the surface. For both of them the side chains of the five D residues are close to the surface and one is further away, see black arrows in Figure 5.31. However, for the shorter peptide, more additional binding can arise from the G residues, which are also close to the surface. For the longer peptide, the added G residues are further away, also giving more flexibility, and thus increasing the entropy. Also the distance of certain residues from the surface can be analyzed, to investigate the differences in the binding affinities. For the structures of Figure 5.31 and the initial 6D peptide, the distance of the outer most carbons from all side chains of all residues in those peptides is plotted in Figure 5.32. The residues assignment is given in Table 5.7.

Here, for all peptides the first three and last three residues are strong binders. It is

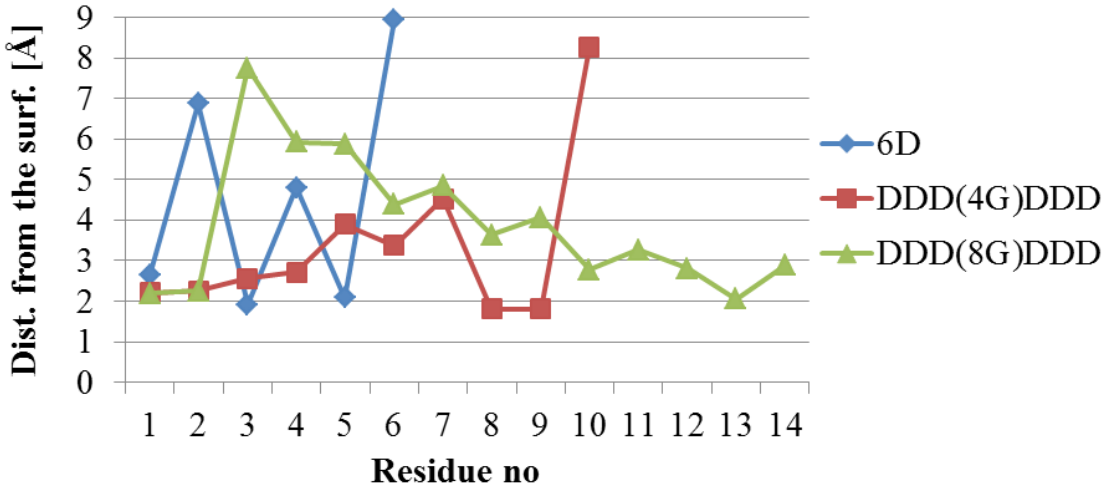

Figure 5.32: Distance from the surface of the carbon atoms terminating the side chains of all residues of the 6D homopeptide and its two mutants with different number of Gs in the middle. See Table 5.7 for the sequences.

Peptide	Residue													
	1	2	3	4	5	6	7	8	9	10	11	12	13	14
6D	D	D	D	D	D	D	-	-	-	-	-	-	-	-
DDD(4G)DDD	D	D	D	G	G	G	G	D	D	D	-	-	-	-
DDD(8G)DDD	D	D	D	G	G	G	G	G	G	G	G	D	D	D

Table 5.7: Detailed peptide sequences with all residues and corresponding residue number.

possible to compare directly which side chains are close to the surface. In the case of the 6D peptide, three Ds are bound, namely, the first, the third and the fifth. For other peptides this number increases to five. This directly shows that the presence of additional amino acids in the sequence is expanding the range of possible torsions. However, for the DDD(8G)DDD peptide, the preferred structure is such that the additional G residues are further away from the surface, and cannot contribute to the binding, hence a weaker binding compared to the DDD(4G)DDD peptide is observed.

5.3.4 Summary

In this chapter it was shown that the EISM model can easily be calibrated against experimental data obtained for homopeptides with fixed length. The model calibrated in this way can be used to reproduce the experimental results for heteropeptides of different lengths with a good agreement. The model was also used to analyze the trends in the experimental results. EISM considers the structures of the peptides at the surface and can predict strong-binding peptides. It can be used for theoretical investigations of the peptide binding. For that reason the EISM model was used to investigate the influence of strong and weak-binding amino acids mutating the sequences on the binding affinities of strong binding peptides. It was shown that an addition of a weak binding amino acid can to some extent increase he binding ability of a strong binding peptides. This can be explained on the basis of an increasing flexibility. All in all this case showed that the EISM model makes a useful framework for analysis and prediction of affinity of peptides to magnetic nanoparticles.

6 Electronic structure of magnetite and its derivatives

Magnetic nanoparticles are inorganic compounds of a still not fully described structure, see Chapter 2.2 for details. The binding of peptides to the surface is essential in this work, however other aspects like the electronic structure and properties of the iron oxides are considered as well. Besides the surface and size effects, the electronic properties of a nanoparticle depend on the electronic structures of the underlying oxide. The iron oxide magnetic nanoparticles are mainly built of two different types of iron oxides, magnetite and maghemite. Therefore, quantum chemical calculations employing density-functional theory (DFT) for a cluster model with point charge field embedding were carried out for magnetite. Additionally, derivatives of magnetite, i.e., ferrites, were considered. They are obtained by replacements of iron ions by zinc and manganese, see Chapter 2.2.2 for more details. For all structures, i.e., magnetite and ferrites, both, the normal and the inverse spinel positions were considered, to check the most stable and favorable conformations.

6.1 Test calculations on model clusters

In order to verify, which of the exchange-correlation functionals should be used, test calculations with three different functionals for the simplest models were carried out. I started from calculations for small clusters for all three metals (Fe, Mn and Zn) surrounded by water molecules both in tetrahedral and octahedral symmetry. For those two types of structures, with different charges of the metal center, bond lengths were compared. These test calculations were also carried out to pick a suitable functional for further calculations on the bigger systems. Iron and manganese atoms were considered in the second and third oxidation state, and zinc in the second. Their electronic configurations are listed in Table 6.1.

The DFT calculations were performed with the TURBOMOLE package[203–205], using three different exchange-correlation functionals: a generalized gradient approximation (GGA) functional PBE[206], and two hybrid functionals, namely, PBE0[207] and B3LYP[208–211]. A def2-TZVP basis set was used for all atoms in the clusters[212], along with the resolution of identity (RI) approximation and a suitable auxiliary basis set[213]. The structures of the clusters taken into consideration were optimized, and are shown in Figure 6.1.

For iron and manganese, depending on the splitting of the metal's d orbitals in the ligand field, different occupations, i.e., low and high spin are possible. Here, for both metals, their high spin electronic configurations were considered, with the maximum number of unpaired electrons. The d-occupations are given in Table 6.2.

For all considered clusters their geometrical structures were optimized in the respective electronic states. The metal-oxygen distances for the final structures obtained with the three exchange-correlation functionals are shown in Table 6.3.

It can be observed that for each structure, the metal-oxygen distances are comparable,

Metallic center	Charge	Electron configuration
Fe	0	[Ar] $3d^6$ $4s^2$
	2+	[Ar] $3d^6$
	3+	[Ar] $3d^5$
Mn	0	[Ar] $3d^5$ $4s^2$
	2+	[Ar] $3d^5$
	3+	[Ar] $3d^4$
Zn	0	[Ar] $3d^{10}$ $4s^2$
	2+	[Ar] $3d^{10}$

Table 6.1: The electron configurations of three metallic centers (Fe, Mn, and Zn) in different oxidation states.

Metallic center	Charge	Electron configuration	Unpaired electrons	
			Low spin	High spin
Fe	2+	[Ar] $3d^6$	0	4
	3+	[Ar] $3d^5$	1	5
Mn	2+	[Ar] $3d^5$	1	5
	3+	[Ar] $3d^4$	0	4
Zn	2+	[Ar] $3d^{10}$	Closed shell	

Table 6.2: Number of unpaired electrons present in different spin configurations of three metallic centers with different charges.

Center	Charge	Symmetry	Me−O distance [Å]		
			PBE	PBE0	B3LYP
Fe	2+	T_d	2.03	2.03	2.04
		O_h	2.15	2.15	2.16
	3+	T_d	1.89	1.93	1.95
		O_h	2.07	2.04	2.06
Mn	2+	T_d	2.09	2.09	2.10
		O_h	2.21	2.20	2.21
	3+	T_d	1.94	1.92	1.93
		O_h	2.05	2.03	2.04
Zn	2+	T_d	2.00	1.99	2.00
		O_h	2.12	2.11	2.12

Table 6.3: The metal-oxygen (Me−O) distances for small clusters containing three metallic centers (Fe, Mn and Zn) with different oxidation states and different geometries.

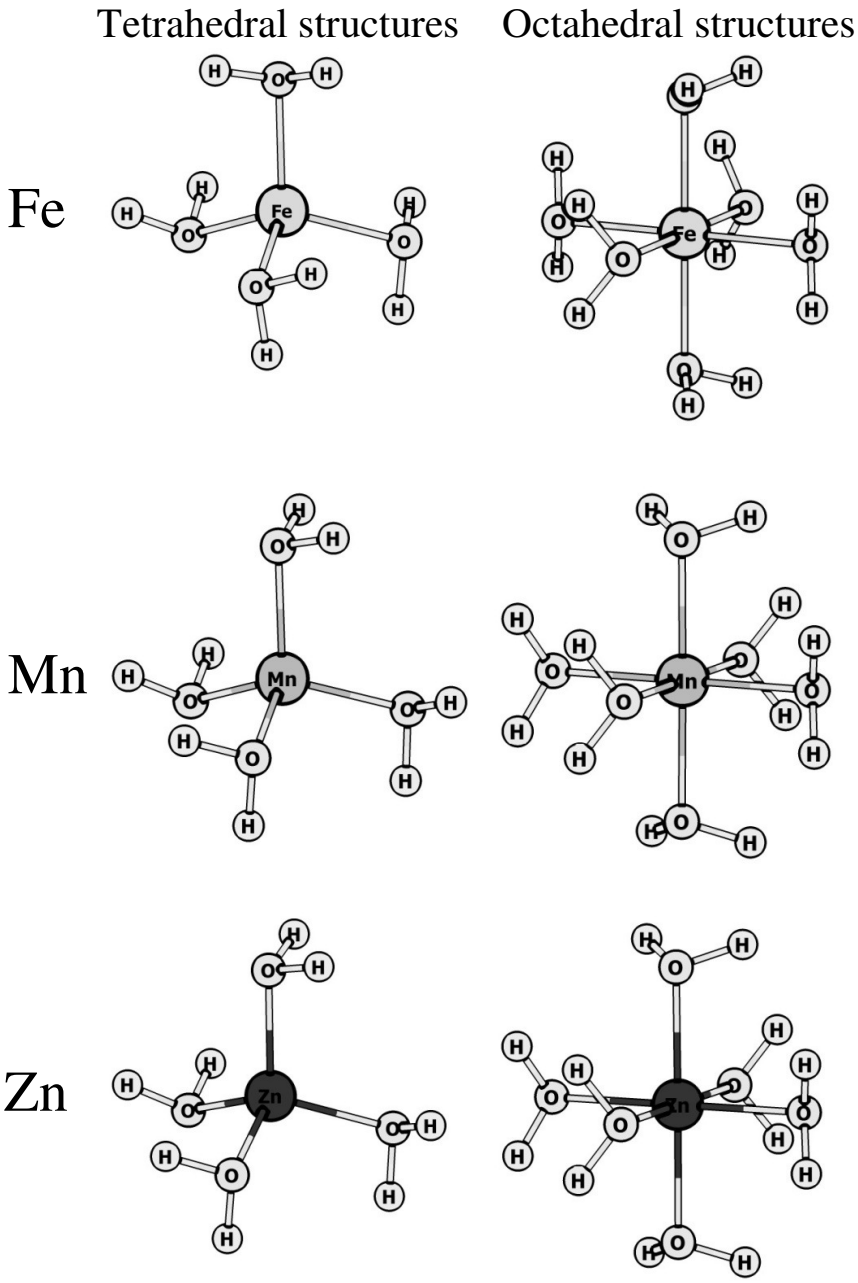

Figure 6.1: The structures of model clusters containing Fe, Mn and Zn metal centers and surrounded by water molecules in both tetrahedral and octahedral symmetry.

regardless the applied exchange-correlation functional.

Since the structural parameters for structures optimized with the GGA and hybrid functionals are similar, the most efficient one, namely the GGA functional PBE was chosen for further calculations. Thus larger structures investigated later in this work could be treated with less effort. Also, to make sure that the PBE functional is good enough, in comparison to hybrid functionals, in the description of the electronic structure of the investigated systems, one needs to check if the same structures (normal or inverse spinel) will be favorable regardless the applied functional.

6.1.1 Inverse and normal spinel systems

The simple clusters introduced in this chapter can serve as a first simplified model for the spinel structures. Comparing the relative energies of the '2+' and '3+' ions in tetrahedral and octahedral surrounding, allows a first approximation of the stability of normal and inverse spinel structures. The total energies of both systems for a given metal composition are obtained as a sum of the according building blocks. Next, the relative energy is calculated with respect to the lower energy of the normal/inverse spinel pair within each functional. The considered compositions and the relative energies obtained with PBE, PBE0, and B3LYP functionals are compared in Table 6.4.

As shown in Table 6.4, for all combinations, built from simple clusters, a normal spinel structure is preferred. This is not consistent with the considerations based on the crystal-field splitting energy presented in Chapters 2.2.1 and 2.2.2. What is shown there, is that normal spinel structure is favorable only for the clusters with Zn^{2+} on the tetrahedral position. In all other cases, the tetrahedral position is occupied by Fe^{3+} or Mn^{3+}, and hence an inverse spinel structure is preferred. Supposedly, such a simplified model of spinels presented here might be not sufficient to approximate the electronic structure of actual spinels, where the three metal centers are direct neighbors and share the surrounding oxygen atoms. In the simplified model the building blocks of a spinel are "decoupled", and thus the electrons are not shared between them, which is the case in the actual spinels. Nevertheless, this model was used as a method evaluation, which functional should be applied in further considerations. The relative energies obtained with the PBE functional varies more than hybrids in most cases, however the trend is always the same (the normal spinel more favorable in all cases), and thus this functional was chosen for further calculations for more reliable models.

6.2 Point Charge Field Embedding

To investigate the electronic and geometrical structure of the normal and inverse spinels, embedded cluster calculations were performed. Now, three metal centers were considered combined in one cluster as a part of the bulk structure of the magnetite surrounded by pseudo potentials and point charges[214–218]. The idea of this method is to treat only a small part of the system (cluster) using quantum-mechanical (QM) methods, while rest of the bulk is approximated by a point-charge field. A schematic representation of the method is presented in Figure 63.

Centers	Functional	Relative energy [eV]	
		Normal spinel	Inverse spinel
Fe		$Fe^{2+}(T_d)[Fe^{3+}(O_h)]_2$	$Fe^{3+}(T_d)Fe^{2+}(O_h)Fe^{3+}(O_h)$
	PBE	0.00	3.95
	PBE0	0.00	2.35
	B3LYP	0.00	2.27
Fe + Mn		$Mn^{2+}(T_d)[Fe^{3+}(O_h)]_2$	$Fe^{3+}(T_d)Mn^{2+}(O_h)Fe^{3+}(O_h)$
	PBE	0.00	3.84
	PBE0	0.00	2.29
	B3LYP	0.00	2.20
Fe + Mn		$Fe^{2+}(T_d)Mn^{3+}(O_h)Fe^{3+}(O_h)$	$Fe^{3+}(T_d)Fe^{2+}(O_h)Mn^{3+}(O_h)$
	PBE	0.00	3.95
	PBE0	0.00	2.35
	B3LYP	0.00	2.27
Fe + Mn		$Fe^{2+}(T_d)Mn^{3+}(O_h)Fe^{3+}(O_h)$	$Mn^{3+}(T_d)Fe^{2+}(O_h)Fe^{3+}(O_h)$
	PBE	0.00	2.14
	PBE0	0.00	2.15
	B3LYP	0.00	2.26
Fe + Zn		$Zn^{2+}(T_d)[Fe^{3+}(O_h)]_2$	$Fe^{3+}(T_d)Zn^{2+}(O_h)Fe^{3+}(O_h)$
	PBE	0.00	3.95
	PBE0	0.00	2.42
	B3LYP	0.00	2.35
Fe + Zn + Mn		$Zn^{2+}(T_d)Mn^{3+}(O_h)Fe^{3+}(O_h)$	$Fe^{3+}(T_d)Zn^{2+}(O_h)Mn^{3+}(O_h)$
	PBE	0.00	3.95
	PBE0	0.00	2.42
	B3LYP	0.00	2.35
Fe + Zn + Mn		$Zn^{2+}(T_d)Mn^{3+}(O_h)Fe^{3+}(O_h)$	$Mn^{3+}(T_d)Zn^{2+}(O_h)Fe^{3+}(O_h)$
	PBE	0.00	2.15
	PBE0	0.00	2.23
	B3LYP	0.00	2.33

Table 6.4: Relative energies of simplified normal/inverse spinel structures combined from different small clusters calculated using three different functionals (PBE, PBE0, B3LYP)

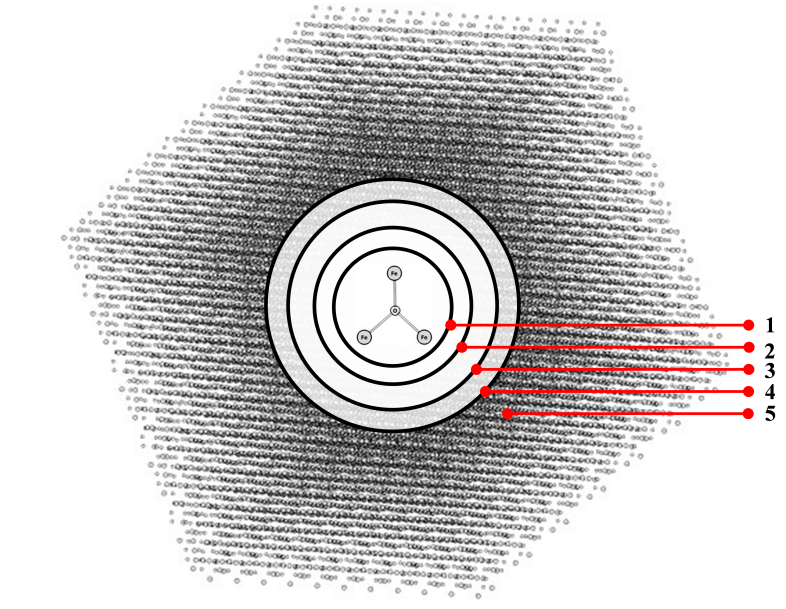

Figure 6.2: Schematic picture of the Point Charge Field Embedding method adopted in this Chapter. In the middle of the system there is the quantum cluster containing three metal centers surrounded by the first oxygen layer (1), this part is treated fully quantum mechanically, next there is a shell containing effective core potentials (ECPs) (2), and again a layer of oxygens (3), a second shell of ECPs (4), and outermost shell with point charges (5).

6.2.1 Preparation of the system

The procedure for performing embedded cluster calculations is as follows. First, a unit cell of the (111) surface of magnetite was built. Such a structure contains 48 oxygen anions, 24 iron cations on octahedral sites (half of them is divalent and half trivalent), and 12 iron cations on tetrahedral sites (all of them are trivalent), what gives 84 ions in total, Figure 6.3. The lattice parameters of the unit cell are $a = 5.934037$ Å, $b = 10.276343$ Å, and $c = 14.441501$ Å.

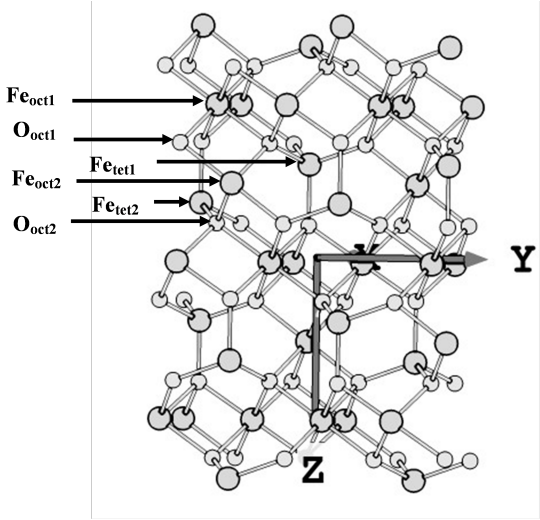

Figure 6.3: Unit cell of the (111) magnetite surface, positioned in z-direction perpendicular to the surface. Plains containing tetrahedral and octahedral iron ions are selected as Fe_{tet} and Fe_{oct} respectively. Numbers 1 and 2 denote different surrounding for atoms of the same type.

In naturally occurring crystals the dipole moment, perpendicular to the surface, is equal to zero. Such a unit cell, as in Figure 6.3, has a significant dipole moment. To get rid of the dipole moments as well as a higher multipole moments in the bulk systems one needs to extend the system until it becomes stable. In the considered case the Madelung energies of the selected atoms inside the structure were calculated, while the whole structure was extended in all directions, until the energy change from one step to another was negligible. Such an extended structure should provide the correct electric field for the QM cluster, and is used as point charge field in further calculations.

To achieve fast electrostatic convergence in the periodic system, the Evjen method was applied[219]. In this method the multipole moments of the unit cell are reduced distributing the charges of corners and face atoms to all cells they are connecting (1/8 for corners, 1/2 for faces). In order to compensate the lowest multipole moments, the Evjen procedure was extended[218–220] by addition of fractional charges at the borders of the unit cell. The full point charge field is constructed by translation of the charges in the unit cell by the lattice constants. The additional charges cancel inside the point charge field and in the end remain only at the borders of the point charge field, i.e., far from the QM cluster we are interested in. A schematic example of such a procedure of dipole moment cancellation in x-direction is presented in Figure 6.4.

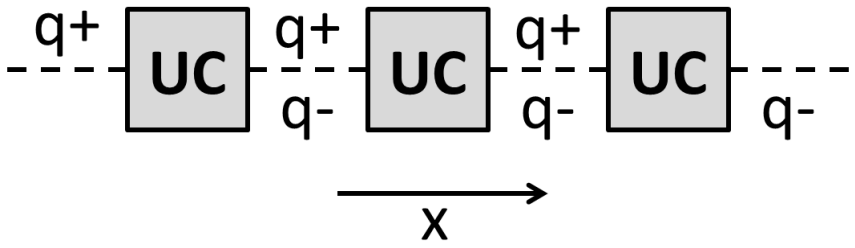

Figure 6.4: Distribution of the fractional charges within the periodic system extended in x-direction.

Here, the multipole moments were removed up to quadrupole moments. The unit cell of magnetite was extended in x, y and z direction, in a way that the point charge field has equal size in all directions. Three iron ions occupying crucial positions to create a spinel structure, one on tetrahedral and two on octahedral sites, were chosen, together with two neighboring oxygens, and their electrostatic energies were checked for different sizes of the point charge field. In Table 6.5, the size, i.e., number of ions, of the multiplied unit cell, and values of the monitored energies are given.

System size	Energy [eV]					
	Fe_{oct2}^{2+}	Fe_{tet1}^{3+}	Fe_{oct1}^{3+}	O_{oct1}^{2-}	O_{oct2}^{2-}	$O_{oct1}^{2-} - O_{oct2}^{2-}$
182	-3.4360	-5.6849	-8.2047	-2.9007	-6.1378	3.2371
1054	-0.1374	-0.0325	-0.0804	0.0627	0.0523	0.0104
6070	-3.7763	-6.6217	-7.1912	-3.4247	-3.4248	0.0002
20438	-3.7792	-6.6239	-7.1913	-3.4229	-3.4228	-0.0001
34478	-3.7793	-6.6241	-7.1915	-3.4228	-3.4227	-0.0001
72094	-3.7797	-6.6246	-7.1921	-3.4224	-3.4223	-0.0001
101158	-3.7797	-6.6247	-7.1922	-3.4224	-3.4223	-0.0001
114494	-3.7797	-6.6247	-7.1922	-3.4224	-3.4223	-0.0001
135006	-3.7798	-6.6248	-7.1923	-3.4223	-3.4222	-0.0001

Table 6.5: Energies obtained by the EVJEN procedure, for three iron centers and two oxygens, occupying different positions in the center of the structure, for the various sizes of the point charge field. The multipole moments were removed up to quadrupoles.

As the energy changes for monitored atoms became negligible for systems containing between 20438 and 34478 point charges, the latter was chosen for further investigations. In this system, the unit cell was extended 10 times in x-direction, 6 times in y-direction, and 4 times in z-direction.

6.2.2 Geometry optimization of different spinel structures

With the point charge field constructed in the presented way, and the QM cluster defined as stated in the beginning of Chapter 6.2, several embedded cluster calculations have been carried out with different oxidation states at the iron positions. Additionally, the iron atoms in the cluster were substituted by Zn and Mn to obtain ferrite structures. The substituting ions were placed in all possible positions, i.e., in O_h and T_d manifolds, respectively. For each of the clusters, a geometry optimization, followed by a validation of the stationary point with a harmonic frequency calculation, as well as a population analysis were carried out. To achieve the desired oxidation state of the metallic centers in the inner cluster, the proper number of the unpaired electrons needs to be defined. For example, if one would like to consider an inverse spinel cluster containing one Zn ion and two Fe ions, the Zn ion should be located on the octahedral site, because it can be only 2+ charged, and the total number of the unpaired electrons should be equal to 10, as there are two Fe^{3+} cations, each in its high spin configuration with 5 unpaired electrons. All considered types of clusters, i.e., the pure iron cluster and its derivatives doped with Zn and Mn atoms, as well as such in which the doping atom is represented by a pseudo potential, along with the number of the unpaired electrons are given in Table 6.6. Spins in all clusters are parallel to each other, what leads to ferromagnetic coupling.

Cluster name	Atom			Unpaired
	1(oct2)	2(tet1)	3(oct1)	electrons
Fe Fe Fe	Fe	Fe	Fe	14
Zn Fe Fe	Zn	Fe	Fe	10
Fe Zn Fe	Fe	Zn	Fe	10
Fe Fe Zn	Fe	Fe	Zn	10
Mn Fe Fe	Mn	Fe	Fe	15
Fe Mn Fe	Fe	Mn	Fe	15
Fe Fe Mn	Fe	Fe	Mn	15
Mn Fe Fe	Mn	Fe	Fe	13
Fe Mn Fe	Fe	Mn	Fe	13
Fe Fe Mn	Fe	Fe	Mn	13
Ga Fe Fe	Ga(PP)	Fe	Fe	9
Fe Ga Fe	Fe	Ga(PP)	Fe	9
Fe Fe Ga	Fe	Fe	Ga(PP)	9
Fe Ga Ga	Fe	Ga(PP)	Ga(PP)	4
Ga Fe Ga	Ga(PP)	Fe	Ga(PP)	4
Ga Ga Fe	Ga(PP)	Ga(PP)	Fe	4
Zn Fe Ga	Zn(PP)	Fe	Ga(PP)	5
Zn Ga Fe	Zn(PP)	Ga(PP)	Fe	5
Fe Zn Ga	Fe	Zn(PP)	Ga(PP)	5
Ga Zn Fe	Ga(PP)	Zn(PP)	Fe	5
Fe Ga Zn	Fe	Ga(PP)	Zn(PP)	5
Ga Fe Zn	Ga(PP)	Fe	Zn(PP)	5
Mn Fe Ga	Mn	Fe	Ga(PP)	10
Mn Ga Fe	Mn	Ga(PP)	Fe	10

Continued on next page

Table 6.6 – continued from previous page				
Cluster name	Atom			Unpaired
	1(oct2)	2(tet1)	3(oct1)	electrons
Ga Mn Fe	Ga(PP)	Mn	Fe	10
Fe Mn Ga	Fe	Mn	Ga(PP)	10
Ga Fe Mn	Ga(PP)	Fe	Mn	10
Zn Fe Mn	Zn	Fe	Mn	9
Zn Mn Fe	Zn	Mn	Fe	9
Fe Zn Mn	Fe	Zn	Mn	9
Fe Mn Zn	Fe	Mn	Zn	9
Mn Fe Zn	Mn	Fe	Zn	9
Zn Fe Ga	Zn	Fe	Ga(PP)	5
Zn Ga Fe	Zn	Ga(PP)	Fe	5
Fe Zn Ga	Fe	Zn	Ga(PP)	5
Ga Zn Fe	Ga(PP)	Zn	Fe	5
Fe Ga Zn	Fe	Ga(PP)	Zn	5
Ga Fe Zn	Ga(PP)	Fe	Zn	5

Table 6.6: Combinations of metallic centers considered in embedded cluster calculations, their names, specification on which position which atom is and the total number of unpaired electrons in the system.

For all clusters listed in Table 6.6 relative energies within the groups containing the same metallic centers, but on different positions, have been calculated. In this way, one can determine which type of spinel structure, normal or inverse, is preferred. As it can be found in Table 6.7, for all systems the inverse spinel structure is the most favorable. This is consistent with theoretical reference data included in Chapters 2.2.1 and 2.2.2, except for the cases when zinc is on the tetrahedral position. However, the differences between the inverse/normal spinel configurations are in the small range of 0.14–0.93 eV. It is also worth to underscore that an inverse spinel structure can be built in two ways, either when the 2+ ion is on the oct2 position, or when it is located on the oct1 position. The energies of those two configurations are very similar, and in our investigations they vary between 0.04 and 0.25 eV. These differences arise from slightly different environments of oct1 and oct2.

Cluster name	Unpaired electrons	Charge of the metallic center			Spinel structure	Relative energy [eV]
Fe Fe Fe	14	2.5	3	2.5	I	–
Zn Fe Fe	10	2	3	3	I	0.18
Fe Zn Fe	10	3	2	2.5	N	0.36
Fe Fe Zn	10	3	3	2	I	0.00
Mn Fe Fe	15	2	3	3	I	0.04
Fe Mn Fe	15	3	2	2.5	N	0.60
Fe Fe Mn	15	3	3	2	I	0.00

Continued on next page

Table 6.7 – continued from previous page						
Cluster name	Unpaired electrons	Charge of the metallic center			Spinel structure	Relative energy [eV]
Mn Fe Fe	13	3	3	2	I	0.00
Fe Mn Fe	13	2.5	3	2.5	I	0.38
Fe Fe Mn	13	2	3	3	I	0.12
Ga Fe Fe	9	3	3	2	I	0.18
Fe Ga Fe	9	2.5	3	2.5	I	0.00
Fe Fe Ga	9	2	3	3	I	0.33
Fe Ga Ga	4	2	3	3	I	0.25
Ga Fe Ga	4	3	2	3	N	0.93
Ga Ga Fe	4	3	3	2	I	0.00
Zn Fe Ga	5	2	3	3	I	0.19
Zn Ga Fe	5	2	3	3	I	0.00
Fe Zn Ga	5	2.5	2	3	N	0.35
Ga Zn Fe	5	3	2	2.5	N	0.14
Fe Ga Zn	5	3	3	2	I	0.13
Ga Fe Zn	5	3	3	2	I	0.03
Mn Fe Ga	10	2	3	3	I	0.17
Mn Ga Fe	10	2	3	3	I	0.08
Ga Mn Fe	10	3	2	3	N	0.57
Fe Mn Ga	10	3	2	3	N	0.73
Ga Fe Mn	10	3	3	2	I	0.00
Zn Fe Mn	9	2	3	3	I	0.19
Zn Mn Fe	9	2	3	3	I	0.81
Fe Zn Mn	9	3	2	3	N	0.48
Fe Mn Zn	9	3	3	2	I	0.60
Mn Fe Zn	9	3	3	2	I	0.00
Zn Fe Ga	5	2	3	3	I	0.23
Zn Ga Fe	5	2	3	3	I	0.36
Fe Zn Ga	5	3	2	3	N	0.53
Ga Zn Fe	5	3	2	3	N	0.46
Fe Ga Zn	5	3	3	2	I	0.26
Ga Fe Zn	5	3	3	2	I	0.00

Table 6.7: Investigated clusters with different metallic centers, their charges and spinel structures obtained in embedded cluster calculations and calculated relative energies between the clusters with the same centers. Charge of the metallic centers is defined by number of electrons in d-orbitals

In order to check what the charges on the metallic centers are, after the geometry optimization, one can perform the spin flip procedure to locate the valence electrons and take d-occupations at the metal centers from the output. For example, for the iron ion located on the tetrahedral position one can find five electrons on the alpha orbitals, and no electrons on the beta orbitals, and such occupation of the d-orbitals corresponds to the charge 3+. This methodology was used to obtain charges for other metallic center given in Table 6.7.

The interesting observation is that for the inverse spinel structures, where iron ions were located on both octahedral positions, the electrons were found to delocalize between both sites resulting in an effective charge of 2.5+ on each site, instead of the expected 2+ and 3+ charges. This phenomenon was described before in literature, both experimentally and theoretically, as mentioned in Chapter 2.2.1.

6.3 Population analysis of small clusters compared to the full system

For the small clusters, of the two metallic centers in high spin configurations (Fe and Mn) surrounded by water molecules in two different symmetries and with two different charges, presented in Chapter 6.1, the Mulliken population analysis was performed[221]. The results obtained for optimized structures are given in Table 6.8. For comparison, the atomic populations from the total density for the three metallic centers considered in the embedded cluster calculations are given in Table 6.9.

	Atomic population from total density			
	2+ (T_d)	2+ (O_h)	3+ (T_d)	3+ (O_h)
Fe atom	1.0	0.9	1.2	0.9
Cluster	2.0	2.0	3.0	3.0
Mn atom	1.2	1.0	1.1	0.8
Cluster	2.0	2.0	3.0	3.0

Table 6.8: Mulliken atomic population from the total density of small metallic clusters surrounded by water molecules in two different symmetries and with two different charges, comparison of data for metal centers and entire clusters.

Comparing the results of population analyses for the small and large models, Tables 6.8 and 6.9, one can see that in general the total charge does not only arise from the metallic centers, but also from the atoms in the surrounding. This is clearly visible in Table 6.8 where charges for the entire small clusters are given as well, and in fact they correspond to the desired charges. In Table 6.8 we see that there is no clear difference between triply and doubly charged ions, in the end all metallic centers have similar charges of around 1+. One can notice only slightly lower charges on the metallic centers for the octahedral structures, but still it is not possible to distinguish between 2+ and 3+. For the big clusters and their atomic populations stored in Table 6.9 the situation is slightly different. Again, the charges of the metallic centers do not resemble the expected charge, but in most cases the lowest charge is present on the tetrahedral positions. However, as it was shown in the analysis of the occupation numbers of the orbitals localized on the metallic centers in Chapter 6.2.2, the inverse spinel structure is dominating. In such a structure, the 3+ ion is placed on the tetrahedral position. Even for a zinc-doped structure, which is a closed-shell system, and can only have 2+ charge, the results are ambiguous, and depending on the position in the cluster it has three different charges in a range from 1.2 to 2.4. These results show that to tell what charge is on which metallic center, a population analysis is not reliable, and a check of the occupation numbers is helpful.

	Atomic population from total density					
Unpaired electrons				14		
oct2	Fe	1.8				
tet1	Fe	1.3				
oct1	Fe	2.0				
Unpaired electrons				15		
oct2	Mn	1.7	Fe	1.9	Fe	1.9
tet1	Fe	1.3	Mn	1.0	Fe	1.3
oct1	Fe	2.0	Fe	2.1	Mn	1.9
Unpaired electrons				13		
oct2	Mn	2.2	Fe	1.8	Fe	1.7
tet1	Fe	1.2	Mn	1.3	Fe	1.2
oct1	Fe	1.9	Fe	2.0	Mn	2.3
Unpaired electrons				10		
oct2	Zn	2.0	Fe	1.9	Fe	1.8
tet1	Fe	1.2	Zn	1.2	Fe	1.2
oct1	Fe	2.0	Fe	2.0	Zn	2.4

Table 6.9: Mulliken atomic population of big clusters containing three metallic centers in different spinel structures, comparison of data for metal centers and entire clusters.

In the next step, the number of the unpaired electrons, obtained from the spin density, i.e., difference between the densities obtained from alpha and beta orbitals, for each of the small and big clusters was calculated.

	Unpaired electrons from $D_\alpha - D_\beta$			
	2+ (T_d)	2+ (O_h)	3+ (T_d)	3+ (O_h)
Unpaired electrons	4	4	5	5
Fe atom	3.8	3.8	4.2	4.2
Cluster	4.0	4.0	5.0	5.0
Unpaired electrons	5	5	4	4
Mn atom	4.9	4.9	3.9	3.8
Cluster	5.0	4.9	4.0	4.0

Table 6.10: Unpaired electrons and their localization on metallic centers and total number for the whole small clusters, surrounded with water molecules, containing both Fe and Mn.

As shown in Table 6.10, in case of the small clusters, most of the unpaired electrons are found on the metallic centers, especially for the Mn clusters, however there is still some delocalization of the unpaired electrons to the water molecules. For the clusters containing Fe^{3+}, the unpaired electrons are little more distributed over whole cluster, than for the Fe^{2+} case, regardless of the symmetry of the cluster and number of water molecules.

In the case of the point-charge field embedded systems, presented in Table 6.11, we can

	Unpaired electrons from D_α–D_β)					
Total no. of unpaired el.				14		
oct2	Fe	3.9				
tet1	Fe	4.0				
oct1	Fe	3.9				
Cluster		13.8				
Total no. of unpaired el.				15		
oct2	Mn	4.8	Fe	4.0	Fe	4.1
tet1	Fe	4.1	Mn	4.8	Fe	4.1
oct1	Fe	4.0	Fe	4.0	Mn	4.8
Cluster		14.6		14.5		14.7
Total no. of unpaired el.				13		
oct2	Mn	3.9	Fe	3.9	Fe	3.9
tet1	Fe	3.9	Mn	3.9	Fe	4.0
oct1	Fe	3.9	Fe	3.9	Mn	3.9
Cluster		13.0		13.0		13.0
Total no. of unpaired el.				10		
oct2	Zn	–	Fe	4.0	Fe	4.1
tet1	Fe	4.1	Zn	–	Fe	4.0
oct1	Fe	4.0	Fe	4.0	Zn	–
Cluster		9.6		9.4		9.7

Table 6.11: Distribution of unpaired electrons through the metallic centers and their total number in the big clusters, clusters contain different mixtures of Fe^{2+}/Fe^{3+} ions with Mn^{2+}/Mn^{3+} and Zn^{2+}.

see that usually one or two unpaired electrons are distributed over the surrounding of the metal centers. Additionally, the number of the unpaired electrons on the iron centers is equally distributed over all of them, and it is always around 4, despite the fact that usually there is at least one Fe^{3+} cation present in the cluster, which is supposed to have 5 unpaired electrons. This observation is consistent with the one obtained for the small clusters, where on the Fe^{3+} cation one could find 4 unpaired electrons, instead of the expected 5. Also, the number of missing unpaired electrons for the big iron clusters corresponds to the number of Fe^{3+} cations in the structure. This suggests that the lack of the unpaired electrons in the three-iron-center clusters is due to the presence of the Fe^{3+} cations.

6.4 Summary

In this chapter, quantum-chemical calculations employing DFT methods were carried out. These calculations provide information on the electronic structure of magnetite, which can be directly related to other experimental and theoretical observations. Here, several model structures were proposed. First, small one-center clusters with water for bi- and trivalent cations of Fe, Mn, and Zn were investigated. Next, using a unit cell of magnetite, a three-center cluster embedded in a point-charge field was prepared. The main issue present in the considerations of magnetite is type of the spinel structure present in the system. The assignment of spinel type is not straightforward, as depending on the theoretical approach either inverse or normal spinel is preferred. Additionally, experimental reports show that instead of distinguished 2+ and 3+ iron centers, rather two 2.5+ centers are observed. This, specific for iron, distribution of charges was also observed in the calculations performed for big three-center point-charge field embedded cluster. It was also noticed that for clusters containing Fe^{3+} cations, roughly one unpaired electron per Fe^{3+} center is delocalized over the cluster. This effect could be caused by the application of a GGA functional, namely PBE. Therefore, using the PBE structure of the Fe Fe Fe cluster, single-point calculation with a hybrid PBE0 functional was performed. This, however, did not influence the resulting charge distribution. Also, small changes in the geometry, i.e., enlarging or shortening of the Fe−O distances, did not change this distribution. This suggests that the electronic structure of magnetite might be difficult to describe with conventional DFT methods, and possibly some other QM approaches should be applied.

7 Summary

In this thesis, the interactions of peptides and inorganic surfaces were investigated theoretically. Binding selectivity of different peptide sequences to inorganic surfaces or nanoparticles is an important problem in various areas of science and technology, like, biotechnology or biomedical engineering. Experimental methods can be used to screen a certain amount of sequences, and verify which of them are binding or not. However, this might be difficult and time consuming, and also provide no information about the nature of interaction, thus give no hint for rational design of peptides binding to surfaces. Here, theoretical methods are invaluable, as they can support the experimental methods, and give insight into the interaction itself. Nevertheless, there are several challenges. First, there is an enormous number of possible combinations of amino acids building peptides and proteins. Second, the consideration of all important aspects of the experimental conditions, such as, certain solvents and buffers is crucial. Next, the modeling of the surface, due to its complicated structure, may be difficult to represent in the computational model. Furthermore, often in the case of the nanoparticles, its actual structure is unknown and condition-dependent.

To address all of these challenges, an efficient computational protocol for evaluation of the binding affinity between peptides and surfaces was introduced in this thesis. We have developed a computational protocol called Effective Implicit Surface Model (EISM). This model is based on Monte Carlo calculations, supported by metadynamics using force-field methods to describe the system. In this model, the surface is treated implicitly and the required empirical amino acid-surface binding affinities can be taken both from experiment and theory.

In order to validate the EISM model, we have calibrated its parameters, using available literature values of theoretically obtained binding affinities for single amino acids, both for gold (111) and silver (111) surfaces. This enables us to define the binding affinities for gold- and silver-binding peptides with various sequences, and to calculate the Gibbs free energy of peptide-surface interactions. The calculated Gibbs free energy was compared with the experimental data available in literature with the overall result showing that we are able to distinguish between better and worse binding sequences. In the set of gold-binding and silver-binding peptides, all peptides were manifesting a stronger affinity to the gold surface, except for one sequence, which was binding stronger to the silver surface. These results are consistent with experimental findings.

The next task was to analyze and explain the results of peptide array screening experiments performed by our experimental collaborators. In this experiment, the interaction strength between homopeptide sequences of all amino acids stored on a cellulose membrane to magnetite nanoparticles under various buffer- and pH-conditions was investigated. Based on these results, we proposed a model which allows to understand the obtained results and to predict binding for other buffer-conditions. What we found was that the binding is observed almost exclusively for charged peptides. Another observation was, that in case the buffer species are charged oppositely compared to the peptide, the peptide-nanoparticle binding is not direct, but with the mediation of buffer ions. Moreover, the binding of both

the buffer and the peptide to the surface was found to be pH dependent. The agreement of the results predicted for charged peptides with experimental scores was very good. This suggests that the proposed model is a useful tool for analysis and to some extent can be used to predict the binding strength of the peptides.

In the next part, the EISM model was calibrated and validated against results of the peptide array screening experiment. For this purpose, a new membrane, containing sequences of D-peptides with different length and mutated systematically by three other amino acids (C, G and N) was designed. First, the EISM model was parametrized using experimental data from the first membrane for the homopeptides of all amino acids. Next the Gibbs free energies of binding for the peptides from the second membrane were calculated and compared to the experimental scores. This gave a good agreement. A more detailed analysis, so-called clustering, was also performed to have an insight into binding behavior of individual residues. Knowing which residues are close to the surface, for the peptides with unexpected low or high Gibbs free energy value, gave an answer how flexibility of the peptide chain influences the binding abilities.

Additional investigations using the EISM model were performed to check how the positions of the amino acids in the sequence and change of the length of the peptide, affect the Gibbs free energy of binding. We have noticed that systematic changes in the sequence will not guarantee linear changes of the Gibbs free energy values. This clearly indicates that not only the composition, but also the position of the amino acids in the sequence determines the binding strength. This knowledge can be helpful in future design of sequences binding well to the desired surface.

Since magnetite is the main component of the iron oxide magetic nanoparticles considered in this work, a deeper theoretical analysis for this compound was carried out. Therefore, in the last part of the thesis, quantum-chemical calculations using density functional theory (DFT) were employed to investigate the electronic properties of magnetite and its derivative mixed-center clusters. The main issue present in the considerations of magnetite is the type of the spinel structure present in the system. The assignment of the spinel type is not straightforward, as depending on the theoretical approach either inverse or normal spinel is preferred. Additionally, experimental reports show that instead of distinguished '2+' and '3+' iron centers, rather two '2.5+' centers are observed. To investigate this problem, first, small one-center clusters with water for bi- and trivalent cations of Fe, Mn, and Zn were considered. These simple one-center models were, however, not enough to describe the spinel structure of magnetite. Therefore, out of a unit cell of the magnetite, a three-center cluster embedded in a point-charge field, was prepared. Also in these calculations, the specific distribution of charges was analyzed. It was also noticed that for clusters containing Fe^{3+} cations, roughly one unpaired electron per Fe^{3+} center is pulled out from the metal center, leading to effectively fewer unpaired electrons than expected.

In this thesis, several theoretical methods for investigating interactions of peptides and inorganic surfaces, as well as the bare iron surfaces, were introduced and employed. The EISM model-based Monte Carlo (MC) protocol introduced in this thesis appears to be much more efficient than the usual molecular dynamics (MD) approach, opening a new perspective for investigating a large number of different sequences and analyzing whether and how the mutations, the length, and a particular position of a certain amino acid in the peptide sequence are crucial for binding abilities. Such an efficient computational protocol paves a route towards rational design of new peptide sequences manifesting desired properties. Due to its empirical nature in can be quickly calibrated against desired experimental

conditions. Moreover, all properties of the surface with respect to the interaction with peptides are stored in the calibration parameters γ_i, which is a very efficient way of treating more complicated cases. More advanced quantum-chemical calculations showed that the electronic structure of iron-oxide nanoparticles is complicated. All in all, the efficient and simple model, still providing a good accuracy, appears to be a good compromise in this case.

Bibliography

[1] Seker, U. O. S. and Demir, H. V., *Molecules*, 2011, **16**(2), 1426–1451.

[2] Sarikaya, M.; Tamerler, C.; Jen, A. K.-Y.; Schulten, K. and Baneyx, F., *Nat. Mater.*, 2003, **2**(9), 577–585.

[3] Tamerler, C. and Sarikaya, M., *Acta Biomater.*, 2007, **3**(3), 289–299.

[4] Green, J. J.; Chiu, E.; Leshchiner, E. S.; Shi, J.; Langer, R. and Anderson, D. G., *Nano Lett.*, 2007, **7**(4), 874–879.

[5] Delehanty, J. B.; Boeneman, K.; Bradburne, C. E.; Robertson, K.; Bongard, J. E. and Medintz, I. L., *Therapeutic Delivery*, 2010, **1**(3), 411–433.

[6] Devadasu, V. R.; Bhardwaj, V. and Kumar, M. N. V. R., *Chem. Rev.*, 2013, **113**(3), 1686–1735.

[7] Durán, J. D. G.; Arias, J. L.; Gallardo, V. and Delgado, A. V., *J. Pharm. Sci.*, 2008, **97**(8), 2948–2983.

[8] Arruebo, M.; Fernández-Pacheco, R.; Ibarra, M. R. and Santamaría, J., *Nano Today*, 2007, **2**(3), 22–32.

[9] Amstad, E.; Textor, M. and Reimhult, E., *Nanoscale*, 2011, **3**(7), 2819–2843.

[10] Hasenpusch, G.; Geiger, J.; Wagner, K.; Mykhaylyk, O.; Wiekhorst, F.; Trahms, L.; Heidsieck, A.; Gleich, B.; Bergemann, C.; Aneja, M. K. and Rudolph, C., *Pharm. Res.*, 2012, **29**(5), 1308–1318.

[11] Talelli, M.; Rijcken, C. J. F.; Lammers, T.; Seevinck, P. R.; Storm, G.; van Nostrum, C. F. and Hennink, W. E., *Langmuir*, 2009, **25**(4), 2060–2067.

[12] Mahmoudi, M.; Sant, S.; Wang, B.; Laurent, S. and Sen, T., *Adv. Drug Delivery Rev.*, 2011, **63**(1–2), 24–46.

[13] Villee, C. A. J., *N. Engl. J. Med.*, 1983, **309**(4), 247–248.

[14] Rodriguez, D. E.; Thula-Mata, T.; Toro, E. J.; Yeh, Y.-W.; Holt, C.; Holliday, L. S. and Gower, L. B., *Acta Biomater.*, 2014, **10**(1).

[15] Nudelman, F.; Pieterse, K.; George, A.; Bomans, P. H. H.; Friedrich, H.; Brylka, L. J.; Hilbers, P. A. J.; de With, G. and Sommerdijk, N. A. J. M., *Nat. Mater.*, 2010, **9**(12), 1004–1009.

[16] Burg, K. J.; Porter, S. and Kellam, J. F., *Biomaterials*, 2000, **21**(23), 2347–2359.

[17] Boehler, R. M.; Graham, J. G. and Shea, L. D., *BioTechniques*, 2011, **51**(4), 239–passim.

[18] Banerjee, I.; Pangule, R. C. and Kane, R. S., *Adv. Mater.*, 2011, **23**(6), 690–718.

[19] Costerton, J. W.; Stewart, P. S. and Greenberg, E. P., *Science*, 1999, **284**(5418), 1318–1322.

[20] Brown, S.; Sarikaya, M. and Johnson, E., *Journal of Mol. Biol.*, 2000, **299**(3), 725–735.

[21] Fu, X.; Wang, Y.; Huang, L.; Sha, Y.; Gui, L.; Lai, L. and Tang, Y., *Adv. Mater.*, 2003, **15**(11), 902–906.

[22] Slocik, J. M. and Naik, R. R., *Adv. Mater.*, 2006, **18**(15), 1988–1992.

[23] Grohe, B.; O'Young, J.; Ionescu, D. A.; Lajoie, G.; Rogers, K. A.; Karttunen, M.; Goldberg, H. A. and Hunter, G. K., *J. Am. Chem. Soc.*, 2007, **129**(48), 14946–14951.

[24] Naik, R. R.; Jones, S. E.; Murray, C. J.; McAuliffe, J. C.; Vaia, R. A. and Stone, M. O., *Adv. Funct. Mater.*, 2004, **14**(1), 25–30.

[25] Slocik, J.; Stone, M. and Naik, R., *Small*, 2005, **1**(11), 1048–1052.

[26] Gray, J. J., *Curr. Opin. Struct. Biol.*, 2004, **14**(1), 110–115.

[27] Gupta, A. K. and Gupta, M., *Biomaterials*, 2005, **26**(18), 3995–4021.

[28] Lévy, R.; Thanh, N. T. K.; Doty, R. C.; Hussain, I.; Nichols, R. J.; Schiffrin, D. J.; Brust, M. and Fernig, D. G., *J. Am. Chem. Soc.*, 2004, **126**(32), 10076–10084.

[29] Lu, A.-H.; Salabas, E. L. and Schüth, F., *Angew. Chem. Int. Ed.*, 2007, **46**(8), 1222–1244.

[30] Wu, W.; Wu, Z.; Yu, T.; Jiang, C. and Kim, W.-S., *Sci. Technol. Adv. Mater.*, 2015, **16**(2), 023501.

[31] Wu, W.; He, Q. and Jiang, C., *Nanoscale Res. Lett.*, 2008, **3**(11), 397–415.

[32] Laurent, S.; Forge, D.; Port, M.; Roch, A.; Robic, C.; Vander Elst, L. and Muller, R. N., *Chem. Rev.*, 2008, **108**(6), 2064–2110.

[33] Hao, R.; Xing, R.; Xu, Z.; Hou, Y.; Gao, S. and Sun, S., *Adv. Mater.*, 2010, **22**(25), 2729–2742.

[34] Miserez, A.; Weaver, J. C.; Thurner, P. J.; Aizenberg, J.; Dauphin, Y.; Fratzl, P.; Morse, D. E. and Zok, F. W., *Adv. Funct. Mater.*, 2008, **18**(8), 1241–1248.

[35] Hlady, V. and Buijs, J., *Curr. Opin. Biotechnol.*, 1996, **7**(1), 72–77.

[36] Brash, J. L. and Horbett, T. A. In *Proteins at Interfaces II*, Vol. 602 of *ACS Symposium Series;* American Chemical Society, 1995; pages 1–23.

[37] Aizenberg, J.; Weaver, J. C.; Thanawala, M. S.; Sundar, V. C.; Morse, D. E. and Fratzl, P., *Science*, 2005, **309**(5732), 275–278.

[38] Waite, J. H. and Tanzer, M. L., *Science*, 1981, **212**(4498), 1038–1040.

[39] Lee, H.; Lee, B. P. and Messersmith, P. B., *Nature*, 2007, **448**(7151), 338–341.

[40] Lee, H.; Rho, J. and Messersmith, P. B., *Adv. Mater. (Deerfield Beach, Fla.)*, 2009, **21**(4), 431–434.

[41] Waite, J. H.; Andersen, N. H.; Jewhurst, S. and Sun, C., *J. Adhes.*, 2005, **81**(3-4), 297–317.

[42] Lee, H.; Dellatore, S. M.; Miller, W. M. and Messersmith, P. B., *Science*, 2007, **318**(5849), 426–430.

[43] Shalev, T.; Gopin, A.; Bauer, M.; Stark, R. W. and Rahimipour, S., *J. Mater. Chem.*, 2012, **22**(5), 2026–2032.

[44] Lee, H.; Scherer, N. F. and Messersmith, P. B., *Proc. Natl. Acad. Sci. U.S.A.*, 2006, **103**(35), 12999–13003.

[45] Wegner, G. J.; Lee, H. J. and Corn, R. M., *Anal. Chem.*, 2002, **74**(20), 5161–5168.

[46] Chen, J.; Wiley, B. J. and Xia, Y., *Langmuir*, 2007, **23**(8), 4120–4129.

[47] Slocik, J. M.; Tam, F.; Halas, N. J. and Naik, R. R., *Nano Lett.*, 2007, **7**(4), 1054–1058.

[48] Willett, R. L.; Baldwin, K. W.; West, K. W. and Pfeiffer, L. N., *Proc. Natl. Acad. Sci. U.S.A.*, 2005, **102**(22), 7817–7822.

[49] Whaley, S. R.; English, D. S.; Hu, E. L.; Barbara, P. F. and Belcher, A. M., *Nature*, 2000, **405**(6787), 665–668.

[50] Tamerler, C.; Oren, E. E.; Duman, M.; Venkatasubramanian, E. and Sarikaya, M., *Langmuir*, 2006, **22**(18), 7712–7718.

[51] Speight, R. E. and Cooper, M. A., *J. Mol. Recognit.*, 2012, **25**(9), 451–473.

[52] Chen, H.; Su, X.; Neoh, K.-G. and Choe, W.-S., *Langmuir*, 2009, **25**(3), 1588–1593.

[53] Sano, K.-I.; Sasaki, H. and Shiba, K., *J. Am. Chem. Soc.*, 2006, **128**(5), 1717–1722.

[54] Wei, Y. and Latour, R. A., *Langmuir*, 2010, **26**(24), 18852–18861.

[55] Wei, Y. and Latour, R. A., *Langmuir*, 2008, **24**(13), 6721–6729.

[56] Hnilova, M.; Oren, E. E.; Seker, U. O. S.; Wilson, B. R.; Collino, S.; Evans, J. S.; Tamerler, C. and Sarikaya, M., *Langmuir*, 2008, **24**(21), 12440–12445.

[57] Florin, E. L.; Moy, V. T. and Gaub, H. E., *Science*, 1994, **264**(5157), 415–417.

[58] Berquand, A.; Xia, N.; Castner, D. G.; Clare, B. H.; Abbott, N. L.; Dupres, V.; Adriaensen, Y. and Dufrêne, Y. F., *Langmuir*, 2005, **21**(12), 5517–5523.

[59] Carvalho, F. A.; Martins, I. C. and Santos, N. C., *Arch. Biochem. Biophys.*, 2013, **531**(1–2), 116–127.

[60] Carvalho, F. A. and Santos, N. C., *IUBMB Life*, 2012, **64**(6), 465–472.

[61] Hinterdorfer, P.; Baumgartner, W.; Gruber, H. J.; Schilcher, K. and Schindler, H., *Proc. Natl. Acad. Sci. U.S.A.*, 1996, **93**(8), 3477–3481.

[62] Maity, S.; Zanuy, D.; Razvag, Y.; Das, P.; Alemán, C. and Reches, M., *Phys. Chem. Chem. Phys.*, 2015, **17**(23), 15305–15315.

[63] Grandbois, M.; Beyer, M.; Rief, M.; Clausen-Schaumann, H. and Gaub, H. E., *Science*, 1999, **283**(5408), 1727–1730.

[64] Wang, C. and Yadavalli, V. K., *Micron*, 2014, **60**, 5–17.

[65] Galler, K.; Bräutigam, K.; Große, C.; Popp, J. and Neugebauer, U., *Analyst*, 2014, **139**(6), 1237–1273.

[66] Das, P. and Reches, M., *Biopolymers*, 2015, **104**(5), 480–494.

[67] Lee, G. U.; Kidwell, D. A. and Colton, R. J., *Langmuir*, 1994, **10**(2), 354–357.

[68] Ozboyaci, M.; Kokh, D. B.; Corni, S. and Wade, R. C., *Q. Rev. Biophys.*, 2016, **49**, e4.

[69] Alder, B. J. and Wainwright, T. E., *J. Chem. Phys.*, 1959, **31**(2), 459–466.

[70] CASE, D. A.; CHEATHAM, T. E.; DARDEN, T.; GOHLKE, H.; LUO, R.; MERZ, K. M.; ONUFRIEV, A.; SIMMERLING, C.; WANG, B. and WOODS, R. J., *J. Comput. Chem.*, 2005, **26**(16), 1668–1688.

[71] Rahman, A., *Phys. Rev.*, 1964, **136**(2A), A405–A411.

[72] Nawrocki, G. and Cieplak, M., *Phys. Chem. Chem. Phys.*, 2013, **15**(32), 13628.

[73] Vellore, N. A.; Yancey, J. A.; Collier, G.; Latour, R. A. and Stuart, S. J., *Langmuir*, 2010, **26**(10), 7396–7404.

[74] Kästner, J. and Thiel, W., *J. Chem. Phys.*, 2005, **123**(14), 144104.

[75] Sun, Y.; Dominy, B. N. and Latour, R. A., *J. Comput. Chem.*, 2007, **28**(11), 1883–1892.

[76] Yancey, J. A.; Vellore, N. A.; Collier, G.; Stuart, S. J. and Latour, R. A., *Biointerphases*, 2010, **5**(3), 85–95.

[77] Souaille, M. and Roux, B., *Comput. Phys. Commun.*, 2001, **135**(1), 40–57.

[78] Schneider, J. and Ciacchi, L. C., *Surf. Sci.*, 2010, **604**(13–14), 1105–1115.

[79] O'Brien, C. P.; Stuart, S. J.; Bruce, D. A. and Latour, R. A., *Langmuir*, 2008, **24**(24), 14115–14124.

[80] Torrie, G. M. and Valleau, J. P., *J. Comput. Phys.*, 1977, **23**(2), 187–199.

[81] Boughton, A. P.; Andricioaei, I. and Chen, Z., *Langmuir*, 2010, **26**(20), 16031–16036.

[82] Kumar, S.; Rosenberg, J. M.; Bouzida, D.; Swendsen, R. H. and Kollman, P. A., *J. Comput. Chem.*, 1992, **13**(8), 1011–1021.

[83] Juffer, A. H.; Argos, P. and de Vlieg, J., *J. Comput. Chem.*, 1996, **17**(16), 1783–1803.

[84] Hoefling, M.; Iori, F.; Corni, S. and Gottschalk, K.-E., *Langmuir*, 2010, **26**(11), 8347–8351.

[85] Friddle, R. W.; Battle, K.; Trubetskoy, V.; Tao, J.; Salter, E. A.; Moradian-Oldak, J.; De Yoreo, J. J. and Wierzbicki, A., *Angew. Chem. Int. Ed.*, 2011, **50**(33), 7541–7545.

[86] Yang, Z. and Zhao, Y.-P., *Eng. Anal. Boundary Elem.*, 2007, **31**(5), 402–409.

[87] Chen, Q.; Wang, Q.; Liu, Y.-C.; Wu, T.; Kang, Y.; Moore, J. D. and Gubbins, K. E., *J. Chem. Phys.*, 2009, **131**(1), 015101.

[88] Mijajlovic, M.; Penna, M. J. and Biggs, M. J., *Langmuir*, 2013, **29**(9), 2919–2926.

[89] Alvarez-Paggi, D.; Martín, D. F.; DeBiase, P. M.; Hildebrandt, P.; Martí, M. A. and Murgida, D. H., *J. Am. Chem. Soc.*, 2010, **132**(16), 5769–5778.

[90] Mücksch, C. and Urbassek, H. M., *Langmuir*, 2011, **27**(21), 12938–12943.

[91] Utesch, T.; Daminelli, G. and Mroginski, M. A., *Langmuir*, 2011, **27**(21), 13144–13153.

[92] Horinek, D.; Serr, A.; Bonthuis, D. J.; Boström, M.; Kunz, W. and Netz, R. R., *Langmuir*, 2008, **24**(4), 1271–1283.

[93] Shen, J.-W.; Wu, T.; Wang, Q. and Pan, H.-H., *Biomaterials*, 2008, **29**(5), 513–532.

[94] Kang, Y.; Liu, Y.-C.; Wang, Q.; Shen, J.-W.; Wu, T. and Guan, W.-J., *Biomaterials*, 2009, **30**(14), 2807–2815.

[95] Emami, F. S.; Puddu, V.; Berry, R. J.; Varshney, V.; Patwardhan, S. V.; Perry, C. C. and Heinz, H., *Chem. Mater.*, 2014, **26**(19), 5725–5734.

[96] Hamdi, M.; Ferreira, A.; Sharma, G. and Mavroidis, C., *Microelectron. J.*, 2008, **39**(2), 190–201.

[97] Baier, J.; Blumenstein, N. J.; Preusker, J.; Jeurgens, L. P. H.; Welzel, U.; Do, T. A.; Pleiss, J. and Bill, J., *CrystEngComm*, 2014, **16**(24), 5301.

[98] Friedrichs, W.; Köppen, S. and Langel, W., *Surf. Sci.*, 2013, **617**, 42–52.

[99] Dong, X.; Wang, Q.; Wu, T. and Pan, H., *Biophys. J.*, 2007, **93**(3), 750–759.

[100] Laio, A. and Parrinello, M., *Proc. Natl. Acad. Sci. U.S.A.*, 2002, **99**(20), 12562–12566.

[101] Bussi, G.; Laio, A. and Parrinello, M., *Phys. Rev. Lett.*, 2006, **96**(9), 090601.

[102] Bussi, G.; Gervasio, F. L.; Laio, A. and Parrinello, M., *J. Am. Chem. Soc.*, 2006, **128**(41), 13435–13441.

[103] Laio, A. and Gervasio, F. L., *Rep. Prog. Phys.*, 2008, **71**(12), 126601.

[104] Jarzynski, C., *Phys. Rev. Lett.*, 1997, **78**(14), 2690–2693.

[105] Bonomi, M.; Barducci, A. and Parrinello, M., *J. Comput. Chem.*, 2009, **30**(11), 1615–1621.

[106] Vallee, A.; Humblot, V. and Pradier, C.-M., *Acc. Chem. Res.*, 2010, **43**(10), 1297–1306.

[107] Lambert, J.-F., *Orig. Life and Evolution of Biospheres*, 2008, **38**(3), 211–242.

[108] Collins, J. R.; Loew, G. H.; Luke, B. T. and White, D. H., *Origins Life Evol. Biosphere: Journal of the International Society for the Study of the Origin of Life*, 1988, **18**(1-2), 107–119.

[109] Qiu, T. and Barteau, M. A., *J. Colloid Interface Sci.*, 2006, **303**(1), 229–235.

[110] Lodish, H.; Berk, A.; Zipursky, S. L.; Matsudaira, P.; Baltimore, D. and Darnell, J., W. H. Freeman, New York, 2000; chapter Noncovalent Bonds.

[111] Schwaminger, S. P.; García, P. F.; Merck, G. K.; Bodensteiner, F. A.; Heissler, S.; Günther, S. and Berensmeier, S., *J. Phys. Chem. C*, 2015, **119**(40), 23032–23041.

[112] Roddick-Lanzilotta, A. D.; Connor, P. A. and McQuillan, A. J., *Langmuir*, 1998, **14**(22), 6479–6484.

[113] Arunan, E.; Desiraju, G. R.; Klein, R. A.; Sadlej, J.; Scheiner, S.; Alkorta, I.; Clary, D. C.; Crabtree, R. H.; Dannenberg, J. J.; Hobza, P. and others, , *Pure Appl. Chem.*, 2011, **83**(8), 1637–1641.

[114] Ikhsan, J.; Johnson, B. B.; Wells, J. D. and Angove, M. J., *J. Colloid Interface Sci.*, 2004, **273**(1), 1–5.

[115] Vlasova, N. N. and Golovkova, L. P., *Colloid J.*, 2004, **66**(6), 657–662.

[116] Munsch, S.; Hartmann, M. and Ernst, S., *Chem. Commun.*, 2001, pages 1978–1979.

[117] Hitz, T. and Luisi, P., *Helv. Chim. Acta*, 2002, **85**(11), 3975–3983.

[118] Basyuk, V. A., *Theor. Exp. Chem.*, 1990, **26**(1), 89–93.

[119] Krohn, J. E. and Tsapatsis, M., *Langmuir*, 2005, **21**(19), 8743–8750.

[120] Krohn, J. E. and Tsapatsis, M., *Langmuir*, 2006, **22**(22), 9350–9356.

[121] Hargrove, R. S. and Kündig, W., *Solid State Commun.*, 1970, **8**(5), 303–308.

[122] Navrotsky, A., *Am. Mineral.*, 1986, **71**(9-10), 1160–1169.

[123] Essene, E. J. and Peacor, D. R., *Am. Mineral.*, 1983, **68**(3-4), 449–455.

[124] O'Neill, H. S. C. and Dollase, W. A., *Phys. Chem. Miner.*, 1994, **20**(8), 541–555.

[125] Spaldin, N. A., *Magnetic materials: fundamentals and applications*, Cambridge University Press, Cambridge ; New York, 2nd ed ed., 2011.

[126] Wyckoff, R. W. G. and Wyckoff, R. W. G., *Inorganic compounds RXn, RnMX2, RnMX3*, number Ralph W. G. Wyckoff ; Vol. 2 in Crystal structures, Interscience Publ, New York, NY, 2. ed ed., 1964.

[127] Noh, J.; Osman, O. I.; Aziz, S. G.; Winget, P. and Brédas, J.-L., *Sci. Technol. Adv. Mater.*, 2014, **15**(4), 044202.

[128] Figuerola, A.; Di Corato, R.; Manna, L. and Pellegrino, T., *Pharmacol. Res.*, 2010, **62**(2), 126–143.

[129] Tiwari, P. M.; Vig, K.; Dennis, V. A. and Singh, S. R., *Nanomaterials*, 2011, **1**(1), 31–63.

[130] Yamaura, M.; Camilo, R. L.; Sampaio, L. C.; Macêdo, M. A.; Nakamura, M. and Toma, H. E., *J. Magn. Magn. Mater.*, 2004, **279**(2–3), 210–217.

[131] Okuda, M.; Eloi, J.-C.; Jones, S. E. W.; Sarua, A.; Richardson, R. M. and Walther Schwarzacher, , *Nanotechnology*, 2012, **23**(41), 415601.

[132] Cao, M.; Li, Z.; Wang, J.; Ge, W.; Yue, T.; Li, R.; Colvin, V. L. and Yu, W. W., *Trends in Food Science & Technology*, 2012, **27**(1), 47–56.

[133] Xie, J.; Wang, J.; Niu, G.; Huang, J.; Chen, K.; Li, X. and Chen, X., *Chem. Commun.*, 2010, **46**(3), 433–435.

[134] Iwaki, Y.; Kawasaki, H. and Arakawa, R., *Anal. Sci.*, 2012, **28**(9), 893–900.

[135] Marcelo, G.; Muñoz-Bonilla, A.; Rodríguez-Hernández, J. and Fernández-García, M., *Polym. Chem.*, 2013, **4**(3), 558–567.

[136] Samanta, B.; Yan, H.; Fischer, N. O.; Shi, J.; Jerry, D. J. and Rotello, V. M., *J. Mater. Chem.*, 2008, **18**(11), 1204.

[137] Yang, L.; Cao, Z.; Sajja, H. K.; Mao, H.; Wang, L.; Geng, H.; Xu, H.; Jiang, T.; Wood, W. C.; Nie, S. and Wang, Y. A., *J. Biomed. Nanotechnol.*, 2008, **4**(4), 439–449.

[138] Lee, N. and Hyeon, T., *Chem. Soc. Rev.*, 2012, **41**(7), 2575–2589.

[139] Chow, A. M.; Chan, K. W. Y.; Cheung, J. S. and Wu, E. X., *Magn. Reson. Med.*, 2010, **63**(1), 224–229.

[140] Tsai, Z.-T.; Wang, J.-F.; Kuo, H.-Y.; Shen, C.-R.; Wang, J.-J. and Yen, T.-C., *J. Magn. Magn. Mater.*, 2010, **322**(2), 208–213.

[141] Yue-Jian, C.; juan, T.; Fei, X.; Jia-Bi, Z.; Ning, G.; Yi-Hua, Z.; Ye, D. and Liang, G., *Drug Dev. Ind. Pharm.*, 2010, **36**(10), 1235–1244.

[142] Terreno, E.; Castelli, D. D.; Viale, A. and Aime, S., *Chem. Rev.*, 2010, **110**(5), 3019–3042.

[143] Gilchrist, R. K.; Medal, R.; Shorey, W. D.; Hanselman, R. C.; Parrott, J. C. and Taylor, C. B., *Ann. Surg.*, 1957, **146**(4), 596–606.

[144] Laurent, S.; Dutz, S.; Häfeli, U. O. and Mahmoudi, M., *Advances in Colloid and Interface Sci.*, 2011, **166**(1–2), 8–23.

[145] Kita, E.; Oda, T.; Kayano, T.; Sato, S.; Minagawa, M.; Yanagihara, H.; Mikio Kishimoto, ; Mitsumata, C.; Hashimoto, S.; Yamada, K. and Ohkohchi, N., *J. Phys. D: Appl. Phys.*, 2010, **43**(47), 474011.

[146] Tasci, T. O.; Vargel, I.; Arat, A.; Guzel, E.; Korkusuz, P. and Atalar, E., *Med. Phys.*, 2009, **36**(5), 1906–1912.

[147] Thomas, L. A.; Dekker, L.; Kallumadil, M.; Southern, P.; Wilson, M.; Nair, S. P.; Pankhurst, Q. A. and Parkin, I. P., *J. Mater. Chem.*, 2009, **19**(36), 6529–6535.

[148] Rabias, I.; Tsitrouli, D.; Karakosta, E.; Kehagias, T.; Diamantopoulos, G.; Fardis, M.; Stamopoulos, D.; Maris, T. G.; Falaras, P.; Zouridakis, N.; Diamantis, N.; Panayotou, G.; Verganelakis, D. A.; Drossopoulou, G. I.; Tsilibari, E. C. and Papavassiliou, G., *Biomicrofluidics*, 2010, **4**(2), 024111.

[149] Gazeau, F.; Lévy, M. and Wilhelm, C., *Nanomedicine*, 2008, **3**(6), 831–844.

[150] Maier-Hauff, K.; Rothe, R.; Scholz, R.; Gneveckow, U.; Wust, P.; Thiesen, B.; Feussner, A.; Deimling, A. v.; Waldoefner, N.; Felix, R. and Jordan, A., *J. Neurooncol.*, 2006, **81**(1), 53–60.

[151] Pankhurst, Q. A.; Thanh, N. T. K.; Jones, S. K. and Dobson, J., *J. Phys. D: Appl. Phys.*, 2009, **42**(22), 224001.

[152] Roca, A. G.; Costo, R.; Rebolledo, A. F.; Veintemillas-Verdaguer, S.; Tartaj, P.; González-Carreño, T.; Morales, M. P. and Serna, C. J., *J. Phys. D: Appl. Phys.*, 2009, **42**(22), 224002.

[153] Baaziz, W.; Pichon, B. P.; Fleutot, S.; Liu, Y.; Lefevre, C.; Greneche, J.-M.; Toumi, M.; Mhiri, T. and Begin-Colin, S., *J. Phys. Chem. C*, 2014, **118**(7), 3795–3810.

[154] Rockenberger, J.; Scher, E. C. and Alivisatos, A. P., *J. Am. Chem. Soc.*, 1999, **121**(49), 11595–11596.

[155] Peng, X.; Schlamp, M. C.; Kadavanich, A. V. and Alivisatos, A. P., *J. Am. Chem. Soc.*, 1997, **119**(30), 7019–7029.

[156] Dabbousi, B. O.; Rodriguez-Viejo, J.; Mikulec, F. V.; Heine, J. R.; Mattoussi, H.; Ober, R.; Jensen, K. F. and Bawendi, M. G., *J. Phys. Chem. B*, 1997, **101**(46), 9463–9475.

[157] Akbarzadeh, A.; Samiei, M. and Davaran, S., *Nanoscale Res. Lett.*, 2012, **7**(1), 144.

[158] Hines, M. A. and Guyot-Sionnest, P., *J. Phys. Chem.*, 1996, **100**(2), 468–471.

[159] Qu, L.; Peng, Z. A. and Peng, X., *Nano Lett.*, 2001, **1**(6), 333–337.

[160] Grünberg, K.; Müller, E.-C.; Otto, A.; Reszka, R.; Linder, D.; Kube, M.; Reinhardt, R. and Schüler, D., *Applied and Environ. Microbiol.*, 2004, **70**(2), 1040–1050.

[161] Schübbe, S.; Kube, M.; Scheffel, A.; Wawer, C.; Heyen, U.; Meyerdierks, A.; Madkour, M. H.; Mayer, F.; Reinhardt, R. and Schüler, D., *J. Bacteriol.*, 2003, **185**(19), 5779–5790.

[162] Matsunaga, T.; Okamura, Y.; Fukuda, Y.; Wahyudi, A. T.; Murase, Y. and Takeyama, H., *DNA Res.*, 2005, **12**(3), 157–166.

[163] Matsunaga, T. and Okamura, Y., *Trends Microbiol.*, 2003, **11**(11), 536–541.

[164] Faivre, D. and Schüler, D., *Chem. Rev.*, 2008, **108**(11), 4875–4898.

[165] Komeili, A., *Annu. Rev. Biochem.*, 2007, **76**(1), 351–366.

[166] Cornell, R. M. and Schwertmann, U., *The Iron Oxides*, Wiley-VCH Verlag GmbH & Co. KGaA, Weinheim, FRG, 2003.

[167] Roth, H.-C.; Schwaminger, S. P.; Schindler, M.; Wagner, F. E. and Berensmeier, S., *J. Magn. Magn. Mater.*, 2015, **377**, 81–89.

[168] Debnath, N. C. and Anderson, A. B., *Surf. Sci.*, 1983, **128**(2), 61–69.

[169] Tombácz, E.; Hajdú, A.; Illés, E.; László, K.; Garberoglio, G. and Jedlovszky, P., *Langmuir*, 2009, **25**(22), 13007–13014.

[170] Wu, W.; Xiao, X.; Zhang, S.; Zhou, J.; Fan, L.; Ren, F. and Jiang, C., *J. Phys. Chem. C*, 2010, **114**(39), 16092–16103.

[171] Brown, G. E.; Henrich, V. E.; Casey, W. H.; Clark, D. L.; Eggleston, C.; Felmy, A.; Goodman, D. W.; Grätzel, M.; Maciel, G.; McCarthy, M. I.; Nealson, K. H.; Sverjensky, D. A.; Toney, M. F. and Zachara, J. M., *Chem. Rev.*, 1999, **99**(1), 77–174.

[172] McCarty, K. F.; Monti, M.; Nie, S.; Siegel, D. A.; Starodub, E.; El Gabaly, F.; McDaniel, A. H.; Shavorskiy, A.; Tyliszczak, T.; Bluhm, H.; Bartelt, N. C. and de la Figuera, J., *J. Phys. Chem. C*, 2014, **118**(34), 19768–19777.

[173] Yu, X.; Li, Y.; Li, Y.-W.; Wang, J. and Jiao, H., *J. Phys. Chem. C*, 2013, **117**(15), 7648–7655.

[174] Zhao, L.; Zhang, H.; Xing, Y.; Song, S.; Yu, S.; Shi, W.; Guo, X.; Yang, J.; Lei, Y. and Cao, F., *Chem. Mater.*, 2008, **20**(1), 198–204.

[175] Sato, J.; Kobayashi, M.; Kato, H.; Miyazaki, T. and Kakihana, M., *J. Asian Ceram. Soc.*, 2014, **2**(3), 258–262.

[176] Shimizu, T. K.; Jung, J.; Kato, H. S.; Kim, Y. and Kawai, M., *Phys. Rev. B*, 2010, **81**(23), 235429.

[177] Tartaj, P.; Morales, M. P.; Gonzalez-Carreño, T.; Veintemillas-Verdaguer, S. and Serna, C. J., *Adv. Mater.*, 2011, **23**(44), 5243–5249.

[178] Adib, K.; Camillone III, N.; Fitts, J. P.; Rim, K. T.; Flynn, G. W.; Joyce, S. A. and Osgood Jr, R. M., *Surf. Sci.*, 2002, **497**(1–3), 127–138.

[179] Rim, K. T.; Müller, T.; Fitts, J. P.; Adib, K.; Camillone, N.; Osgood, R. M.; Batista, E. R.; Friesner, R. A.; Joyce, S. A. and Flynn, G. W., *J. Phys. Chem. B*, 2004, **108**(43), 16753–16760.

[180] Cutting, R. S.; Muryn, C. A.; Thornton, G. and Vaughan, D. J., *Geochim. Cosmochim. Acta*, 2006, **70**(14), 3593–3612.

[181] Noh, J.; Osman, O. I.; Aziz, S. G.; Winget, P. and Brédas, J.-L., *Chem. Mater.*, 2015, **27**(17), 5856–5867.

[182] Metropolis, N.; Rosenbluth, A. W.; Rosenbluth, M. N.; Teller, A. H. and Teller, E., *J. Chem. Phys.*, 1953, **21**(6), 1087–1092.

[183] Berendsen, H. J. C.; van der Spoel, D. and van Drunen, R., *Comput. Phys. Commun.*, 1995, **91**(1), 43–56.

[184] Abraham, M. J.; Murtola, T.; Schulz, R.; Páll, S.; Smith, J. C.; Hess, B. and Lindahl, E., *SoftwareX*, 2015, **1–2**, 19–25.

[185] Strunk, T.; Wolf, M.; Brieg, M.; Klenin, K.; Biewer, A.; Tristram, F.; Ernst, M.; Kleine, P. J.; Heilmann, N.; Kondov, I. and Wenzel, W., *J. Comput. Chem.*, 2012, **33**(32), 2602–2613.

[186] Tribello, G. A.; Bonomi, M.; Branduardi, D.; Camilloni, C. and Bussi, G., *Comput. Phys. Comm.*, 2014, **185**(2), 604–613.

[187] Verlet, L., *Phys. Rev.*, 1967, **159**(1), 98.

[188] Grochowski, P. and Trylska, J., *Biopolymers*, 2008, **89**(2), 93–113.

[189] Still, W. C.; Tempczyk, A.; Hawley, R. C. and Hendrickson, T., *J. Am. Chem. Soc.*, 1990, **112**(16), 6127–6129.

[190] Hornak, V.; Abel, R.; Okur, A.; Strockbine, B.; Roitberg, A. and Simmerling, C., *Proteins: Struct., Funct., Bioinf.*, 2006, **65**(3), 712–725.

[191] Best, R. B. and Hummer, G., *J. Phys. Chem. B*, 2009, **113**(26), 9004–9015.

[192] Lindorff-Larsen, K.; Piana, S.; Palmo, K.; Maragakis, P.; Klepeis, J. L.; Dror, R. O. and Shaw, D. E., *Proteins: Struct., Funct., Bioinf.*, 2010, **78**(8), 1950–1958.

[193] Schrödinger, LLC, 2015.

[194] Darve, E. and Pohorille, A., *J. Chem. Phys.*, 2001, **115**(20), 9169–9183.

[195] Lennard, J. and Jones, I. In *Proc. R. Soc. London*, Vol. 106, pages 441–477, 1924.

[196] Setzler, J.; Seith, C.; Brieg, M. and Wenzel, W., *J. Comput. Chem.*, 2014, **35**(28), 2027–2039.

[197] Born, M., *Z. Physik*, 1920, **1**(1), 45–48.

[198] Palafox-Hernandez, J. P.; Tang, Z.; Hughes, Z. E.; Li, Y.; Swihart, M. T.; Prasad, P. N.; Walsh, T. R. and Knecht, M. R., *Chem. Mater.*, 2014, **26**(17), 4960–4969.

[199] Cooper, G. M. and Hausman, R. E., *The cell: a molecular approach*, ASM Press ; Sinauer Associates, Washington, D.C. : Sunderland, Mass, 3rd ed ed., 2004.

[200] Heinz, H.; Farmer, B. L.; Pandey, R. B.; Slocik, J. M.; Patnaik, S. S.; Pachter, R. and Naik, R. R., *J. Am. Chem. Soc.*, 2009, **131**(28), 9704–9714.

[201] Tang, Z.; Palafox-Hernandez, J. P.; Law, W.-C.; E. Hughes, Z.; Swihart, M. T.; Prasad, P. N.; Knecht, M. R. and Walsh, T. R., *ACS Nano*, 2013, **7**(11), 9632–9646.

[202] Gutz, I. G. R., CurTiPot – pH and Acid–Base Titration Curves: Analysis and Simulation freeware.

[203] TURBOMOLE V7.1 2016, a development of University of Karlsruhe and Forschungszentrum Karlsruhe GmbH, 1989-2007, TURBOMOLE GmbH, since 2007; available from
`http://www.turbomole.com`.

[204] Ahlrichs, R.; Bär, M.; Häser, M.; Horn, H. and Kölmel, C., *Chem. Phys. Lett.*, 1989, **162**(3), 165–169.

[205] Treutler, O. and Ahlrichs, R., *J. Chem. Phys.*, 1995, **102**(1), 346–354.

[206] Perdew, J. P.; Burke, K. and Ernzerhof, M., *Phys. Rev. Lett.*, 1996, **77**(18), 3865–3868.

[207] Adamo, C. and Barone, V., *J. Chem. Phys.*, 1999, **110**(13), 6158–6170.

[208] Stephens, P.; Devlin, F.; Chabalowski, C. and Frisch, M. J., *J. Phys. Chem.*, 1994, **98**(45), 11623–11627.

[209] Vosko, S. H.; Wilk, L. and Nusair, M., *Can. J. Phys.*, 1980, **58**(8), 1200–1211.

[210] Becke, A. D., *J. Chem. Phys.*, 1993, **98**(7), 5648–5652.

[211] Lee, C.; Yang, W. and Parr, R. G., *Phys. Rev. B*, 1988, **37**(2), 785–789.

[212] Weigend, F. and Ahlrichs, R., *Phys. Chem. Chem. Phys.*, 2005, **7**(18), 3297.

[213] Weigend, F., *Phys. Chem. Chem. Phys.*, 2006, **8**(9), 1057.

[214] Teunissen, E. H.; Jansen, A. P. J.; Santen, R. A. v.; Orlando, R. and Dovesi, R., *J. Chem. Phys.*, 1994, **101**(7), 5865–5874.

[215] Herschend, B.; Baudin, M. and Hermansson, K., *J. Chem. Phys.*, 2004, **120**(10), 4939–4948.

[216] Fink, K., *Chem. Phys.*, 2006, **326**(2), 297–307.

[217] Burow, A. M.; Sierka, M.; Döbler, J. and Sauer, J., *J. Chem. Phys.*, 2009, **130**(17), 174710.

[218] Stodt, D. and Hättig, C., *J. Chem. Phys.*, 2012, **137**(11), 114705.

[219] Evjen, H. M., *Phys. Rev.*, 1932, **39**(4), 675–687.

[220] Stolarczyk, L. Z. and Piela, L., *InterNatl. J. (Wash.) of Quantum Chemistry*, 1982, **22**(5), 911–927.

[221] Mulliken, R. S., *J. Chem. Phys.*, 1955, **23**(10), 1833–1840.

Acknowledgments

I would like to thank to:

Prof. Dr. Wolfgang Wenzel for the opportunity of doing PhD in his group, and an endless list of ideas.
His group's members for the scientific and technical support when using SIMONA.

PD Dr. Karin Fink for the broadly understood support, friendly attitude, and understandable explanations of difficult tasks.
Her group's members for the nice atmosphere, interesting discussions, and the lunch company in Campus Nord.

Prof. Dr. Willem Klopper for a spot in one of the offices in Campus South, and knowledge-expanding seminars.
His group's members for a pleasant and cheerful time in mensa and during after-work events, friendly atmosphere, and also for the unforgettable impressions from making PhD hats and cars.

Scientific collaborators from the theory: Dr. Priya Anand, Florian Gußmann, Dr. Martin Brieg, Prof. Dr. Wolfgang Wenzel, PD Dr. Karin Fink; and from the experiment: Silvia Blank-Shim, Sebastian Schwaminger, Dr. Paula Fraga Garcia, Prof. Dr. Sonja Berensmeier. Without them this thesis would not be in the form it is.

My family and friends for faith in my abilities, words of encouragement and not too many questions about "how is my thesis going".

Dr. Paweł Panek, my husband, for literally everything, presence in stressful moments, support in realizing the challenges, corrections, and wonderful life together.
Eva Panek, my daughter, for showing me new aspects of everyday life, and distracting me from thinking about work.